APPENDIX 1 : REFERENCES

1.1 CHAPTER 2

[Artières et al., 2010] O. Artières, M. Galiana, P. Royet, Y.-L. Beck, P. Cunat, J.-R. Courivaud, J.-J. Fry, Y.H. Fuare, C. Guidoux (2010) Fiber optics monitoring solution for canal dykes. PIANC MMX Congres Liverpool UK.

[Bourges & Mieussens, 1979] F. Bourges, C. Mieussens (1979) Déplacements latéraux à proximité des remblais sur sols compressibles, Méthode de prevision, Bulletin liaison Laboratoire Central des Ponts et Chaussées, 101, mai-juin 1979

[Calle et al., 2007] E.O.F. Calle, F.P.H. Engering, G.A.M. Kruse, J.B. Sellmeijer, V.M. van Beek (2007) Module MPiping-VNK voor piping-analyse in PC-Ring. Fase 2 van het project Veiligheid Nederland in Kaart. GeoDelft Report 424111-0014 v05, 9 March 2007

[CUR 228, 2010] Ontwerprichtlijn door grond horizontaal belaste palen (2010) ISBN 987-90-376-0524-2, CUR publication C228

[den Haan and Feddema, 2009] E.J. den Haan, A. Feddema (2009) Deformatie en sterkte van ophogingen en dijken op slappe Nederlandse grond. Geotechniek, oktober 2009, 52-55.

[FC2009, Robust monitoring] Deltares, IBM and TNO (2009) Robust monitoring – Added value of sensor streams in dike monitoring systems. FC2015 report 2009.02.01.1

[Koelewijn et al., 2010] A.R. Koelewijn, N. Pals, M.J. Sas, W.S. Zomer (eds.) (2010) IJkdijk Pipingexperiment - Validatie van sensor- en meettechnologie voor detectie van optreden van piping in waterkeringen. ISBN: 978.90.5773.485.4. Report 2010-26 PIW

[Sakurai et al., 2003] S. Sakurai, K. Adachi, T. Takeishi, T. Iwasaki (2003) An evaluation technique for slope stability based in displacements measures at the slope surface. In: Field measurements in Geomechanics, Myrvoll (ed.). ISBN 90 5809 602 5

[Sellmeijer, 1988] J.B. Sellmeijer (1988) On the mechanism of piping under impervious structures, PhD Thesis, Technische Universiteit Delft.

[Sellmeijer et al.,2011] J.B. Sellmeijer, J. Lopéz de la Cruz, V.M. van Beek, J.G. Knoeff (2011) Fine-tuning of the piping model through small-scale, medium-scale and IJkdijk experiments. Submitted to European Journal of Environmental and Civil Engineering.

[van Beek en Knoeff, 2010] V.M. van Beek, J.G. Knoeff (2010) SBW Piping: Hervalidatie piping: HP5.5a Analyse en validatie full-scale proeven. Deltares report 1200690-005-GEO-0006 version 3, 7 May 2010.

[van Duinen, 2010] A. van Duinen (2010) SBW Werkelijke sterkte van dijken - validatie WS15, Deltares report: 1202121-003-GEO-0022-v1-r (Draft version, 7 September 2010).

[Vermeer et al., 2010] P.A. Vermeer, I. Jassim, F. Hamad (2010) Need and Performance of New Undrained Clay Model. Deltares report 1201662-003-GEO-0003.

[Weijers et al. 2009] J.E. Weijers, G.T Elbers, A.R. Koelewijn, N. Pals (eds.) (2009) Macrostabiliteit IJkdijk: Sensor- en meettechnologie. ISBN: 978.90.5773.432.8, VIW report 2009-19.

1.2 CHAPTER 4

[de Kleine et al. 2010] M. de Kleine, J. Buma, V. Marges, A. Menkovic, L. Vonhögen, A. Wiersma (2010) Ondergrond schematisatie Julianakanaal. Deltares report 1202392-000-BGS-0001, June 2010.

[Heimivaara and Bouten, 1990] T.J. Heimovaara and W. Bouten (1990). A computer-controlled 36-channel time domain reflectometry system for monitoring soil water contents. Water Resour. Res., Vol 26, p. 2311-2316.

[Huisman et al., 2003] J.A. Huisman, S.S. Hubbard, J.D. Redman, A.P. Annan (2003). Measuring Soil Water Content with Ground Penetrating Radar: A Review. Vadose Zone, Vol 2, p 476-491.

[Smulders et al. 2010] D. Smulders, M. Bierkens, R. Westerhoff (2010) Internship at Deltares: A quantitative analysis of the applicability of the ASAR imagery for soil moisture content mapping at a regional scale in the Netherlands. Deltares report 1201880-000-BGS-0001.

[Swart et al., 2008] L.M.T. Swart, S.J. Flos, W.S. Zomer (2008) Laseraltimetrie voor waterkeringbeheer: ontwikkelingen, gewenste specificaties, procesbeschrijving en evaluatie AHN-2-proef. STOWA report VIW 2008-06, RWS report RWS WD 2008-012.

[TU Delft 2009] K. Arroyo, P. Bhattacharya, F. Biljecki, D. Kalpoe, Á. Muñoz, P.T. van der Toren, S. Verlaar, H. Yu (2009) Satellite radar observation feasibility study for large infrastructural public works – A case study on the Delft train tunnel. Geomatics Synthesis Project 4 - Argus Panoptes. Delft University of Technology.

[van Meerten et al. 2009] H. van Meerten, F. Hesami, A. Venmans (2009) GeoRisicoScan Julianakanaal - Verruiming Julianakanaal. Deltares report 1201613-000-GEO-0005 (Draft version, December 2009)

References for leakage:

Baghdadi, N., King, C., Bourguignon, A. and Remond, A. (2002) Potential of ERS and Radarsat data for surface roughness monitoring over bare agricultural fields: application to catchments in Northern France, *International Journal of Remote Sensing*, **23(17),** pp3427-3442

Baghdadi, N., Holah, N. and Zribi. M. (2006) Soil moisture estimation using multi-incidence and multi-polarisation ASAR data, *International Journal of Remote Sensing,* **27 (10),** pp1907-1920.

Baghdadi, N., Aubert, M., Cerdan, O. and Franchisteguy, L. (2007) Operational mapping of soil moisture using Synthetic Aperture Radar data: application to the Touch Basin (France), *Sensors*, **7**, pp2458-2483

Baghdadi, N., Zribi, M., Loumagne, C., Ansart, P. and Anguela T. P. (2008) Analysis of TerrSAR-X data and their sensitivity to soil surface parameters over bare agricultural fields, *Remote Sensing of Environment,* **112**, pp4370-4379.

Dubois, P. C., van Zyl, J. And Engman, T. (1995) Measuring soil moisture with imaging radars, *IEEE Transactions on Geoscience and Remote Sensing*, **33 (4)**, pp915-926

Gabriel, A. K., Goldstein, R. M. and Zebker, H. A. (1989) Mapping small elevation changes over large areas: Differential Radar Interferometry, *Journal of Geophysical Research*, **94 (B4)**, pp9183-9191.

Hajnsek, I., Pottier, E. And Cloude, S. R. (2003) Inversion of surface parameters from polarimetric SAR, *IEEE Transactions on Geoscience and Remote Sensing*, **41 (4)**, pp727-747

Keydel, W. (2005) Polarimetry and Interferometry Applications, *NATO Research and Technology Organisation document in support of lecture series presented on 14-15th October 2004, Belgium, 18-19th October 2004, Washington DC, USA and 21-22nd October Ottawa, Canada.*

Lee, J. S., Yueh, S. H. And Schuler, D. L. (2004) Polarimetric analsyis of scatterometer data for ocean surface wind measurement, *Proceedings of the International Geoscience and RemoteSensing Symposium, IGARSS'04, Anchorage, Alaska.*

Oh, Y., Sarabandi, K. And Ulaby, F. T. (1992) An empirical model and an inversion technique for radar scattering from bare soil surfaces, *IEEE Transactions on Geoscience and Remote Sensing*, **30 (2)**, pp370-381

Martin Jr, R. D., Asrar, G. And Kanemasu, E. T. (1989) C-Band scatterometer measurements of a tall grass prairie, *Remote Sensing of Environment*, **29**, pp281-292

Martone, M., Jagdhuber, T., Hajnsek, I. And Iodice, A. (2009) Modified scattering decomposition for soil moisture estimation from polarimetric X-Band data, *Master Thesis, DLR-HR/University of Naples, Federco II, 2009*

Nolan, M. and Fatland D. R. (2003) Penetration Depth as a DInSAR Observable and Proxy for Soil Moisture, *IEEE Transactions on Geoscience and Remote Sensing,* **41 (3)**, pp532-537.

Nolan, N., Fatland, D. R. and Hinzman, L. (2003) DInSAR Measurement of Soil Moisture, *IEEE Transactions on Geoscience and Remote Sensing,* **41 (12)**, pp2802-2813.

Skriver, H. (2008) Comparison between Multi-temporal and Polarimetric SAR data for land cover classification, *Proceedings of IEEE International Geoscience and Remote Sensing Symposium 2008 (IGARSS), 7-11 July*, **III,** pp558-561.

Ticconi, F., Martone, M., Jagdhuber, T. and Hajnsek, I. (2010) Investigation of fully polarimetric TerraSAR-X data for soil parameters estimation, *Proceedings of the 8th European conference on Synthetic Aperture Radar (EUSAR) 7-10th June 2010, Aachen, Germany.*

Ulaby, F. T., Dubois, P. C. and Van Zyl, J. (1996) Radar Mapping of Surface Soil Moisture, *Journal of Hydrology*, **184**, pp57-84.

Wang, C., Qi, J., Moran, S. and Marsett, R. (2004) Soil moisture estimation in a semiarid rangeland using ERS-2 and TM imagery, *Remote Sensing of Environment,* **90**, pp178-189.

1.3 CHAPTER 5

[FC 2010] IBM, Deltares, TNO, Fugro, Stichting IJkdijk (2010) Feasibility study of smart levees concepts. Flood Control 2015 report 2010.02.01.1

[International Levee Handbook] International Levee Handbook Scoping document, http://www.ciria.org/service/Home/AM/ContentManagerNet/ContentDisplay.aspx?Section=Home&ContentID=17434

[Koelewijn et al., 2010] A.R. Koelewijn, N. Pals, M.J. Sas, W.S. Zomer (eds.) (2010) IJkdijk Pipingexperiment - Validatie van sensor- en meettechnologie voor detectie van optreden van piping in waterkeringen. ISBN: 978.90.5773.485.4. Report 2010-26 PIW

[Marnette, 2010] K. Marnette (2010) The future of smart levees - Levee monitoring and the potential of self-potential. Deltares report of internship.

APPENDIX 2 : PARAMETERS FOR SLOPE STABILITY

Table 1 Suitability of various parameters to monitor the slope stability of a levee

Parameters sensitive to slope stability	Basic idea for link between parameter and failure mechanism	Judgement (by dike expert) of suitability of parameter for monitoring slope stability process	What model?	Technique	Basic idea confirmed by data according to sensor party.
Pore pressure	The phreatic line inside the levee is one of the parameters describing the slope stability of the levee. The phreatic line can be derived from pore pressure measurements.	Suitable, because the pore pressures are direct input for an analysis. They can be used to calculate the current slope stability factor. For extrapolation, time series can be used in order to determine the slope stability at the representative water level.	Bishop, Spencer, Van or Fellenius. Implemented in MStab and in FEWS-DAM.	Point measurements in levee by piezoresistive pore pressure sensors	Yes
	Pore pressures in aquifers and aquitards affect the slope stability of the levee.		Qualitative correlation of pore pressures and activities.	Point measurements in levee by MEMS sensors	Yes
			Qualitative correlation of pore pressures and activities.	Point measurements in levee by piezoresistive pore pressure sensors	Yes. Trend in pore pressures coincides with trend in displacements.
Tilt	Movement along slip plane inside levee for early detection of slope instability.	Possibly to be used as deformations.	Desk study (not real-time): finite element methods (e.g. Plaxis).	Fixed line measurement in levee	Yes
			1. Change point analysis. 2. Qualitative correlation of angles and load on levee.	Point measurements in levee by MEMS sensors	Yes, but sensors had no rigid connection.
			Qualitative correlation of angles and load on levee.	Point measurements in levee by MEMS sensors	Yes

Parameters sensitive to slope stability	Basic idea for link between parameter and failure mechanism	Judgement (by dike expert) of suitability of parameter for monitoring slope stability process	What model?	Technique	Basic idea confirmed by data according to sensor party.
Temperature	None	Not suitable, because it is a very indirect parameter to put into models.	None	Point measurements in levee by MEMS sensors	No conclusion for temperature provided.
	Change in hydraulic conductivity at overloading of the levee, causing changes in temperature by movement of relatively cold water.		Pattern recognition for temperature and curves of thermic intensity of levee segments.	Remote thermographic camera	Yes, difference in curves of thermic intensity between day before and day of failure.
	Changes in groundwater flow (and corresponding temperature distribution) in levee caused by leakage.		Qualitative correlation of temperatures and load on levee attempted.	Heat pulse fibre optics	Yes. No significant leakage detected unless temperature differences are larger than 1K.
Deformation	Movement of levee at (start of) slope instability.	Suitable, because deformation is linked to strength, which is one of the input parameters in the safety factor model. Deformations can be compared to calculations as a measure for reliability. However, deformation is not the driving mechanism, it may lag behind. Alternatively, fragility curves based on measurements can give an update about the slope stability.	Pattern recognition for deformation.	Remote thermographic camera	Although deformation was detected, the accuracy was not (yet) sufficient.
			Pattern recognition for deformation.	Terrestrial laser scanning	Yes, qualitative correlation between timing of deformations and activities during experiment.
Strain		Possibly to be used as deformations.	Qualitative correlation of strain distribution and activities during experiment.	Fibre optics in GeoDetect mat	Yes, qualitative correlation between timing of strain and load on levee. Also location of breach detected.

Parameters sensitive to slope stability	Basic idea for link between parameter and failure mechanism	Judgement (by dike expert) of suitability of parameter for monitoring slope stability process	What model?	Technique	Basic idea confirmed by data according to sensor party.
Damping	Mechanical damage to fibre optic cable due to bending and straining during movement related to slope instability causes changes in damping of the light signal.	Indirect measurement of deformation. Suitability depends on the results.	Analysis of damping at various timestamps during the experiment.	Heat pulse optical fibre	Not confirmed at IJkdijk slope stability test because of lack of measurements related to time of failure and operational mistakes.
Movement and vibration	Overloading of the levee causes movement and vibrations inside the levee.	Indirect measurement of deformation. Suitability depends on the results.	Amplitude of vibration at 1.81 Hz and combined deformation parameter as indicators for pending slope instability.	Fibre optics	Yes, but meaning of all measured parameters not fully understood yet.
Vibration	Overloading of the levee causes vibrations inside the levee.	Indirect measurement of deformation. Suitability depends on the results	Qualitative analysis of acoustic signals and spectrograms in relation to activities during the experiment.	Hydrophones and microphones in drainage tube	Yes, filling of levee with water can be detected.
Various	Related to movement of levee and pore pressure distribution inside levee.		Qualitative analysis of various signals in relation to activities during the experiments.	IS-system	Various sensors sensitive to activities of crane. Good results for: Inplace inclinometer, water pressure meters (BAT), Liquid Levelling sensors. No good results for: Inverted Pendulum and Settlement strand
Various	None, goal was testing the application of various types of sensors in levee.	Irrelevant	None	E+Soil MCT sensor, ECH2O-TE, EnviroSMART	No basic idea to be confirmed.

APPENDIX 3 : PARAMETERS FOR BACKWARD PIPING EROSION

Table 1 Suitability of various parameters to monitor the process of backward piping erosion in a levee

Parameters sensitive to backward piping erosion	Basic idea for link between parameter and failure mechanism	Judgement (by dike expert) of suitability of parameter for monitoring of the failure process affected by pipes	What model?	Technique	Basic idea confirmed by data according to sensor party
Pore pressure	Slight drop in pore pressure at formation of new pipe. Sharp rise in pore pressure after pipe has reached upstream side of levee. Pore pressures in aquifer are sensitive to presence of pipes in the vicinity of sensors.	Very suitable, proven in the past	Sellmeijer, implemented in FEWS-DAM	Point measurements in levee by piezoresistive pore pressure sensors	Yes, but correction needed for pore pressures at upstream side because of varying entry resistance caused by silt/mud. Calculated pipe length is very sensitive to position of sensors.
			Difference in pore pressure between parallel rows of sensors as indication for pipe growth.	Point measurements in levee by MEMS sensors	Yes, peaks in difference in pore pressure correspond to moments of 1) first sand producing well, 2) increase in sand transport and formation of new pipes and 3) widening of pipes and breakthrough.
			Qualitative correlation between pore pressures and intervention actions of Luisterbuis.	Fibre optics in drainage tube inside sand layer, under levee	Yes
Discharge	Discharge is related to the amount of water that is flowing through the pipes.	Maybe suitable. Update permeability and calculate length of the pipe. Pipelength might be relatively insensitive to this parameter (needs to be checked).	To be constructed during this project: based on 2D model of Hans Sellmeijer	Point measurements by flow meters	Not analysed yet at start of the project

Parameters sensitive to backward piping erosion	Basic idea for link between parameter and failure mechanism	Judgement (by dike expert) of suitability of parameter for monitoring of the failure process affected by pipes	What model?	Technique	Basic idea confirmed by data according to sensor party
Sand volume	Sand is transported from the pipes and is the volume related to the size of these pipes.	Suitable, by backcalculation of pipelength from sand volume measurements.	To be constructed during this project: based on 2D model of Hans Sellmeijer	Extraction of sand at well and measurement of produced sand volume	Not analyzed yet at the start of this project
Temperature	Water flow through pipes causes localized changes in temperature. Indirect indication of pipes, because water flow does not have to be related to pipe or erosion.	Suitable. Delayed response in case of backward erosion process.	Changes in temperature indicative of water flow.	Point measurements in levee by MEMS sensors	Yes, qualitative correlation between changes in temperature and behavior of pipes during the experiments.
			Image processing techniques to locate areas of outflow of water.	Remote thermographic camera	Yes
			Rate of cooling after heat pulse is quantitative measure for water flow.	Heat pulse fibre optics	Seepage is detected but not quantified.
			Anomalies in spatial temperature distribution as indication for location of pipe. Development of model by Électricité de France using temperature inside levee, air temperature and water temperature to pinpoint locations with anomalous temperatures, to be inspected at the actual levee.	GeoDetect® system and fibre optics	Yes

Parameters sensitive to backward piping erosion	Basic idea for link between parameter and failure mechanism	Judgement (by dike expert) of suitability of parameter for monitoring of the failure process affected by pipes	What model?	Technique	Basic idea confirmed by data according to sensor party
Strain	Flow of water causes movements in levee to be measured as strain.	Suitable, although in existing embankments placement of the mat may be difficult, yet in itself it is a measure against sand erosion, provided the mat pores are small enough to block the sand particles.	Anomalies in spatial strain distribution as indication for location of pipe.	GeoDetect® system and fibre optics	Yes, but only when fibre optic cables are embedded in GeoDetect® mats and not as single, loosely applied cables.
Movement and vibration	Flow of water causes vibrations and movements in levee.	Indirect measurements. Movements and flows are very small. Not suitable, because of synthetic blocks placement in an existing embankment is difficult.	Amplitude of vibration at 1.81 Hz and 4.8 Hz and combined deformation parameter as indications for pipe formation. Model still under development.	Fibre optics with synthetic blocks	Yes, but advanced data analysis to detect location of movement (in stead of an average value only) is still pending.
Vibration	Flow of water causes vibrations in levee.	Indirect measurement. If the discharge proves to work, vibrations might give a local improvement of the prediction.	Increase in amplitude in specified frequency bands with increasing levels of piping.	Hydrophone in drainage tube	No, as no increase in amplitude has been detected. However, the drainage tube is very effective as a counter-measure for piping.
SP	Changes in electrical potentials due to flow of water along grains in porous media. Combination of Law of Darcy (hydraulic conduction), Ohm (electrical conduction) and Fick (chemical diffusion).	Probably suitable, if noise levels are sufficiently small. Filtering needed to interpret signal and correct for instrument drift. Indirect measurement of the discharge, SP might give a local improvement of the prediction.	Data processing (frequency filtering) and detection of anomalies outside noise band.	Point measurements on levee by non-polarizing electrodes Point measurements on levee by non-polarizing electrodes	On first interpretation, late detection of piping by SP due to small contrasts. In the project, more advanced processing is performed.

APPENDIX 4 : STATISTICAL ANALYSIS REPORT

Sensor Behavior and Dike Collapse

4.1 INTRODUCTION AND PROBLEM STATEMENT

Several experiments have been conducted in which levees collapsed with the aim to collect measurements describing what goes on during the experiment. The measurements included several ways to follow the buildup of pressure within the levee, changes in temperature, flow and more.

Every sensor produced one measurement per time interval, sensor readings were combined into lines of measurements per time interval. Time intervals between different measurements were not synchronized. Originally, the aim was to relate every measurement with every other one, but this proved to be very time consuming, due mainly to mismatches in measurement frequencies.

Several parties have contributed measurements to the experiments. They are listed in the tables below.

Table 1 Measurements in Slope Stability Experiment

Party	Sensor	Parameter
Deltares	Pr pore pressure sensors	Pore pressure
	Divers	Pore pressure
	Moisture sensors	Moisture content
	Camera	Deformation
	Tilt meters	Tilt
Alert Solutions	MEMS	Temperature, pore pressure, movement, moisture content
Intech	Thermographic camera	Temperature
Dike Survey	Fiber optic	Movement
Flood Control 2015	E+Soil MCT sensor, ECH2)-TE, EnviroSMART	Moisture content, EC, temperature
GTC Kappelmeyer	Fiber optic (heat pulse)	Temperature
Hansje Brinker	Terrestrial laserscanning	Deformation
Koenders	Inclinometers and pr water pressure sensors	Deformation and water pressure
	Weather station	Air temperature and moisture, wind speed and direction, solar radiation, precipitation
Luisterbuis	Microphones and hydrophones	Acoustic signal
RPS-BCC/IFCO	IS-System	Deformation, water pressure
Inventec/Ten Cate	Fiber optic sensors	Strain and temperature

Table 2 Measurements in Piping Experiments

Party	Sensor	Parameter
Deltares	Pr pore pressure sensors	Pore pressure
	Divers	Pore pressure
	Flow meter	Water flow rate and amount
Fugro	Self potential	SP value
ITC	Self potential	SP value
2M	Capacitive sensors	Electrical capacity
Intech	Infrared camera	Temperature
Dike Survey	Fiber optic	Movement
Luisterbuis	Fiber optic	Water pressure, temperature
	Microphones	Acoustic signal
Alert Solutions	MEMS	Temperature and water pressure
GTC Kappelmeyer	Fiber optic (heat pulse)	Temperature
Ten Cate	Fiber optic	Strain and temperature

SPSS was asked in particular if pressure measurements, as reported by several different instruments, were equivalent and if observed differences in temperature could be related to changes in pressure.
Analysis was done using IBM SPSS Modeler and IBM SPSS Statistics. The main techniques employed were correlation analysis and Principal Components Analysis (PCA). These techniques proved to be well suited for the questions posed and data to be analyzed.

Other techniques would have been applicable as well. Time series analysis could have been conducted to give more insight into the flow of water through the levee, still other techniques would have proposed moments predicting collapse. For detailed reconstructions of what precisely happened inside the levees, more physically oriented models of levee behavior would probably have been necessary. IBM SPSS Modeler and IBM SPSS Statistics offer the techniques to analyze the data successfully in the presence of these reconstructions.

Principal Components Analysis (PCA) was chosen in this case because there were not only different types of pressure measurements, but there were many measurements per type. PCA is a robust technique for data reduction. If these measurements are linearly related PCA reduces these data into a few components, thus providing overview and better insight.

In Piping Experiment 1 PCA the pressure measurements of different types are shown to be equivalent. In Piping Experiment 4, where a drainage tube was employed, the same technique shows two components. The first component shows the effectiveness of drainage. The second component, however, shows that drainage becomes less effective when applied more often under relatively high head.

4.2 PIPING EXPERIMENT 1

This experiment started September 29th 2009, 15:00h and concluded with a collapse on October 3rd 2009, 16:20h. Pressure and temperature sensors were investigated, especially to test if the micro electro mechanical systems (MEMS) pressure measurements (by Alert Solutions) are equivalent to the reference piezoresistive (pr) pore pressure measurements (by Deltares).

To obtain insight into the usability of measures other than the currently used pr-measurements as input for models and/or model changes, SPSS was asked to investigate if the pr pressure measurements and the MEMS pressure measurements are equivalent.

Other measurements were collected for this experiment but so far were not taken into account. This was either because these measurements did not seem relevant to the question at hand or because the intervals of data collection were not compatible.

Changes in temperature may indicate flow of water caused by piping. Temperature changes were analyzed, but no direct and clear association could be detected without physical models of levee behavior.

4.2.1 Sensor locations

The sensors for Experiment 1 were placed as in the graph below.

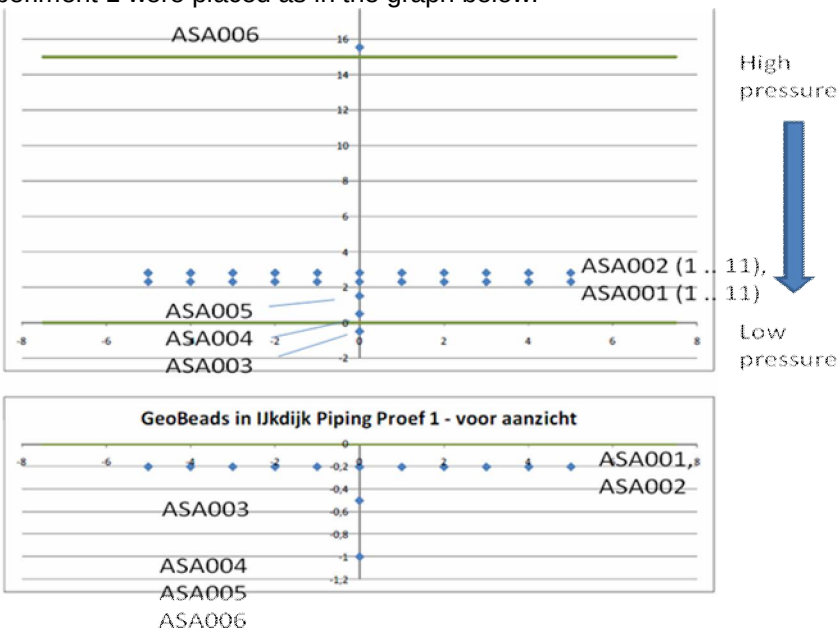

All MEMS sensors report pore pressure and temperature. Sensor ASA006 is in the middle, at the high pressure side, beyond the toe of the dike, 1m below the plane separating sand from clay (dike body). At the low pressure side two sensor chains, 50 cm apart, 20 cm below the plane separating sand from clay, reported pressure and temperature. These chains contained 11 sensors each. In the centre of the levee three more sensors were placed. All three were placed in the middle of the ASA001 chain. Sensor ASA005 was placed 1m below the plane separating sand form clay. At the same depth, 2m behind ASA005 (direction low pressure), ASA004 was placed. Finally, another sensor, ASA003, was located 1m behind ASA004, 50cm below the plane separating sand and clay.

From the pressure time sequence it can be seen that ASA006 reports the highest pressures, followed by ASA005 and ASA004, all 1m below the sand-clay plane. Although ASA003 initially reports pressures similar to ASA004, ASA003 shows less variation than ASA004. Below the pressure measurements of the single sensors the measurements of the two sensor chains ASA001 and ASA002 are located.

The experiment was started 2009-09-29 at 12:30h (1, for reference points see pressure graph below) by raising the water level at the high pressure side of the levee. The next day at 12:00h (2) the first pipes were seen. At 18:00h (3) the critical point of high head was reached. After that moment, all sensors (except ASA006) report diminishing pressures. A long time follows without much pressure change. A flow sensor placed by Landustrie reports a flowburst (4) on 2009-10-02 at 13:30h.

Before pressure increases again, piping channels widen (5). A few hours later, (6), prolonged widening is observed. The first signs of breakdown are visible (7) from the data 2009-10-03 at 14:25h and the levee clearly collapses (8) 2009-10-03 at 16:20h.

4.2.2 Pore Pressure

The MEMS pore pressures as measured by the sensors during the experiment all look surprisingly similar. The following graph shows the sequence of pressure measurements during the experiment.

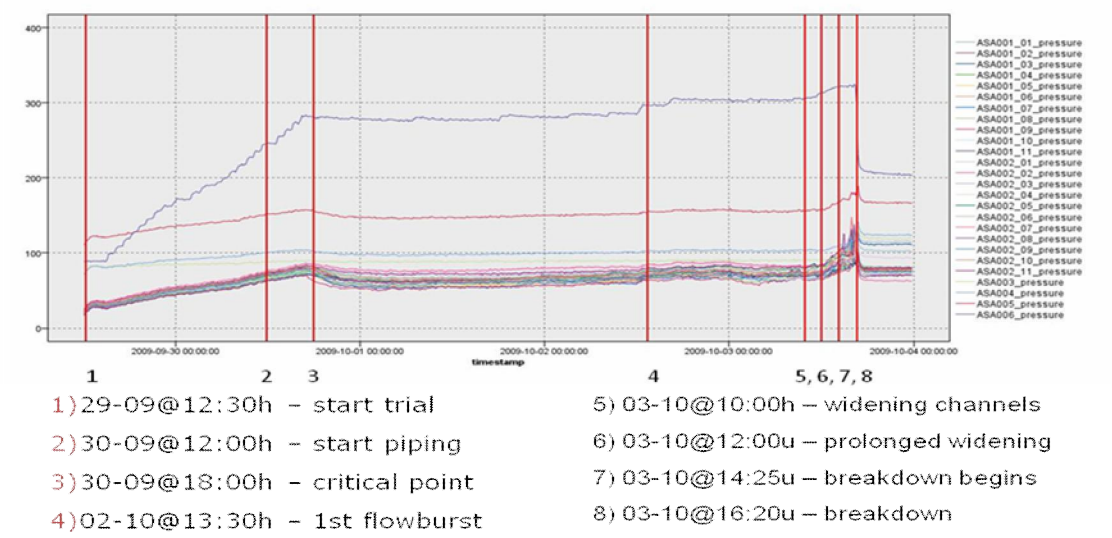

Although similar, the individual pressure sequences between different sensors differ. Highest pressure is recorded by ASA006, located at the upstream side of the dam. The two sensor chains were located at the downstream side of the levee, showing lowest pressures. A critical point is reached (3), after which all sensors report declining pressures, except ASA006. Pressures show little variation until the channels start to widen (5), after which the pressures in the sensor-chain at the downstream side of the dam increases until collapse begins.

4.2.3 Principal Component Analysis

The sequences reported by the sensors all look similar and it is worthwhile to investigate if all sensors describe the same phenomenon or if some sensors describe a different process.

Below is a graph of sensors ASA001_6, ASA002_6 and ASA005, all located closely together where the collapse was expected to take place (middle). The graph below shows a higher overall pressure for ASA005 (80cm below ASA001) and a somewhat higher overall pressure for ASA002 (deeper in the dike) than ASA001 and a very similar pattern in pressure change for all sensors.

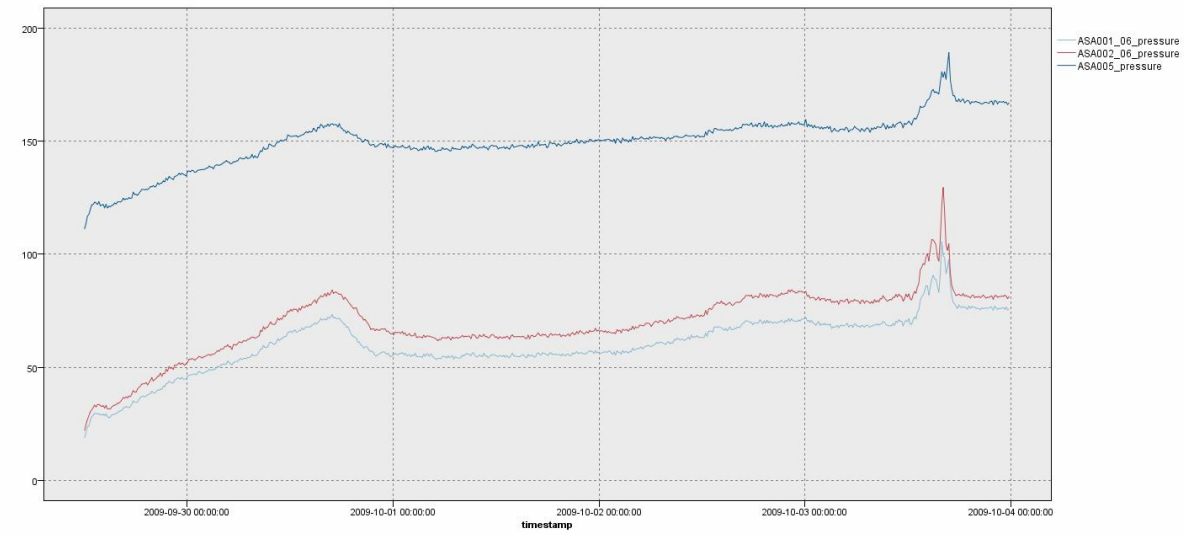

In statistical terms: the measurements are very highly correlated. The correlation coefficient is a useful similarity measure between two sets of observations. It varies between -1 and +1, where +1 indicates perfect similarity, 0 indicates no similarity and -1 indicates perfect reverse similarity. The correlation between a

variable with itself is trivially perfect. The correlation between variables A and B is equal to the correlation between B and A. The correlation matrix between the three sensor measurements is therefore symmetric. Its values are:

Correlation Matrix

		ASA001_06_pressure	ASA002_06_pressure	ASA005_pressure
Correlation	ASA001_06_pressure	1,000	0,998	0,979
	ASA002_06_pressure	0,998	1,000	0,982
	ASA005_pressure	0,979	0,982	1,000

Correlations are very high, indicating the sensors measure the same phenomenon. This can be further established by analyzing the principal components of the correlation matrix. Principal Component Analysis (PCA) is a technique for dimension reduction.

If the three measurements were unrelated, i.e., correlations were near zero, each variable would behave almost independently of every other variable, resulting in 3 dimensions. Higher correlations express more similarity between the measurements and will reduce the number of dimensions. In case of the three highly correlated variables ASA001_6, ASA002_6 and ASA005 one dimension suffices to describe 99% of the variance.

Total Variance Explained

Component	Initial Eigenvalues			Extraction Sums of Squared Loadings		
	Total	% of Variance	Cumulative %	Total	% of Variance	Cumulative %
1	2,973	99,090	99,090	2,973	99,090	99,090
2	0,025	0,849	99,939			
3	0,002	0,061	100,000			

Extraction Method: Principal Component Analysis.

Correlations of the three variables with the first component are displayed in the table below. Geometrically, correlations can be interpreted as cosines. From this analysis the conclusion is justified that the three sensors behave in (almost) exactly the same way.

Component Matrix[a]

	Component
	1
ASA001_06_pressure	0,997
ASA002_06_pressure	0,998
ASA005_pressure	0,991

This technique can also be applied to more than three variables. In particular, SPSS was asked whether the pressure measurements of MEMS were an acceptable replacement for the reference pr sensor measurements. PCA can answer that question in the same vein as we just saw, except that we now have 54 instead of 3 variables.

4.2.4 Equivalence of pressure measurements

During the experiment pore pressure was measured by pr sensors for reference (by Deltares) and by MEMS sensors. The pr sensors were laid out in 4 sensor chains (series WSMA100, WSMA300, WSMA500 and WSMA700), each with 16 pressure sensors. The MEMS sensors were laid out in 2 chains of 11 sensors each. The chains were 50 cm apart. Pr sensor series 300 and 500 were closest to the two MEMS chains. Combining the measurements of series WSMA300, WSMA500, ASA001 and ASA002, amounts to 2x16+2x11=54 variables.

The pr sensors had one measurement every four seconds and the MEMS sensor system had one measurement per ten minutes. To synchronize the measurements, the pr sensor observations in the time span between two MEMS measurements were averaged. The pr sensor pressures were in kPa, the MEMS pressures were measured in mBar. For the analysis the measurements were not converted, instead, the measurements were standardized to mean=0 and variance=1, and PCA was applied to the correlation matrix.

After the dike has collapsed on October 3rd, 16:20h, some sensors start to behave in an uncoordinated fashion, different from their behavior before the crash. As we are more interested in events leading to the crash than events after the collapse, we have analyzed the data from the start of the experiment to the first moment of irregular behavior related to the crash, i.e., October 3rd, 14:25h, point (7) in the pressure graph.

The first dimension describes 97.08% of the variance, enough to claim that the measurements by pr sensors, series WSMA300 and WSMA500 and those by MEMS ASA001 and ASA002 are interchangeable. The 54 variables graphed over the duration of the experiment, all standardized to mean=0 and standard deviation=1.

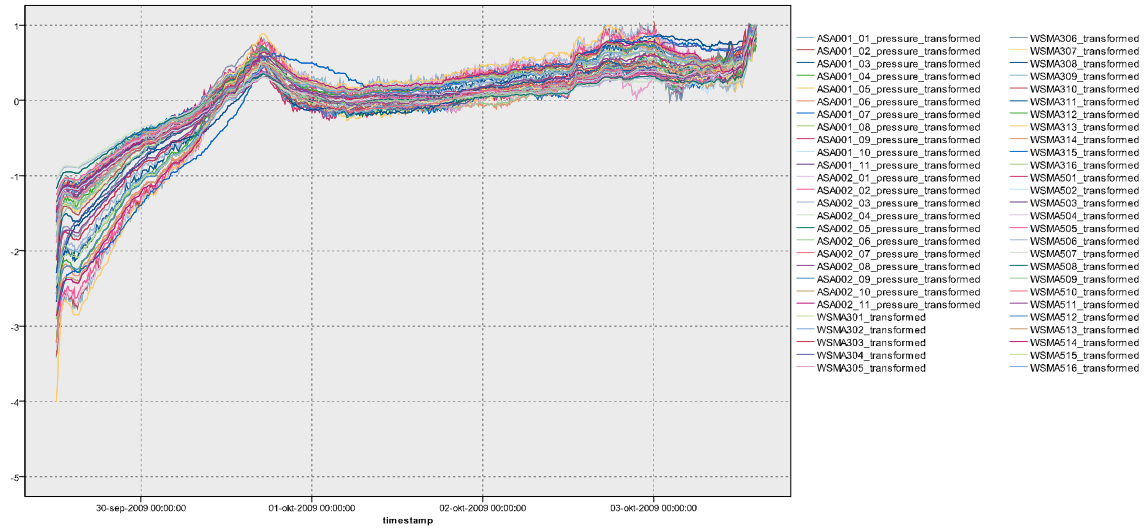

Although WSMA315 reports higher pressures after the first pressure maximum(October 30th) and WSMA315, WSMA308 and WSMA304 report higher ones after the second pressure maximum, these deviations are small and may be ignored from a statistical point of view. Whatever the smallness of these deviations, their behavior is somewhat deviant and there may be good physical reasons for these deviations. From this analysis the conclusion is justified that both types of pressure sensors (pr and MEMS) in Piping Experiment 1 report on just one process (development of pressure), no other processes can be detected in this case.

4.2.5 Pore pressure and individual sensors – comparison by box plots

Comparing the individual pressures in sensors gives insight in the distributions per sensor. We illustrate this by means of box plots. Box plots give a robust and intuitive overview of how the data are distributed.
A box plot is a graphical display showing the first quartile (25% of the observations lie below this point), median (50% above and below), third quartile (75% lie below). The space between first and third quartiles is drawn as a rectangle with a horizontal line symbolizing the median. Two horizontal lines are drawn 1.5 times the height of the box above and below it. Observations above or below these values are called outliers and are marked in the plot with an “o”. Observations more than 3 times the height of the box are called extreme values and they are marked by a ”*” in the plot.

An example shows the box plot for the pressure measurements of ASA005.

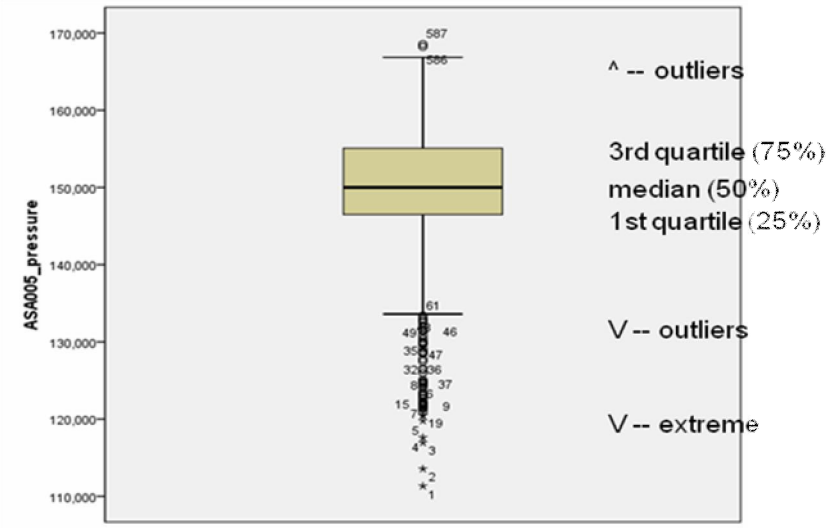

The middle value is around 150, the bulk of the observations lie between the horizontal lines at ±135 and ±166. There are outliers with low pressure and a few with high pressure. Outliers are labeled with the sequence number of the observation. All outliers with low pressure occur in the beginning of the experiment, all outliers with high values occur at the end (observation 587 corresponds to the last observation at October 3rd, 14:25h, when measurements started to deteriorate).

Comparing the two sensor chains for the entire experiment (all data included) with one box plot for each sensor reveals the distribution of water pressure over the individual sensors. There are two chains, labeled ASA001 and ASA002, each equipped with 11 sensors. Both chains were on the land side, ASA002 50cm further into the levee than ASA001.

The box plots for ASA002 (inside levee):

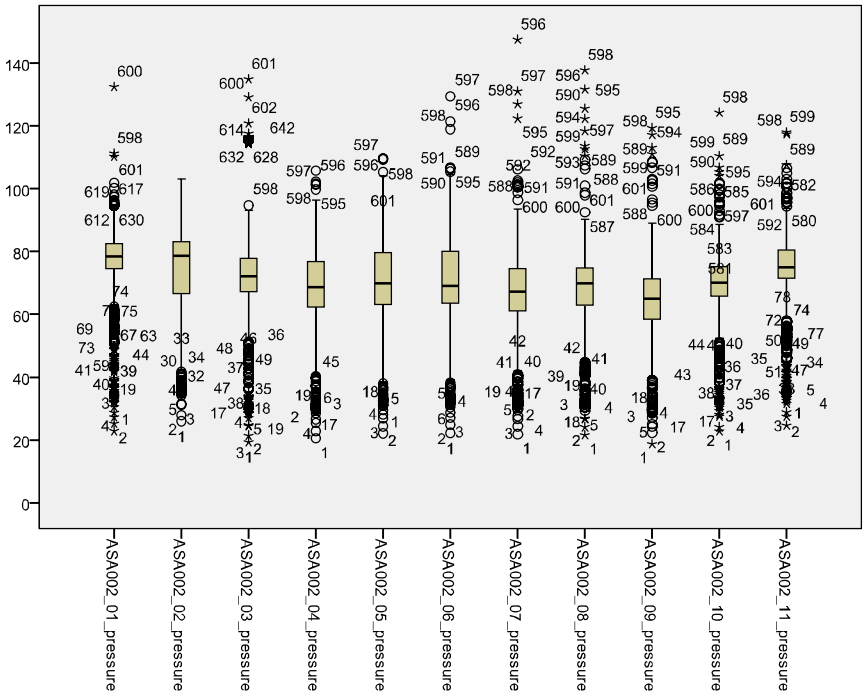

High outliers all begin to show around observation 600, October 3rd, 16:25h, at the onset of the widening of the pipes which will lead to the collapse. ASA002_7 reaches the highest value of all ASA002 sensors: 147.5 at 3-Oct-2009 15:55h. Inspection of the data shows the higher pressures start at sensors 7 and 8 at 15:45h followed by the other sensors 10 to 20 minutes later.

Box plots for ASA001 (downstream side of levee):

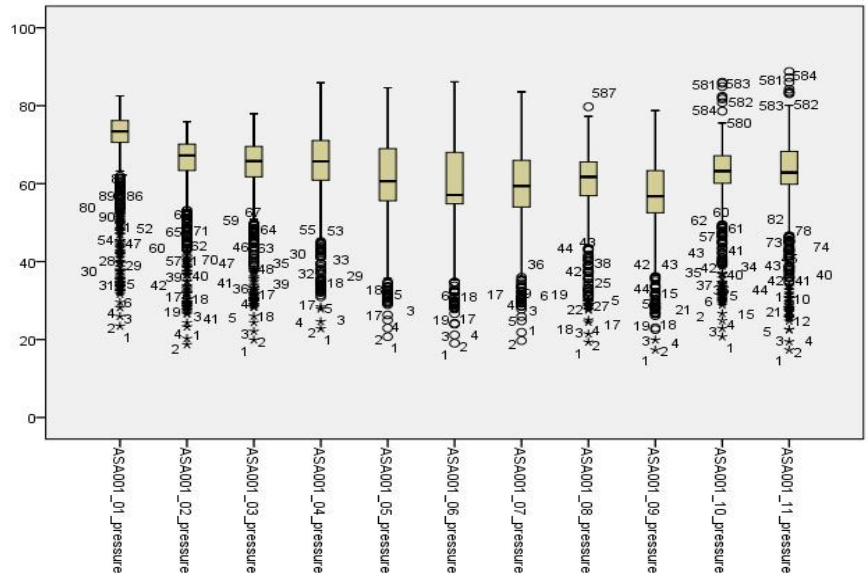

The measurements for ASA001, although reporting generally lower pressure, give roughly the same impression. Maximum values are somewhat lower than for ASA002, but they are attained at the same time. The box plots for pressure sensors 3, 4, 5 and 6 are:

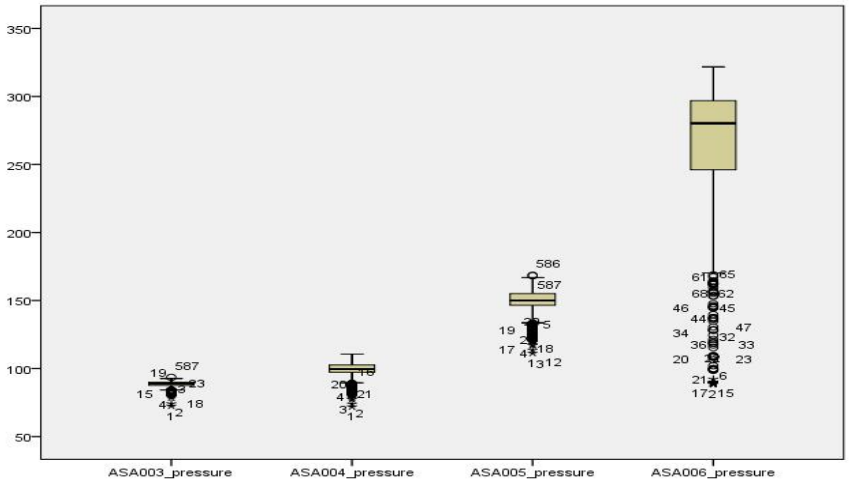

4.2.6 Water Temperature

Changes in temperature may indicate flow of water caused by piping. Pipe formation may be detected by the fact that water from the immediate environment of a sensor starts flowing through a pipe. When the pipe is forming, the sensor would detect a sudden change in temperature. Accuracy of the temperature measurements was better than 0.05 degrees Celsius.

The time series diagram of temperatures during Piping Experiment 1 is below. All collected data were in the analysis, no data points were left out.

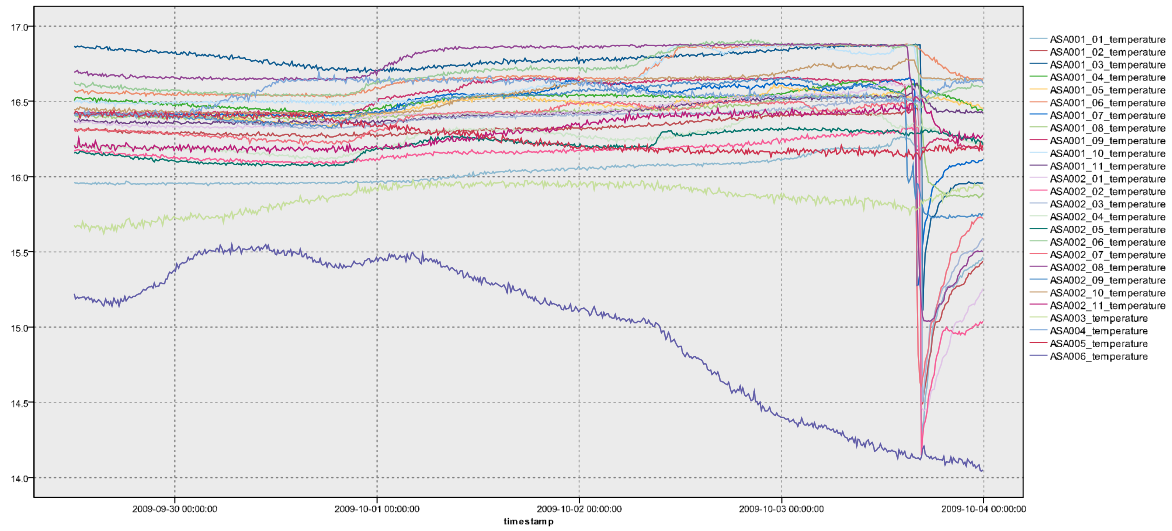

Most sensors show a sudden drop in temperature at the moment the levee collapses. Different temperature levels are reported until hours after the collapse.

The sensor reporting the lowest temperatures is ASA006, on the high water side of the levee. After the start of the experiment temperature increases by more than 0.5 degrees C, remains on the same level and then water becomes progressively colder.

It is unknown what the temperature of the water in the canal on the high side of the experiment was, but it is attractive to speculate the lower temperatures are associated with colder water from the environment starting to flow through pipes in the sand below the dike, replacing the warmer water inside the levee. Continuing this reasoning, the declining temperatures might be explained by an increasing proportion of water from the outer canal (colder water), indicating progressive widening of the pipe.

Temperature changes are much less consistent than changes in pressure. Some sensors report increasing temperatures, some do not. Perhaps these changes are related to non-uniformly distributed pipes in the process of formation. As data about location, time of formation and growth of pipes are absent, perhaps other measurements and more knowledge of dike behavior would be necessary for a better explanation of the observations.

The box plots of the temperatures show where colder water flows through the levee. The chain ASA002, located 50 cm further in the dike than ASA001, shows the following temperature distributions. ASA006, at the canal side, is included for reference.

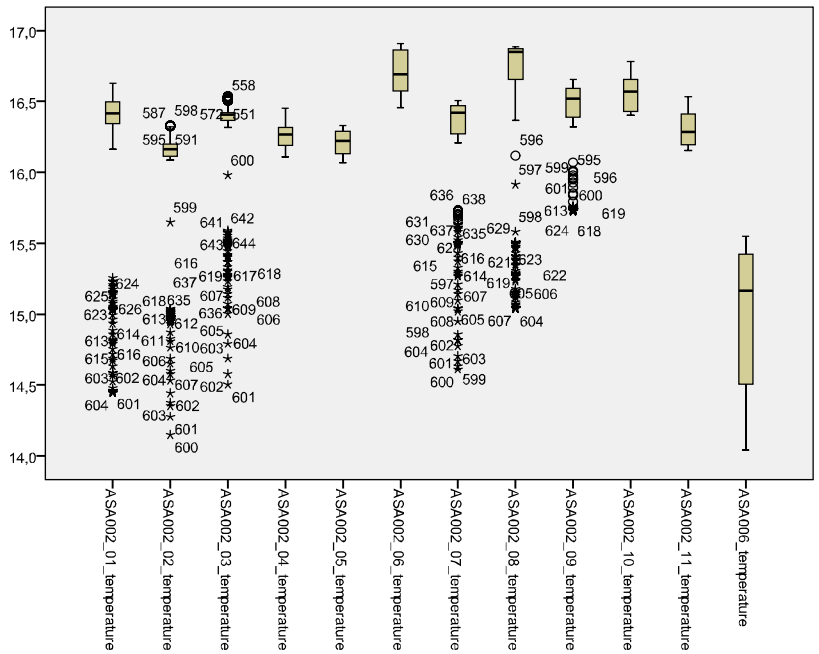

At the time of the collapse at October 3rd, 16:20h (to show outliers and extreme values all data are included) the water temperatures reach the level of ASA006 at that time for two groups of sensors. One group consists of sensors ASA002_01, 2 and 3 and the other of sensors ASA002_07, 8 and 9. This might suggest the soil around sensor ASA002_06 is more resistant (breaking streams apart) or it might suggest two pipes under the levee.

Just before the cold water arrives, the highest temperatures were observed in the sensors. The temperature readings of ASA001 are very similar to those of ASA002.

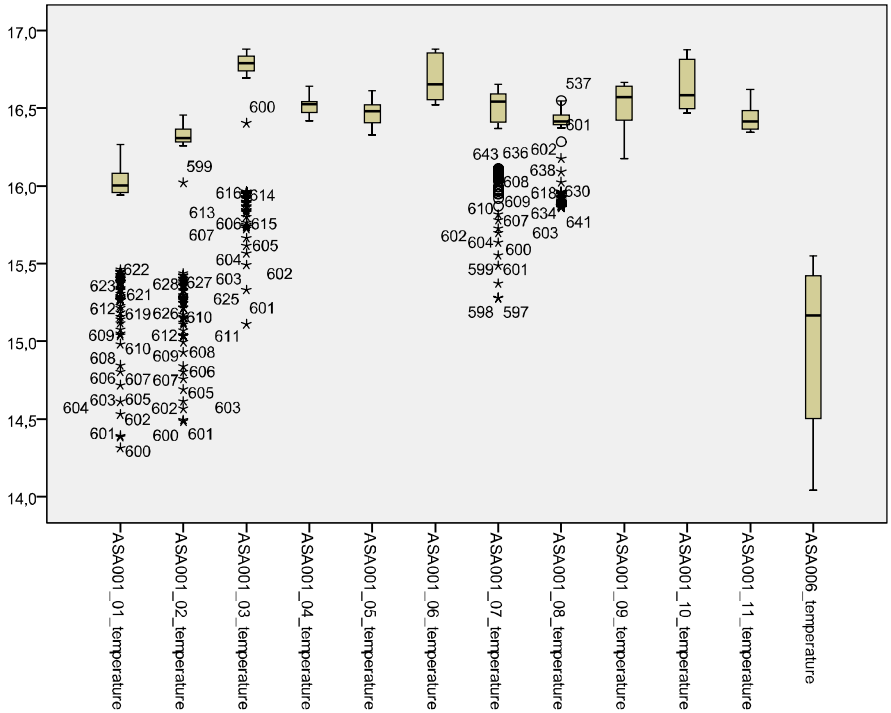

The box plots for temperature sensors ASA003, 4, 5 and 6 are:

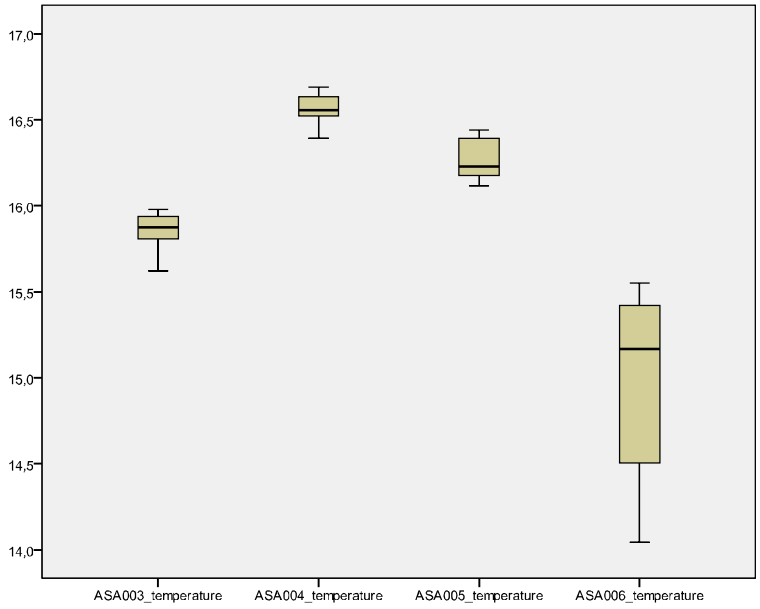

4.3 PIPING EXPERIMENT 4

In Piping Experiment 4 the same measurements were analyzed as in Experiment 1. A major difference with Experiment 1, however, is the location of the sensors.

Other measurements were collected as well, but they were not taken into account thus far, either because they seemed to have no immediate relevance for the main question or because they did not seem reliable (breaking sensor chains) or had incompatible data collection intervals.

4.3.1 Sensor locations

This experiment differed from Piping Experiment 1 in several aspects. Four MEMS sensor chains were installed, two on the high pressure side (ASB04 and ASB05), two on the lower pressure side (ASB02 and ASB03). The fact that there are two sensor chains in this experiment contrary to the single chain in Experiment 1, makes it possible to relate the measurements in time: in what way, if at all, is the behavior measured by the high-pressure chain replicated by the low pressure chain?

Apart from the two sensor chains, two individual sensors were placed further out to the high pressure (ASB01) and to the low pressure side (ASB07). All MEMS sensors measured pressure and temperature. All sensors were placed 20cm below the plane separating sand (foundation) and the clay with which the dike was built.

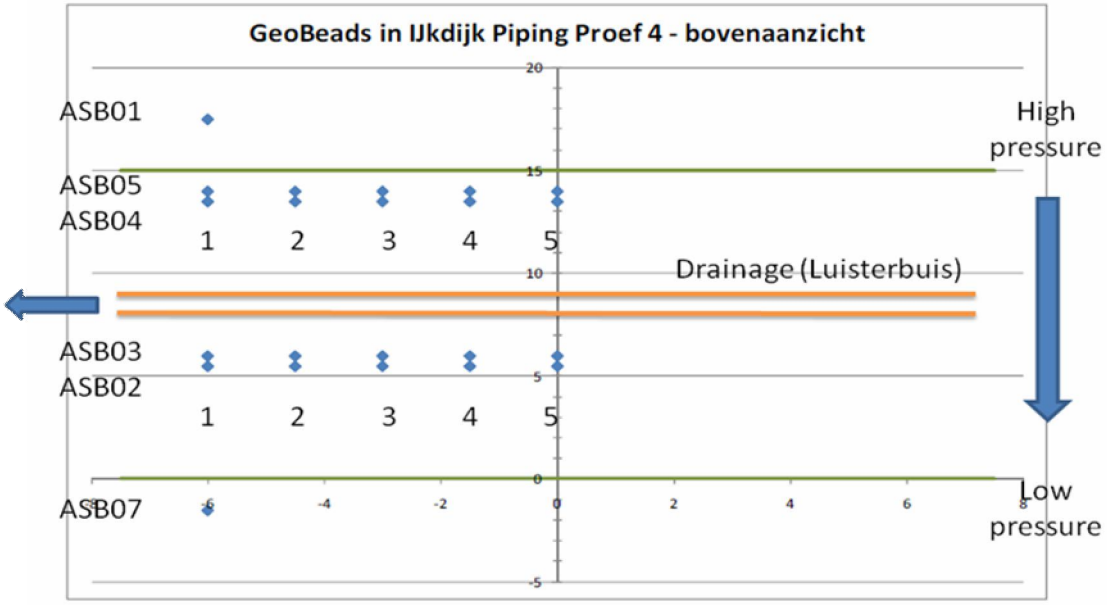

The MEMS sensor chains were shorter than in Experiment 1 and the collapse occurred not in the chains, but somewhere to the "right" of ASB02_5. This was not intended, but the data do not appear to have suffered.
A drainage tube (Luisterbuis) was placed with acoustic sensors, having the capability to extract water from the dike body. The drainage tube was placed off center slightly closer to ASB02 and ASB03 (low pressure) than to ASB04 and ASB05 (high pressure). The tube contained other sensors as well (not analyzed here). During this experiment drainage via the tube occurred three times.

Data were collected from November 30th 2009, 00:05h until December 8th, 2009, 09:35h. The levee collapsed on December 5th 2009, 16:24h. After the collapse most sensors were still functioning. Data were analyzed from the start of the experiment until December 6th, 11:45h. After that moment, data were collected at irregular moments or were missing (all zeros) sometimes.

4.3.2 Pore Pressure

The time series for the MEMS pressures for all sensors is graphed below.

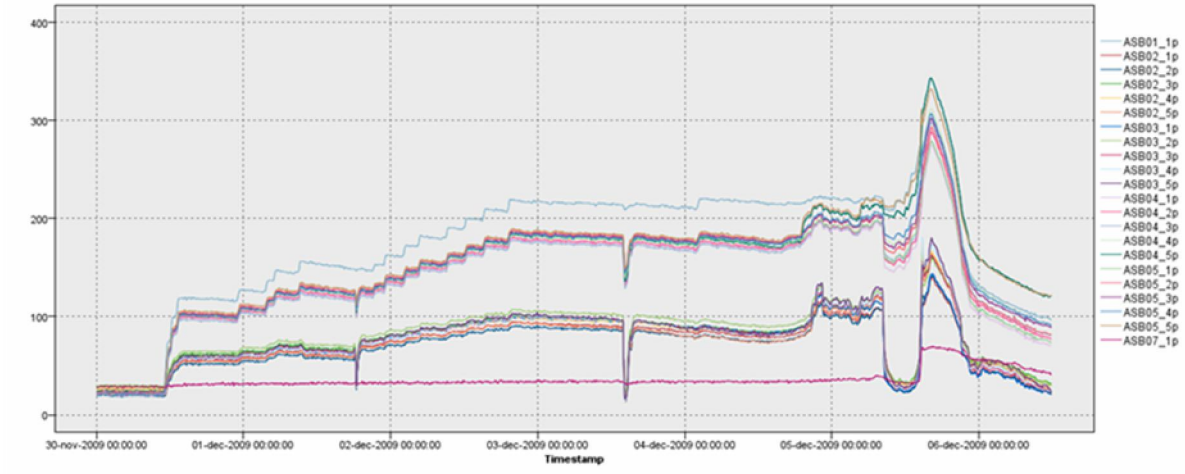

ASB01	Higher pressure	
ASB04, ASB05	...	Drainage tube has more effect on ASB02 and ASB03 than on ASB04 and ASB05
ASB02, ASB03	...	
ASB07	Lower pressure	Drainage tube off centre, closer to ASB02 and ASB03 than to ASB04 and ASB05

As in Piping Experiment 1 the sequence of pressure measurements show similarity. However, the two MEMS sensor chains show a clear difference in overall pressure, due to the placement of the sensors.
The three “dips” in the curves show the effect of drainage. The first period of drainage was relatively short. The second time drainage was applied somewhat longer and more intensely. The last drainage period took significantly longer and was more intense. Note that drainage seems to have no effect on the two outer sensors. Inside the dike, drainage seems to have more effect on ASB02 and ASB03 than on ASB04 and ASB05. This may be because ASB02 and ASB03 were closer to the drainage tube and/or had less pressure to endure than ASB04 and ASB05.

The individual sensors showed a skewed outlier pattern, very probably due to the fact that collapse occurred at one side of the sensor chains.

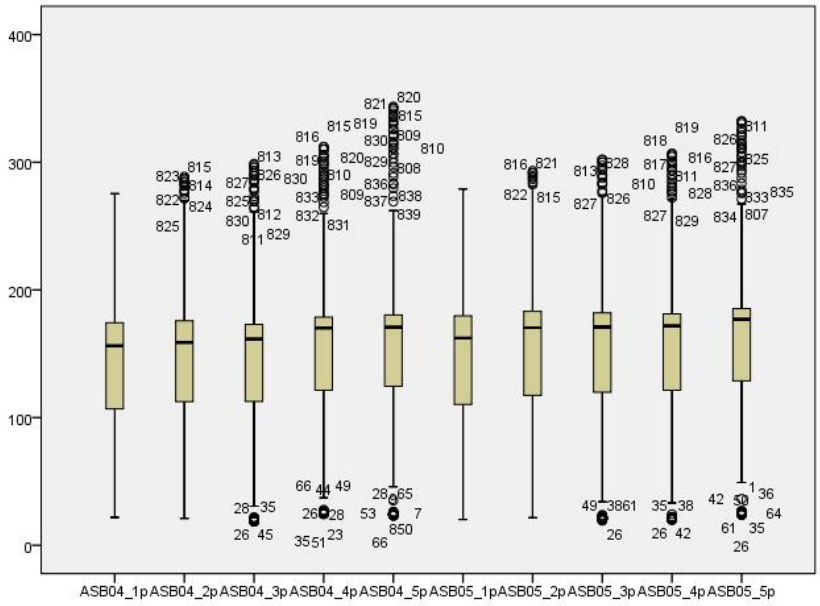

Pressure outliers clearly occur in sensors 3, 4 and 5 of both chains, suggesting collapse to the “right” of the sensor chains.

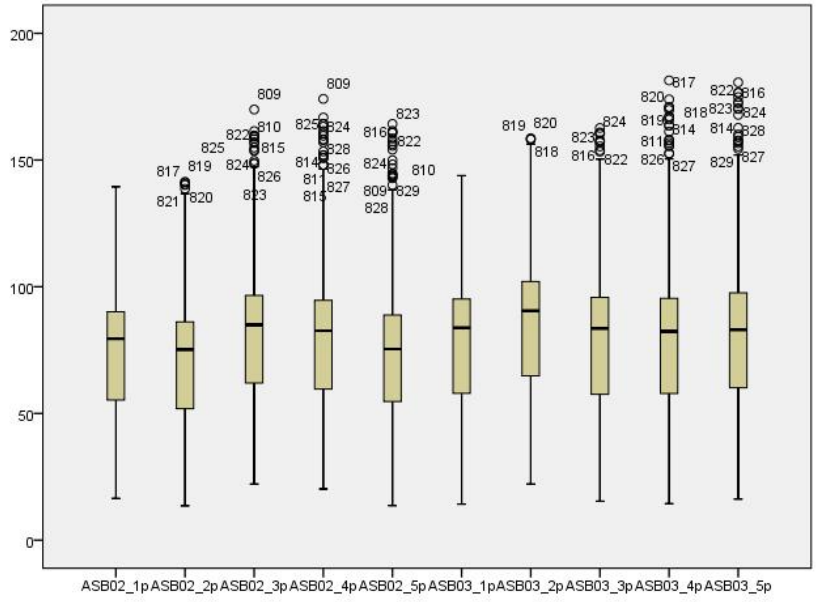

4.3.3 Temperature

As a consequence of a different sensor configuration, temperature measurements in Experiment 4 show a different pattern than in Experiment 1.

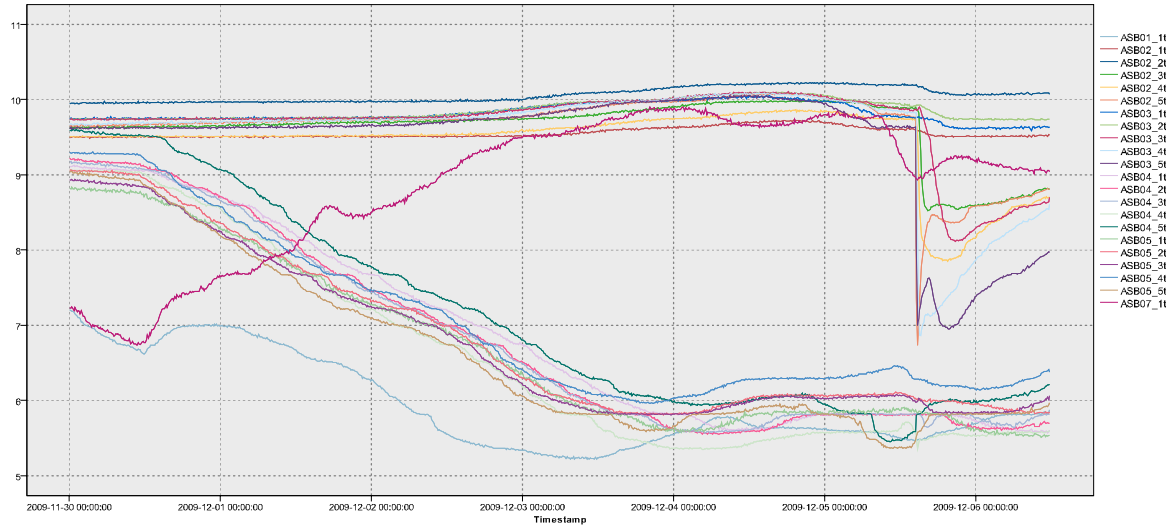

The interpretation of the measurements is easier than it was in Experiment 1. ASB01 and ASB07 initially report similar temperatures (well below the initial temperatures of the two sensor chains). They diverge during the experiment: ASB07 receives warmer water and ASB01 colder. ASB04 and ASB05 (high pressure) steadily decrease, while ASB02 and ASB03 remain constant with a sudden drop for some sensors.

ASB01 and ASB07 were placed at the toe of the levee. The initially higher temperatures reported by the chains may have been caused by the fact that water inside the levee was warmer than in the surrounding environment. Sensor chains ASB04 and ASB05 steadily report colder water, most probably representing water from the high pressure side. Meanwhile, ASB02 and ASB03 retain their high temperature, dropping sharply during collapse. Rising temperatures of ASB07 would imply that water from inside the levee is forced to the outside.

The box plots for sensor chains ASB04 and ASB05 (high pressure side) were

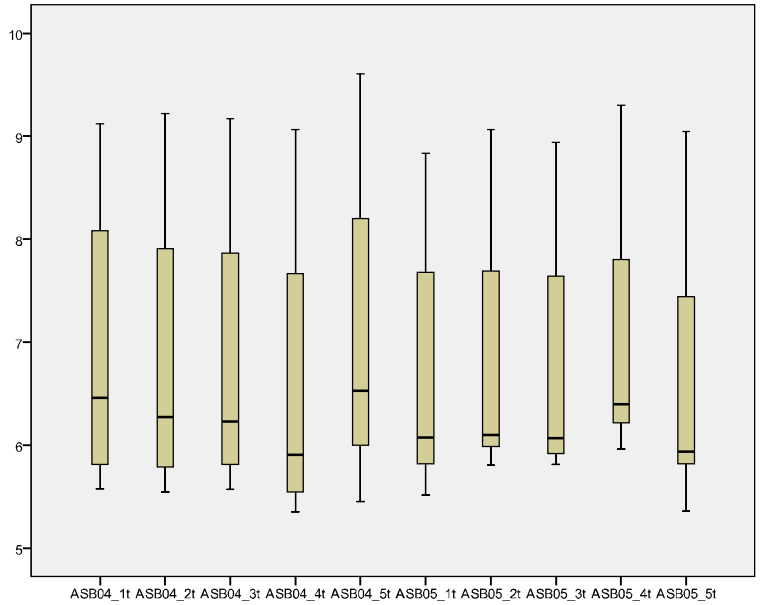

These sensors report continuously diminishing temperatures, but no outliers, i.e., no sudden wave of cold water.

Box plots show which sensors in ASB02 and ASB03 (low pressure side) reported the wave of cold water.

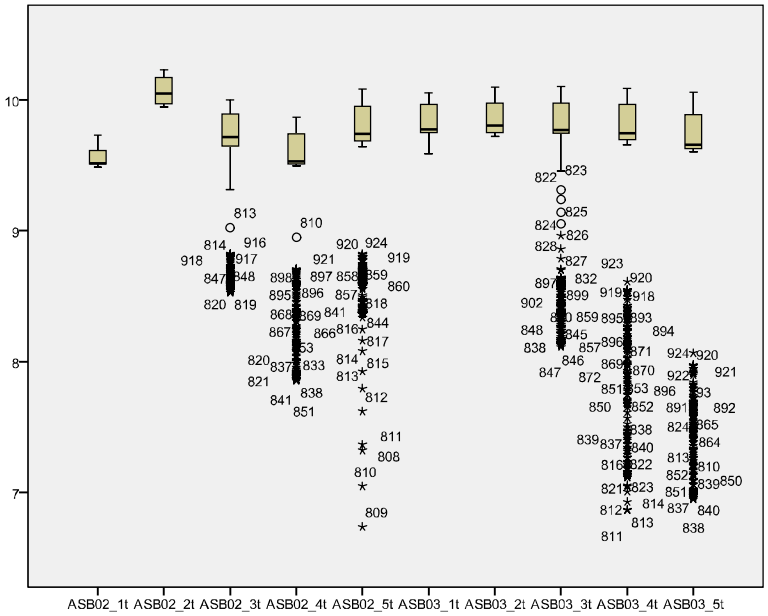

The wave of cold water passed though sensors 3, 4, and 5 of both chains, indicating again the collapse took place at the side these sensors were placed.

4.3.4 Principal Component Analysis

A general overview of the process taking place during Experiment 4 was obtained by applying PCA to the data.

It turns out that the 22 pressure variables can be described by two components. The relative importance is displayed in the table below.

	% variance	Cumulative % variance
Component 1	88.42	88.42
Component 2	7.36	95.77

Almost 96% of the pressure variations are described by two components, the first of which describes 88.5% and the second just over 7%. Both components are orthogonal. The most important component shows a general trend, the second (less important) component separates ASB002 and ASB003 (low pressure) with negative loadings and ASB04 and ASB05 (high pressure) with positive loadings. The second component seems to compensate the general trend for the high pressure sensors. A time plot for the two components shows this.

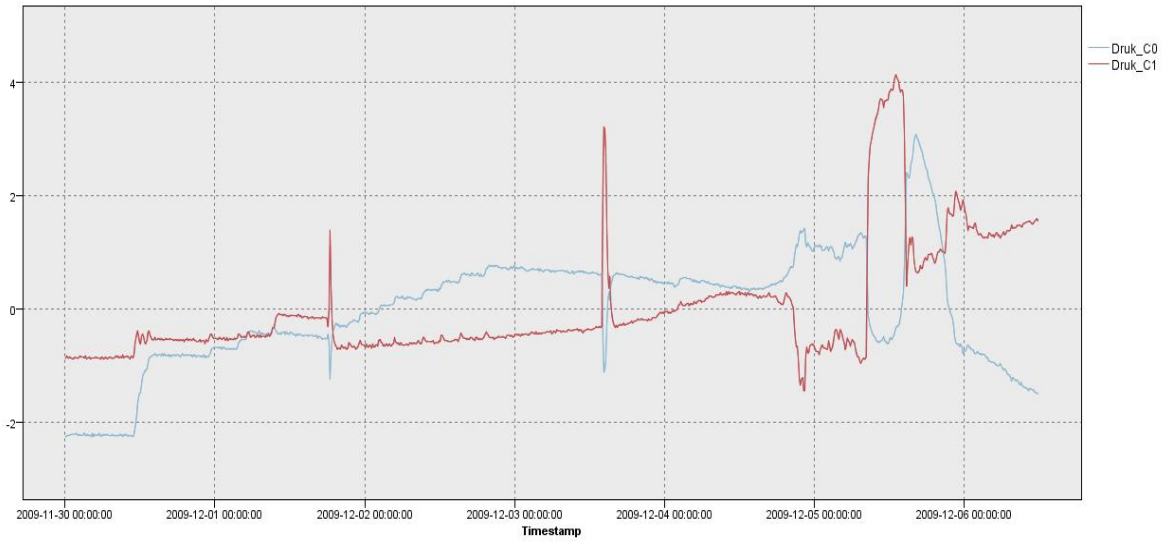

The first component is blue, the second one red, scores are standardized to mean=0, standard deviation=1. Most striking are the periods of draining, low scores for the general trend, showing the effectiveness of draining, high scores for the second component, the high pressure sensors. Note that in the first component the effect remains roughly constant, the compensating effect grows with time until it reaches 4 standard deviations. Although the absolute effect represented by the second component is small, it means that drainage has a diminishing effect for the high-pressure sensors.

PCA applied to temperature measurements showed two components as well. Their relative importance:

	% variance	Cumulative % variance
Component 1	62.23	62.23
Component 2	31.39	93.62

Almost 94% of the temperature change observations is described by two components, 62% for the first, 31% for the second. The first component separates the high pressure sensors without sudden cold water (ASB01, ASB04 and ASB05) from the sensors with lower pressure with a cold water wave.

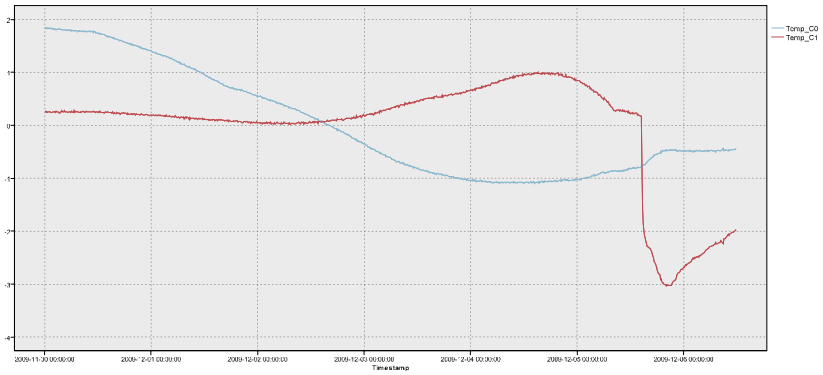

The first component (blue) shows the gradually lowering temperatures of the high pressure sensors, the second curve displays the constant temperature of ASB02 and ASB03 with a rising tendency of ASB07 and especially the wave of cold water.

These four tendencies together show a more complete picture, especially when the last drainage ends and the cold water wave occurs.

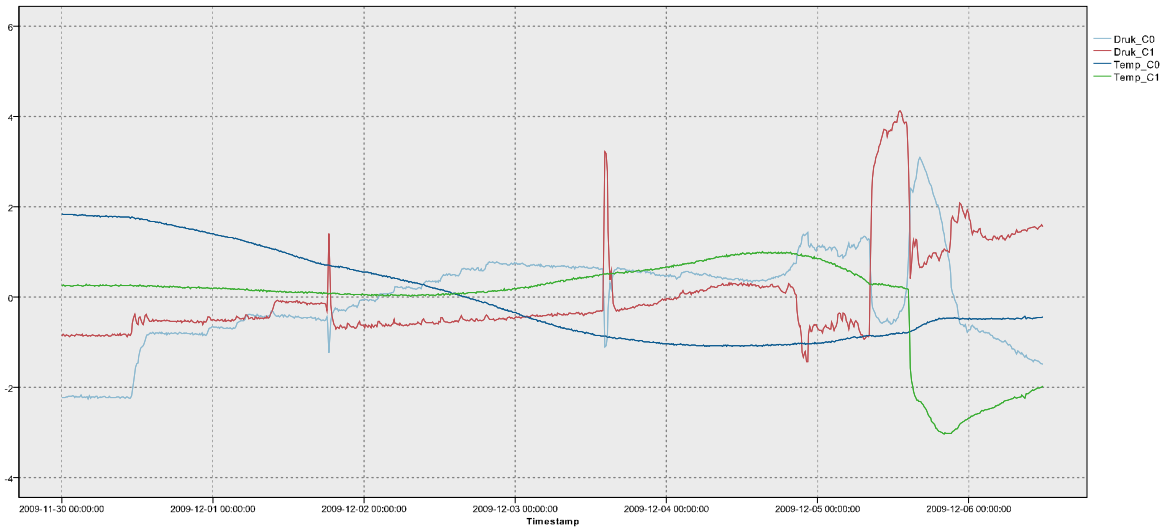

4.3.5 Pressure measurements: pr and MEMS

As in Experiment 1 pressure was measured by pr sensors (Deltares) and by MEMS (Alert Solutions). The measurements of MEMS have been discussed. The pr sensors were subdivided into three categories: WSMA, labeled WSMA_01 to WSMA_60, PRA, labeled PRA_1 to PRA_6 and finally PBA_02, PBA_03, PBA_05, PBA_06 and PBA_07.

Although a detailed analysis of the equivalence of the MEMS and pr pressure measurements fall outside the scope of this report, we would like to give an impression of the various levels of proximity of the pr pressure measurements by graphical inspection.

WSMA pressures

The pressure measurements of WSMA consisted of 60 individual measurements.

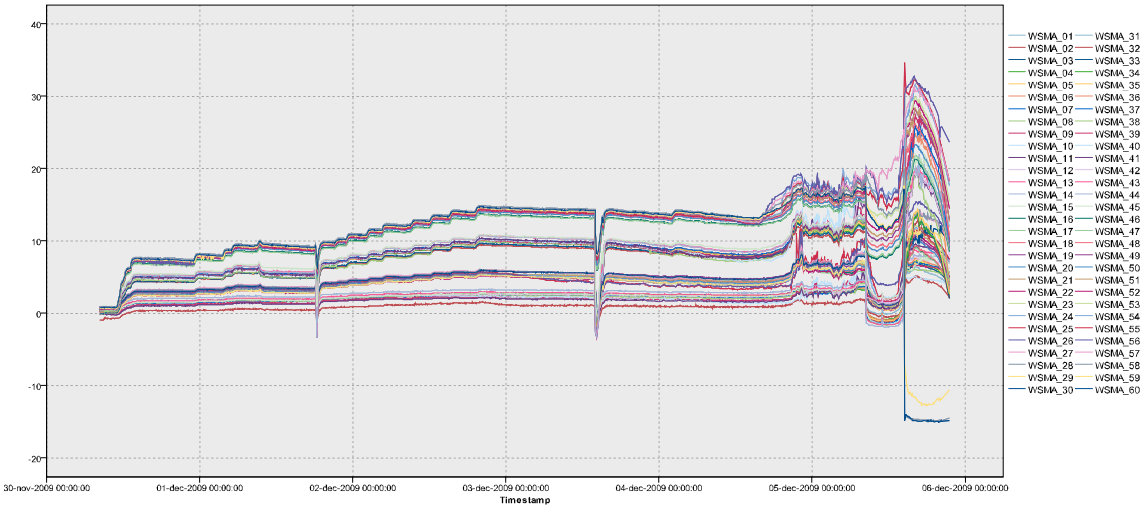

In the WSMA pressure measurements, buildup of pressure and effect of drainage is very similar to the pressure plots of the MEMS pressure measurements.

PRA pressures
The PRA pressure measurements were collected by 6 individual sensors.

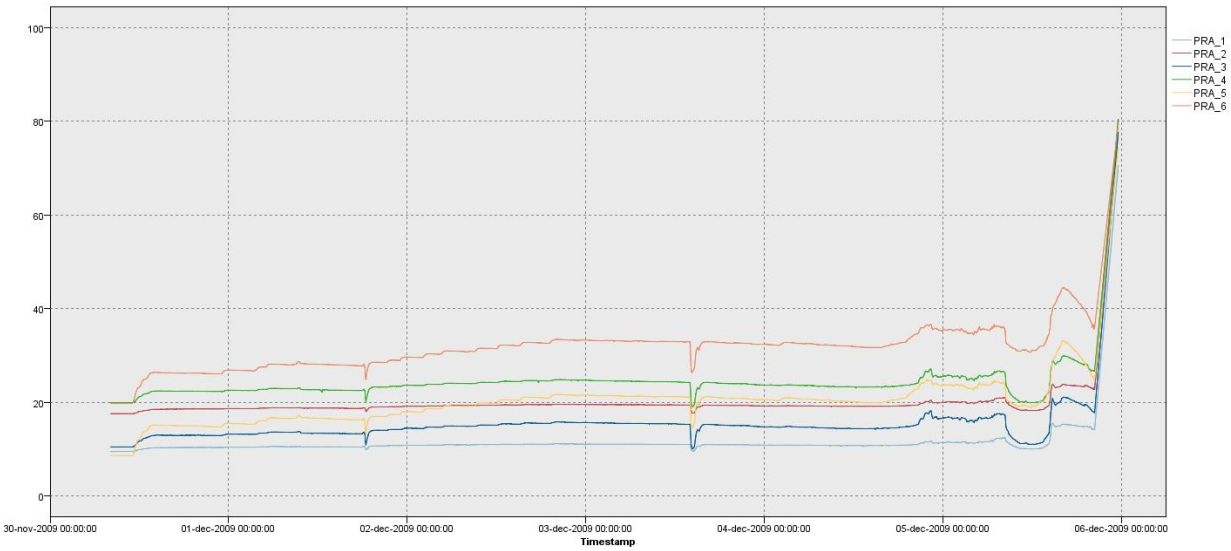

Pressure buildup is roughly the same as with the MEMS sensors, including the effect of drainage. Note that PRA_2 reports very little effect for drainage.

PBA pressures
The PBA pressure measurements were labeled PBA_02, PBA_03, PBA_05, PBA_06 and PBA_07.

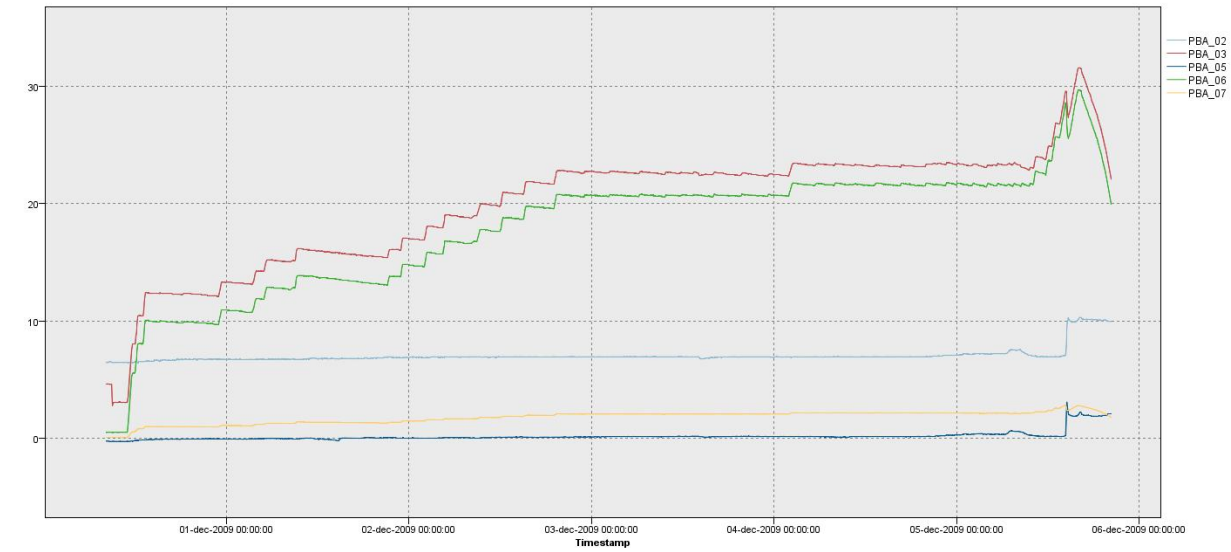

The sensors responding to pressure changes in the levee are PBA_3 and PBA_6, although effects of drainage are not visible. This is because they register the rise of the water level during the experiment. Sensors PBA_02 and PBA_05 are situated on the downstream side of the levee. On this side, the water level was kept constant by an overflow system. Hence, these sensors show little variation.

4.4 SLOPE STABILITY

The Slope Stability Experiment, performed in 2008, has many different measurements. However, the data were collected at different measurement frequencies or had incompatible time notations (Epoch times (Unix) and different character oriented date and time notations), or were hard to bring into an analyzable format for other reasons (many editing operations). For these reasons, the analysis of the Slope Stability data was beyond the scope of this effort.

If these data are to be further analyzed in the future, or new experimental data are to be analyzed, it will save time and effort to organize all data collected into an easily analyzable format before analysis starts. In this way

analysis of the data can be much more rapid and interactive. The result will be less effort for more and deeper knowledge of levee behavior.

4.5 CONCLUSION

The data for Piping Experiments 1 and 4 showed very high correlations between the pressures as measured by the pr-sensors and the MEMS sensors, justifying the result that these different ways of measuring pressure are equivalent.

Although changes in temperature are an indication of water flowing inside the levee, no clear correlations were observed between pressure and temperature. Formation of pipes in a levee implies flow of water through it is not uniform. More details of pipes would be needed to describe the relationship between changes in pressure and temperature. When sensors were placed at two sides of the levee, as in Piping Experiment 4, changes in pressure and temperature can be related in an intuitive way.

APPENDIX 5 : PIPING – SELLMEIJER RULE

5.1 LIST OF SYMBOLS

L	[m]	:	dike width
Q	[m^3/s/m']	:	discharge
V	[m^3/m']	:	volume of erosion channel
a	[m]	:	height of erosion channel
d	[m]	:	particle diameter
x,y	[m]	:	coordinates
α	[m]	:	slope of erosion channel
ϑ	[DEG]	:	bedding angle
η	[-]	:	White's coefficient
κ	[m^2]	:	intrinsic permeability
γ'_p	[kN/m^3]	:	submerged unit weight of particles
γ_w	[kN/m^3]	:	unit weight of water
φ	[m]	:	head drop

5.2 PIPING

The mechanism of piping consists of three connected processes:

- groundwater flow in the sandy layers
- pipe flow in the erosion channel
- limit equilibrium of particles at the bottom of the erosion channel

The result of a piping analysis is the value of the critical head drop across the dike. The critical head drop is the maximum possible head drop as function of the erosion length. Connected properties are the discharge and the volume of the erosion channel.

In the piping analysis some ten parameters play a role, causing a wide outcome space. In order to confine this space the approach will be normalized. To this end, the piping condition, which is derived from the condition of limit equilibrium of particles and the law of continuity of flow, is considered:

$$a^3 \frac{\partial \phi}{\partial x} = 12\kappa \int \frac{\partial \phi}{\partial y} \mathrm{d}x \qquad \frac{a}{d}\frac{\partial \phi}{\partial x} = \frac{\pi}{3}\eta \frac{\gamma'_p}{\gamma_w}\frac{\sin(\vartheta+\alpha)}{\cos\vartheta} \qquad (1)$$

This system is normalized as follows:

$$\Phi = \frac{1}{\lambda}\frac{\varphi}{L} \qquad \frac{a^3}{\delta^3}\frac{\partial \Phi}{\partial X} = \int \frac{\partial \Phi}{\partial Y}\mathrm{d}X \qquad \frac{a}{\delta}\frac{\partial \Phi}{\partial X} = 1 \qquad \lambda = \frac{\pi}{3}\eta\frac{\gamma'_p}{\gamma_w}\frac{\sin(\vartheta+\alpha)}{\cos\vartheta}\frac{d}{\delta} \qquad \delta = \sqrt[3]{12\kappa L} \qquad X = \frac{x}{L} \qquad Y = \frac{y}{L} \qquad (2)$$

λ is the resistance invariance; δ is the pore size invariance. Note, that this only is allowed, if the parameters in the erosion channel are constant. For a general piping design this is not required. But in the IJkdijk tests for the Monstercase project, proper use is made of this normalization *(2)* in order to investigate the correlation behaviour.

By implication, the normalized solution will take the following form:

$$\frac{1}{\lambda}\frac{H}{L} = \mathrm{f}_H\left(\begin{matrix}\text{scaled geometry}\\ \text{permeability ratio}\end{matrix}\right)$$

$$\frac{1}{\lambda}\frac{Q}{kL} = \mathrm{f}_Q\left(\begin{matrix}\text{scaled geometry}\\ \text{permeability ratio}\end{matrix}\right) \qquad (3)$$

$$\frac{V}{\delta L} = \mathrm{f}_V\left(\begin{matrix}\text{scaled geometry}\\ \text{permeability ratio}\end{matrix}\right)$$

f is the normalized flow solution for the head drop $_H$, the discharge $_Q$,and the volume $_V$. This solution only depends on the scaled geometry and the permeability contrast of the soil layers.

The result of computation for the IJkdijk geometry is presented in Figure 1. The green line represents the head drop, the blue one the discharge and the red one the channel volume. The charts may be used for all tests 1 … 3, as their geometry is similar. Test 2 has a slightly thinner sand layer. However, this has a minor effect on the outcome.

The dotted lines are produced by MSeep. These lines are used in the correlation process. Only the stable range of the erosion path is relevant (here the normalized erosion length smaller than 0.233).

In a later stage it is the intention to apply the correlation to more general geometries. Then, characteristic points of the presented lines only will be at hand. The full line must be determined by mathematical formulae. The solid lines in the charts represent such formulae. These lines are accurate in the stable range. Beyond that range, they quickly diverge.

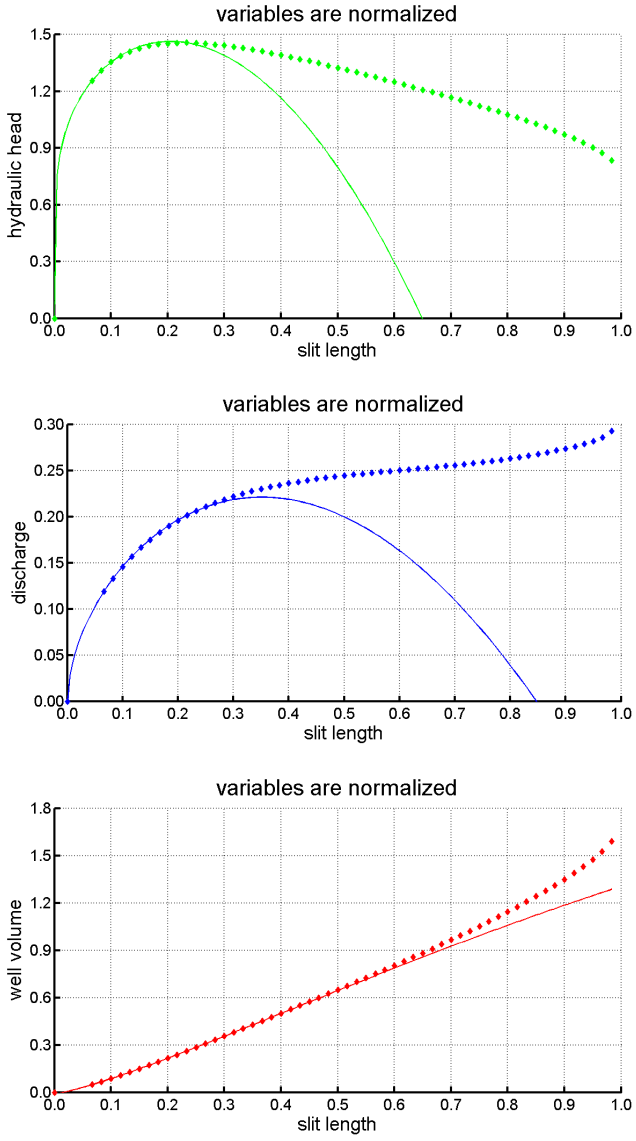

Figure 1 Normalized piping variables as function of erosion channel length

APPENDIX 6 : REMOTE SENSING TECHNIQUES – SAR AND INSAR

The SAR and InSAR text is provided by Fugro NPA.

6.1 SATELLITE SAR

6.4.1 Synthetic Aperture Radar

Radar instruments emit pulses of electromagnetic radiation in the radio and microwave part of the spectrum and detect the reflection of the pulses from objects in its line of sight (LOS). One class of radar instrument is imaging radar, and includes Synthetic Aperture Radar (SAR).

A SAR signal can be imagined as a sine wave, which contains amplitude and phase information (Figures 1 & 2). The amplitude is the strength of the radar response. The phase is the fraction of a complete sine wave cycle. When the sine wave starts to repeat itself, one cycle of phase has occurred. Many SAR applications make use of the amplitude of the return signal, and ignore the phase data. Examples include land cover classification, shipping lane tracking, oil slick detection and feature identification. Interferometry makes use of the phase data.

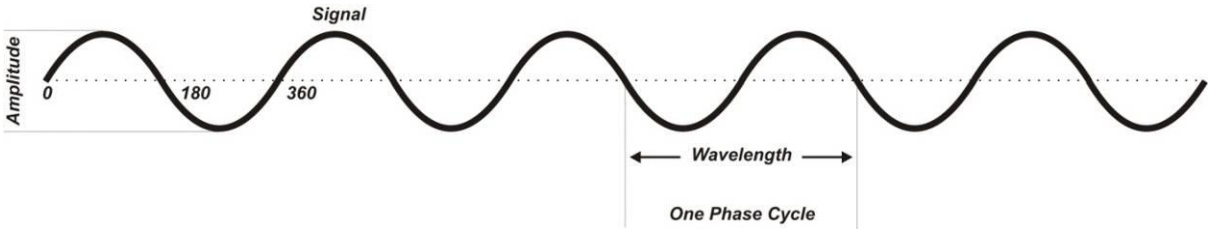

Figure 1. Radar signal - Amplitude and Phase.

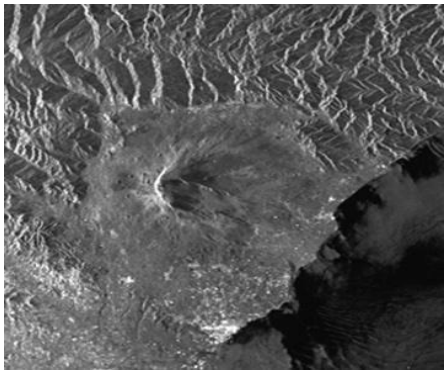

Figure 2a. SAR amplitude image.

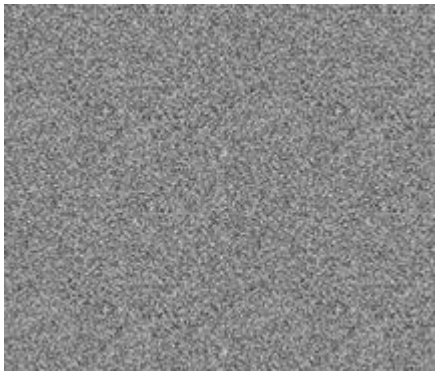

Figure 2b. SAR phase image.

Since the outgoing wave is produced by the satellite, the phase is known, and can be compared to the phase of the return signal. The phase of the return depends on the distance to the ground, since the length to the ground and back will consist of a number of whole wavelengths plus a fraction of a wavelength. The total distance to the satellite (i.e. the number of whole wavelengths) is not known, but the extra fraction of a wavelength (the phase) can be measured extremely accurately.

6.4.2 Geometry

SAR satellites are predominantly in near-polar orbits. The direction of motion with respect to north is known as the *satellite heading.* Figure 3 shows an example of an ascending and descending satellite heading (or azimuth track). The SAR beam images at 90 degrees from the direction of flight.

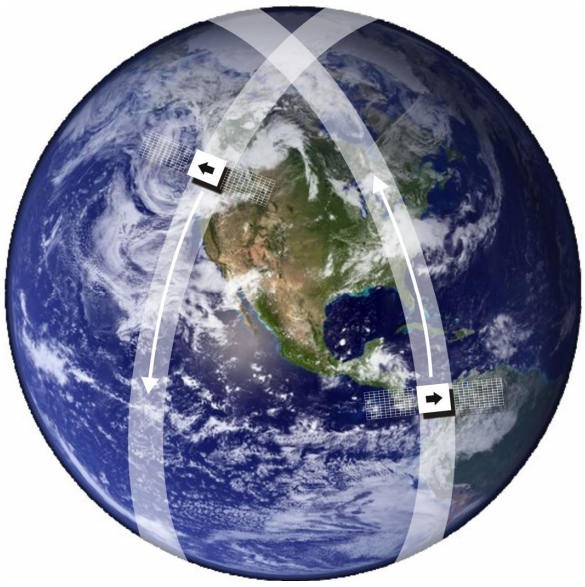

Figure 3. Ascending (southeast to northwest) and descending (northeast to southwest) satellite tracks. SAR imaging direction indicated by black arrows.

The SAR sensor is side looking i.e. at a right angle to the flight direction of the satellite. The viewing angle of the radar beam is known as the look angle. Figure 4 shows the geometry of a SAR acquisition. Range is the LOS distance between the radar and the ground. Slant range is the distance from the radar towards each target, and is measured perpendicular to the satellite track. Ground range is the same distance, projected using a geometrical transformation onto a reference surface such as a map. The azimuth is also known as along-track direction. The azimuth direction is perpendicular to the range direction. The portion of the image closest to the radar platform is called the near range, while the portion of the image farthest from the nadir (vertical) is called the far range.

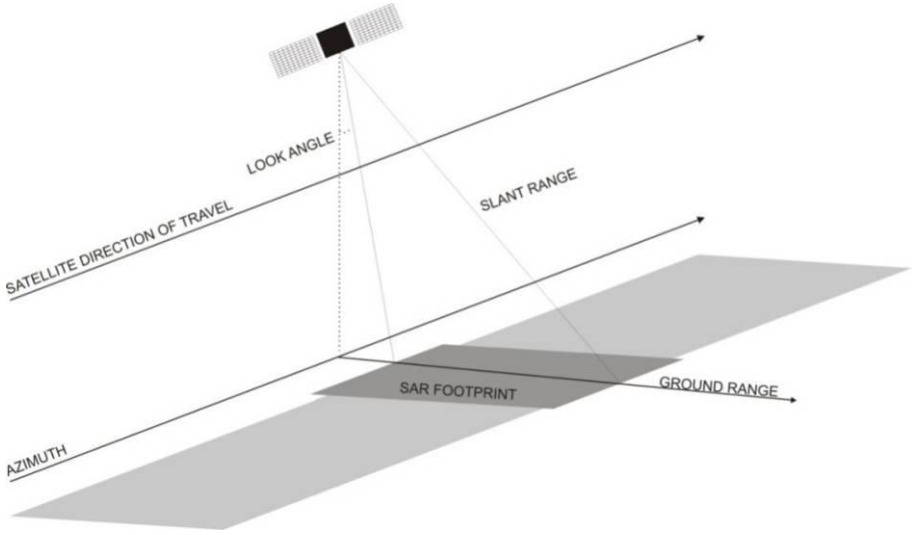

Figure 4. The geometry of a SAR acquisition.

SAR data can be acquired in a number of different imaging modes (Figure 5 provides an example for Envisat). Some modes allow for the SAR instrument to be pointed at different look angles (typically between 20 degrees and 50 degrees from nadir). These are known as beam modes. Steep look angles will predominantly detect

vertical movements, and a small component of horizontal movements. Shallower look angles are most suited to vertical movements but will capture greater portions of any horizontal component of motion. It is worth noting that InSAR can only be performed on SAR images acquired in the same track (travel direction) and frame (imaging footprint) and imaging mode.

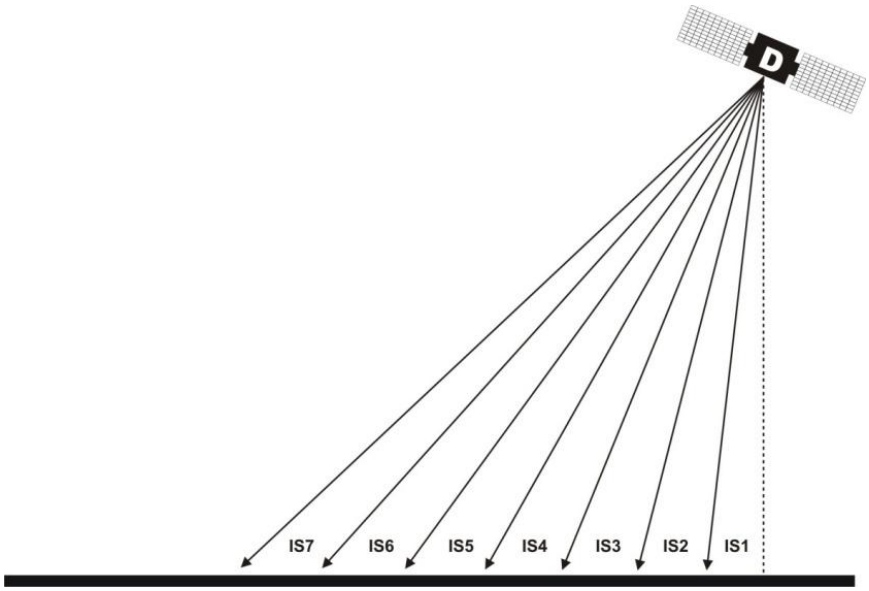

Figure 5. The approximate look angles of each available beam mode for the Envisat satellite. D = Descending satellite track.

6.4.3 Topography

Significant variations in topographic height can cause distortions in SAR images due to the viewing geometry of the SAR instrument. Hill or ridge slopes facing the SAR satellite can be subject to distortion, known as foreshortening and layover. Both are expressed as a compression or "thinning" of slopes facing the SAR satellite, and an elongation on the opposite side. The same hills and ridges can also act to obscure areas from view (known as shadowing).

6.4.4 Radar Wavelength

Radar can be transmitted at a number of different wavelengths. The most common SAR satellites transmit C-band radar (5.6 cm), but X-band (3.1 cm) and L-band (23.6 cm) SAR instruments are also available.

6.4.5 Data Sources

A wide variety of SAR data is available from a large number of earth observation satellites, operated by both public institutions (such as national or regional space agencies) and private commercial companies. Table 1 reviews the specifications of the key SAR satellite missions.

Sensor	Radar wavelength	Lifespan	Spatial resolution (m)	Revisit time (days)	Scene size (km)	Programmable
ERS-1	C-band	1991 - 2000	30	35	100 x 100	No
ERS-2	C-band	1995 -	30	35	100 x 100	Yes
Envisat	C-band	2002 -	30 to 150	35	100 x 100 to 400 x 400	Yes
RADARSAT-1	C-band	1995 -	10 to 100	24	50 x 50 to 500 x 500	Yes
RADARSAT-2	C-band	2007 -	3 to 100	24	20 x 20 to 500 x 500	Yes
JERS-1	L-band	1992 - 1998	18	44	75 x 75	No
ALOS PALSAR	L-band	2006 -	10 to 100	46	30 x 30 to 350 x 350	Yes
TerraSAR-X	X-band	2007 -	1 to 16	11	10 x 5 to 100 x 1500	Yes
COSMO-SkyMed	X-band	2007-	1 to 100	1 (at best)	10 x 10 to 200 x 2000	Yes

Table 1. Specifications of the key SAR satellite missions

6.2 SATELLITE INSAR

6.4.6 Interferometry

If we collect two separate images of a point on the ground from exactly the same position in space, with nothing on or around the point changing, the two signals would be expected to have the same radar amplitude and phase values.

In practice, the position of the satellite between two image acquisitions is never identical, and the corresponding difference in the path (distance between satellite and ground) means there is a difference in phase between the two signals; this is called a phase shift (Figure 6). The difference in position of the satellite between image acquisitions is known as the perpendicular baseline (B_{perp}), illustrated in Figure 7.

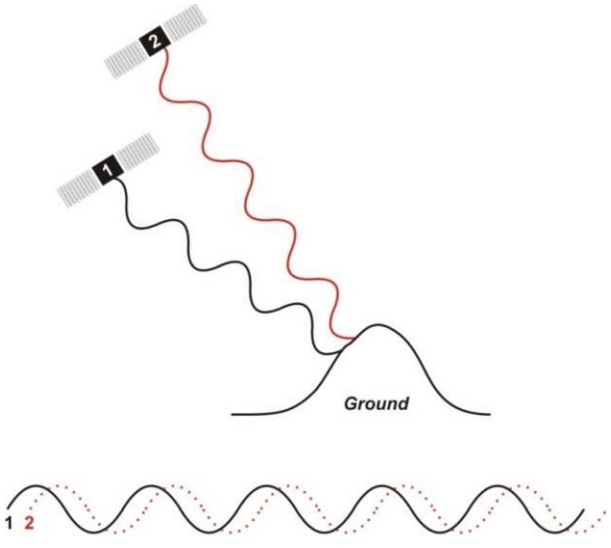

Figure 6. Phase shift between two SAR image acquisitions.

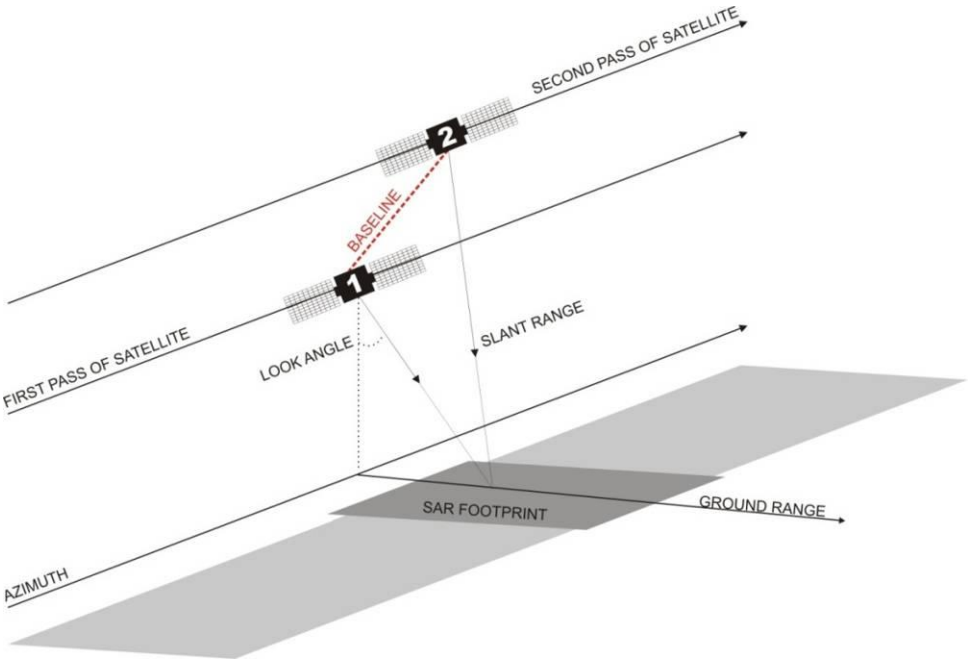

Figure 7. InSAR geometric configuration.

SAR interferometry makes use of phase information by subtracting the phase value in one SAR image from that of the other, for the same point on the ground. The resulting phase difference is directly related to the topography and any movement of the ground in the direction of the satellite LOS and this is represented as fringes. An interferometric fringe can be thought of as a collection of contours, with each fringe corresponding to a phase difference of 0 to 360°. The resulting image is called an interferogram.

Each complete interferometric fringe cycle represents a specific elevation interval (Figure 8). This elevation interval is a factor of the radar wavelength, satellite altitude, viewing angle B_{perp} and is called the altitude of ambiguity. There is a maximum B_{perp} that can be used in interferometry and this varies with the satellite and beam mode used.

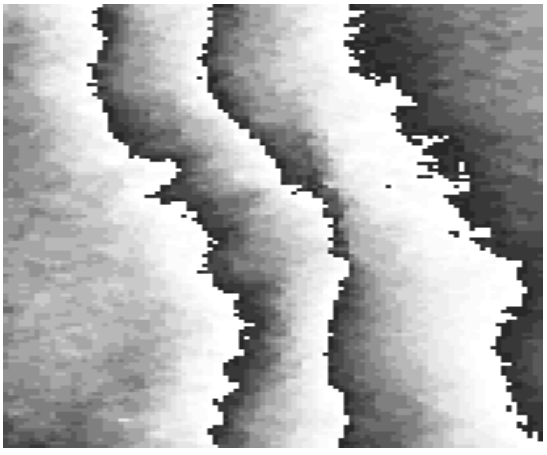

Figure 8a. Interferometric fringes – gently sloping topography.

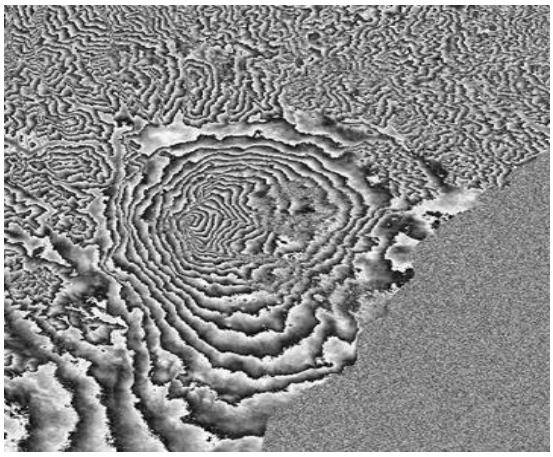

Figure 8b. Interferometric fringes – Mountainous terrain.

6.4.7 Differential Interferometry

SAR interferometry can be used to estimate topographic height, providing the assumption is made that no movement has occurred between SAR image acquisitions. This technique can also be applied to map any ground movement as surface displacements will cause an additional phase shift. This is known as differential interferometry.

To measure surface deformation, an initial interferogram is created representing topography. This can be achieved using a pre-existing Digital Elevation Model (DEM) to simulate the topographic contribution to the phase, or by creating an interferogram using two SAR images prior to any ground movement. A second interferogram is then created spanning the period of movement. This will contain topographic and displacement information. By subtracting one interferogram from the other, fringes that relate to common topography cancel each other out. The phase differences that remain as fringes in the differential interferogram are a result of range changes of any displaced point on the ground from one interferogram to the next. The result is a wide-area map of changes, the maximum size of which is determined by the original SAR images.

Any surface displacement away from the satellite LOS causes an increase in the path (and therefore phase) difference. Any surface displacement toward the satellite LOS causes a decrease in the path (and therefore phase) difference.

Owing to the two-way journey of the signal from and back to the satellite, the change in distance is measured twice in terms of displacement in units of wavelength. In the differential interferogram a fringe cycle corresponds to a displacement relative to the satellite LOS of only half the radar wavelength.

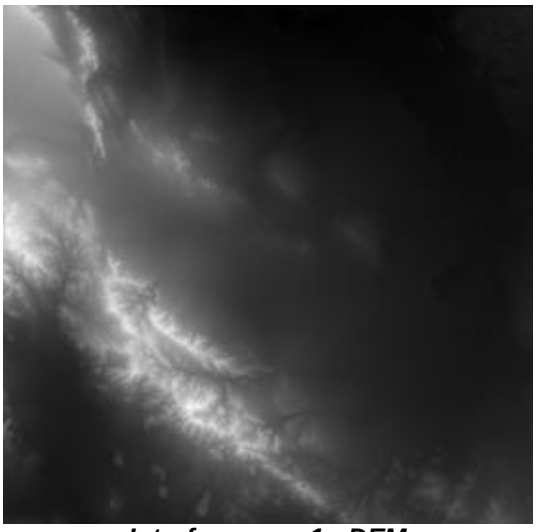

Interferogram 1 - DEM
Interferogram synthesised from a Digital Elevation Model

Differential Interferogram
DEM (topography) eliminated. Differential interferometric fringes represent displacement i.e. motion towards and away from the satellite)

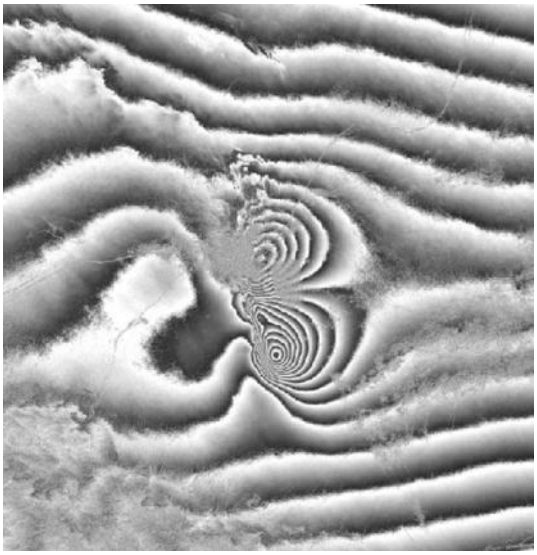

Interferogram 2
Interferogram created from two SAR images spanning the deformation event. Represents topography and displacement (interferometric fringes represent topographic and displacement contours)

Figure 9. Stages of Differential InSAR processing.

6.4.8 Unwrapping

The phase value is not known absolutely, but is given in the range 0-360 degrees. In order to compute terrain heights and generate a DEM or to produce a displacement map showing motion in millimetres per year, fringes have to be unwrapped i.e. the correct multiple of 360 degrees must be added to the phase difference at each pixel (Figure 10). Phase unwrapping is a complex process and can lead to ambiguities in results.

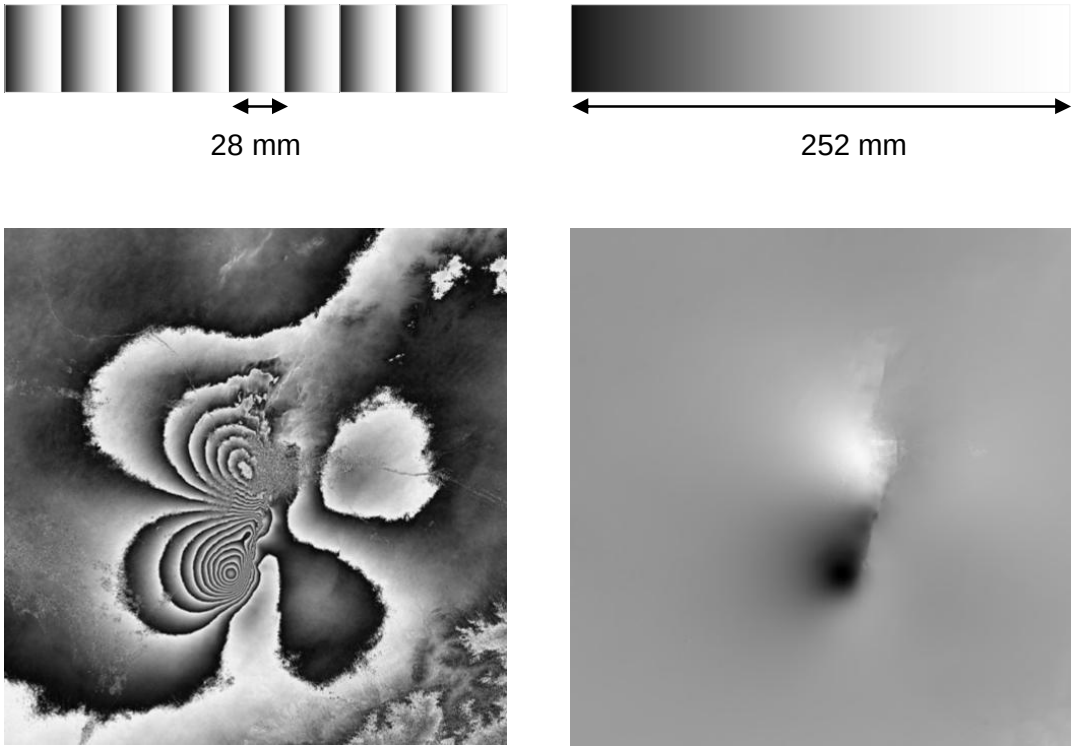

Figure 10. Wrapped (left) and unwrapped (right) C-band interferogram.

6.4.9 Potential Error Sources

Atmosphere
Water vapour in the atmosphere causes a delay to the SAR signal as it passes through. The characteristics of the atmosphere are not invariant and apart from gross changes between SAR image acquisitions, subtle variations can occur on a smaller geographic scale typically in order of 5-20km^2. These variations can cause small phase variations in interferograms, typically between 1/3 to 2 phase cycles.

Orbits
The fringes in an interferogram are not only a result of the surface topography but also of the Earth's curvature and acquisition geometry. An interferogram is said to have been "flattened" when the fringe and phase effects due to the different position of the satellite and the shape of the Earth's ellipsoid have been eliminated and only fringes due to topography and/or deformation remain. This relies on an accurate knowledge of the position of the satellite(s) at the time of each acquisition. The best available reference data is nominally accurate to a few radar wavelengths. However, uncompensated positioning errors can occur, varying slowly on a scale of a few wavelengths over a 100 km scene. These positioning errors are compounded with subtle changes in the average refraction characteristics of the atmosphere. The overall effects are observed as slowly varying (and usually near-linear) large-scale phase trends across interferograms. Orbital phase trends are compensated for using de-trending algorithms.

DEM
In differential interferometry, the topographic signal is usually simulated and removed using a DEM. The magnitude of topographically related phase errors is therefore a function of the quality of the DEM. The severity of topographic errors is reduced by choosing interferograms with a smaller B_{perp}.

The magnitude of DEM errors can also be reduced by using DEMs with greater spatial resolution than the SAR images, and DEMs with a high vertical accuracy, such as LiDAR DEMs.

6.3 ADVANCED INSAR TECHNIQUES

6.4.1 Persistent Scatterer Interferometry

Persistent Scatterer Interferometry (PSI) is a non-invasive surveying technique capable of measuring millimetric motions of individual Earth surface features over wide-areas in both urban and semi-urban environments. PSI exploits the fact that a substantial global archive of satellite SAR images acquired by a number of different satellites exists. This means that over some areas of the world many tens of radar scenes have been acquired over the same places, providing large, multi-temporal data-sets from 1991 to the present day.

The PSI approach identifies common geographical locations in each SAR image of the multi-temporal data stack that reliably and persistently reflects the radar signal back to the satellite. These locations generally correlate to man-made structures such as buildings, bridges, pylons, etc., though they can also include bare rocks and outcrops. Each feature is called a Persistent Scatterer (PS). They act as PS because of their serendipitous geometry, surface-roughness and electrical conductivity, and the exact locations and densities of PS cannot be predicted in advance of processing. However, over urban areas PSI typically yields 100s of PS per km^2. The PSI algorithm compares differences in phase information for each PS across all SAR images in a data stack to derive their individual motion. Variables, such as refraction of the radar signal by atmospheric water vapor, can change the radar signal path length and hence the phase information, leading to errors. However, statistical computation of 'atmospheric phase screens' for each SAR image aims to correct these artefacts and is a vital part of the PSI approach.

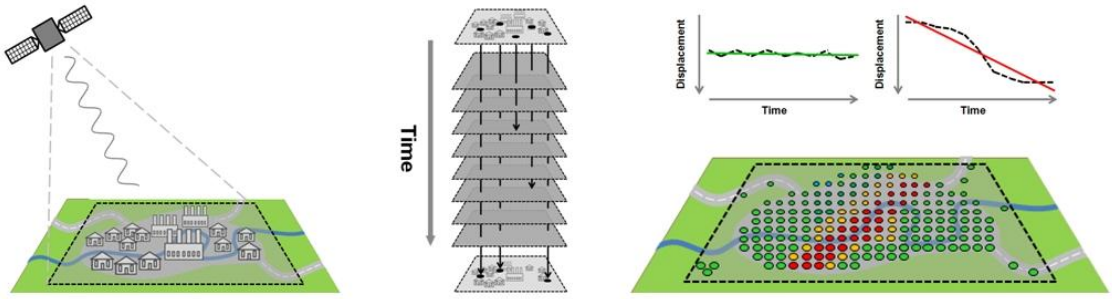

Figure 11. PSI technique.

The PSI technique takes conventional differential interferometry a step further by modelling atmospheric, orbital and Digital Elevation Model (DEM) errors to derive relatively-precise displacement and velocity measurements across networks of PS. A unique benefit of PSI is its ability to provide average annual motion rates (velocity) as well as multi-year motion histories for individual PS, a time-series. The Terrafirma Validation Project demonstrated that PSI results and ground levelling were comparable, revealing a velocity Root Mean Square Error (RMSE) of 1.0 – 1.8 mm/yr and time-series RMSE of 4.2 – 6.1 mm.

Figure 12. Section of a PSI average annual motion over London, UK.

6.4.2 PSI Processing Workflow

The typical PSI processing workflow comprises of the following steps:

1. SAR data search, ordering & copying to Linux machine
2. Raw SAR data processing
3. Master scene selection and image resampling
4. Point list generation
5. Generate point interferograms
6. Import DEM
7. Initial baseline correction
8. Generate initial point differential interferograms
9. Reference point selection
10. Initial model creation (multiple reference point)
11. Model and baseline refinement (multiple reference point)
12. Phase unwrapping and model refinement (single reference point)
13. Non-linear deformation estimation and model refinement (single reference point)
14. Atmospheric correction and model refinement (single reference point)
15. Convert phase to velocity and motion time-series
16. Coarse geocoding
17. Database export
18. GIS import
19. Refine georeferencing
20. Format final deliverables

Figure 13. Basic PSI processing workflow.

6.4.3 Constraints Of Persistent Scatterer Interferometry

Although PSI is a powerful technique for mapping ground and structure motion it does have a number of constraints:

- Data quantity and temporally sampling frequency – PSI relies on a large number of multi-temporal SAR scenes. Poor temporal distribution of SAR data and/or gaps in the data stack will lead to less precise assessment. For some motion types, such as rapid collapse of mine workings or quick dike failures, the frequency of satellite revisit may not be sufficient to accurately monitor the phenomena in question. The spatial extent of any motion phenomena is also a key consideration.
- PS location and density – The number and location of PS cannot be predicted before processing, as a good 'back-scattering' point depends on the geometry and properties of the target in relation to the satellite. The majority of PS are back-scattering features on the ground, such as buildings

or rocky outcrops, and do not represent the ground itself. The motion recorded may represent the motion of a specific feature, the ground upon which it is located or a combination of the two

- High motion rates – The ability of PSI to measure motion is fundamentally limited by the temporal sampling of the SAR data and the fact that phase is wrapped in a set range. For C-band SAR PSI cannot resolve motion greater than 14 mm between two acquisitions, meaning maximum velocities of 14.8 cm per year for ERS-1/2 and Envisat.
- Significantly non-linear motion – Standard PSI processing assumes motion that is largely linear in nature, and although it is possible to capture small amounts of non-linear motion, PSI will struggle where a lot of non-linear motion is present.
- Topography – Steep slopes can lead to common SAR data limitations of layover, foreshortening and radar shadow.
- Motion vector – Motion can only be measured in the viewing geometry (Line of Sight) of the satellite.
- Unresolved atmosphere – Not all components of atmosphere may be successfully characterised.
- Residual orbit trends – Residual orbital trends or tilts can be a feature of PSI processing that arises from uncompensated orbital inaccuracies used within the PSI processing chain.

6.4 DELIVERABLES, GIS INTEGRATION & INTERPRETATION FOR PSI

6.4.1 Velocity & time series for PSI data

The PSI data is provided in the following data formats

- Database (.dbf)
- ArcGIS shapefile (.shp)
- Google Earth (.kmz)

The PSI database (.dbf) covering contains the following fields:

- CODE – PS unique identifier
- LATITUDE – Latitude coordinate of PS in WGS84/Geographic
- LONGITUDE – Longitude coordinate of PS in WGS84/Geographic
- HEIGHT – Height estimate of PS (m) with respect to the stable reference area
- VEL – Average annual motion rate (mm/year) in the satellite LoS
- ERROR_HGT – Estimated height uncertainty (m)
- ERROR_VEL - Estimated average annual motion rate uncertainty (mm/year)
- OFFSET – Shift applied to the time series so that the motion is measured from the first SAR image (mm)
- For this data set: _25_Jan_04 – PS motion relative to 25th Jan 2004 and stable reference area (mm)
- ….
- _14_Dec_08 – PS motion relative to 25th Jan 2004 and stable reference area (mm)

6.4.2 GIS integration

The deliverable can be easily ingested into a GIS using the Easting and Northing coordinates of the PS. PS points can then be styled and analysed using the average annual motion rate. Time series can be created for each PS by plotting the PS motion relative to 25th Jan 2004 (for the current data set) and stable reference area for each of the analysed SAR image dates.

6.4.3 Time series analysis

A time series for each PS point can be created by plotting the measured displacement of each PS point at each date. The displacement derived from the average annual velocity can also be plotted. The displacement at each image date, D_t, estimated from the average annual velocity is:

$$D_t = \left((C \times VEL) - OFFSET\right) + \left((T_t - T_1) \times VEL\right)$$

Where T_t is the time in years at each image date and T_1 is the time in years at the first image date. C is a fixed constant. For the PSI data discussed in chapter 4 in this result C = -2.39.

Below is an example of time series data converted into a displacement graph:

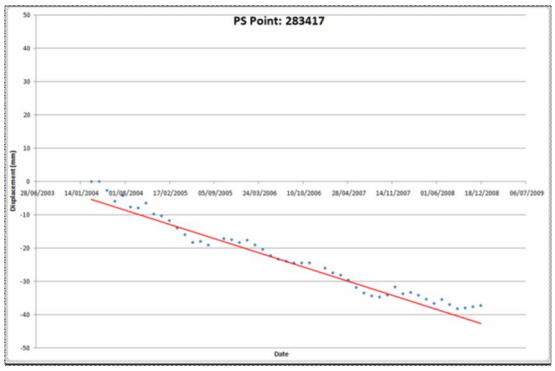

6.4.4 Interpretation

PSI is a complex dataset and users should consider the following information in any subsequent interpretations of the provided data:

- The motion recorded for an individual or collection of PS point may be an expression of the motion of the ground, the motion of a feature on the ground or a combination of the two. The source of motion at a measurement point may be attributed to a variety of factors.
- Users may wish to consider autonomous movements and also stability that is spatially and/or temporally correlated.

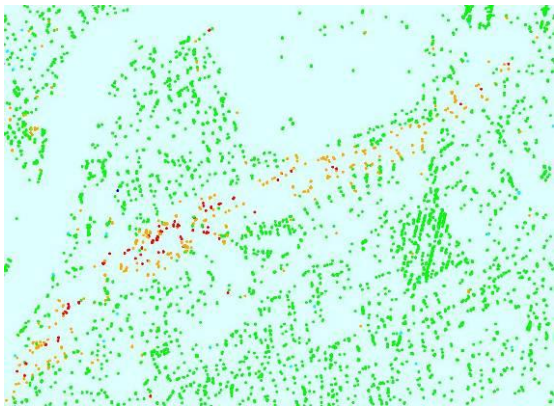

An example of a linear cluster of PS points all indicating similar movement.

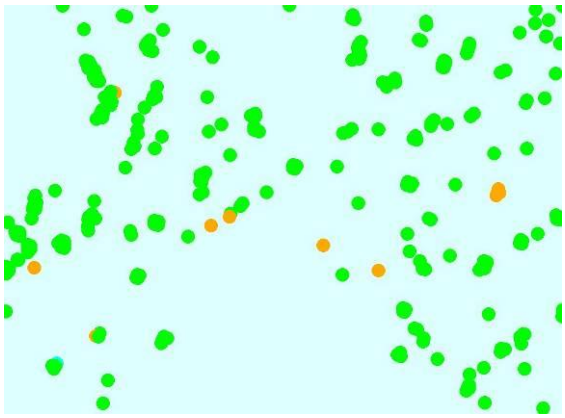

An example of isolated PS points showing different movement compared to the surrounding PS points.

- If PS exhibit instability, this does not mean that features across the AOI are at risk. If PS points are not moving away or towards the satellite, this does not mean their motion situation will remain such.
- Analysis of time series may reveal episodic changes and or changes in acceleration of motion rates. It is worth noting that time series may contain residual errors (such as uncompensated atmosphere) and are less precise than the average annual motion rate.
- PSI motion information should be analysed and interpreted alongside other complimentary datasets.
- Estimates of PS height may be useful in determining the potential position of PS across targets e.g. base or top of building.
- The spatially interpolated raster may help to reveal broad domains of instability.

APPENDIX 7 : REVIEW OF APPROACHES FOR SMC RETRIEVAL FROM SATELLITE DATA

The use of satellite SAR for Soil Moisture Content (SMC) in the Netherlands has been discussed previously by Smulders *et al.,* (2010) where ENVISAT ASAR 'Wide Swath' was used to look at change detection associated with soil moisture. This study provides an understanding of some of the mechanisms associated with the SAR radar signal and SMC, however given the low spatial resolution of the data available and with limited supporting data clear conclusions could not be reached.

7.1 AMPLITUDE CHANGES

The penetration depth of the radar signal varies with a number of parameters, primarily wavelength and dielectric properties; the latter in turn depending upon factors such as, moisture content and soil type. It is commonly understood that longer wavelengths have the ability to penetrate further into the soil than shorter wavelengths under normal conditions partially owing to the decrease in relative surface roughness parameter with longer wavelengths (Baghdadi *et al.,* 2008). This concept was verified during a study in Nevada using SIR-B (Space shuttle imaging radar) to monitor the attenuation of the radar signal as a function of soil moisture. Here it was found that measured attenuations were closely matched to theoretical concepts of penetration depth and the effects of soil moisture as illustrated in Figure 1. It was also found that L band had the capability to penetrate up to 85cm beneath the surface in some soils which were very dry. However, whilst there have been a number of studies considering the effect of penetration depth on soil moisture none have indicated the potential of this depth as a useful signal (Nolan and Fatland, 2003).

Figure 1a shows the sensitivity of penetration depth to different levels of water content. Increases in soil moisture reduce the attenuation substantially when moisture levels are low, but when moisture levels are very high (approaching 40%) penetration becomes minimal. Further increase in moisture is predicted to have a negligible effect on penetration depth. Following a significant rainfall event, modelled SAR signal penetration is predicted to be dramatically reduced in both C and X bands for several days after the event whereas for L band, after 2 dry days the signal might be expected to penetrate to around 8mm and after 5 dry days to around 30mm (figure 1b) (Nolan and Fatland, 2003).

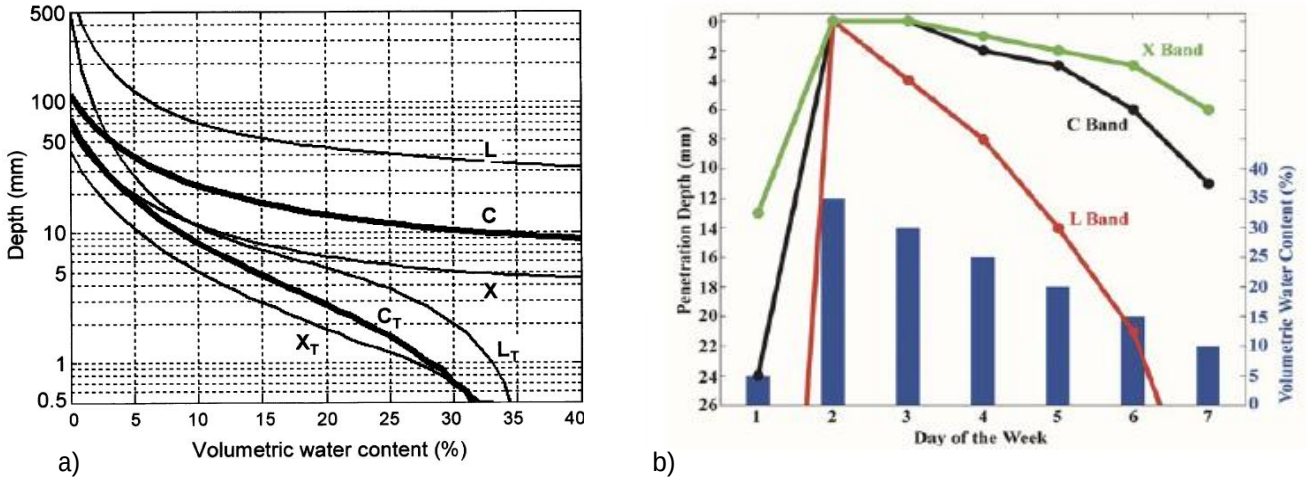

Figure 1: a) Penetration depth of SAR microwaves as a function of soil moisture for L C and X bands. "T" indicates penetration depths when transmission losses at 0.1mm increments have been assumed, the other curves indicated attenuation losses only.
b) Changing penetration with time using modelled rain and evaporation across 3 frequencies, assuming the depth profile of moisture levels is uniform. After Nolan and Fatland, (2003).

That is not to say that shorter wavelengths on their own are not useful for soil moisture studies. There have been several applications of C band (owing to the considerable archive) and X band data for mapping SMC such as Baghdadi *et al.,* (2008), Ticconi *et al.,* (2010), Nolan *et al.,* (2003) and Wang *et al.,* (2004) to name but a few. However, the application of amplitude data at shorter wavelengths is limited where volume scattering from vegetation reduces the signal returning to the satellite having reached the ground, hence application of short wavelength signal amplitude to soil moisture is limited predominantly to arable land with no or sparse crop cover and over periods when surface roughness can be considered stable. With longer wavelengths as the penetration is improved (Figure 1), the data can be used to a greater degree in areas with some vegetation, with low height and density (biomass) (Baghdadi *et al.,* 2008). A potential advantage of data from the more recent X band SAR sensors, despite their seeming limitations for soil moisture mapping, is their increased spatial resolution and temporal revisit. These factors can enable monitoring of field parcels in greater detail monitoring potentially every day or few days leading to the ability to identify perturbations in backscatter trends that may correlate regionally or locally and fluctuating at rates that could be accounted for by SMC change rather than other surface changes (Figure 2).

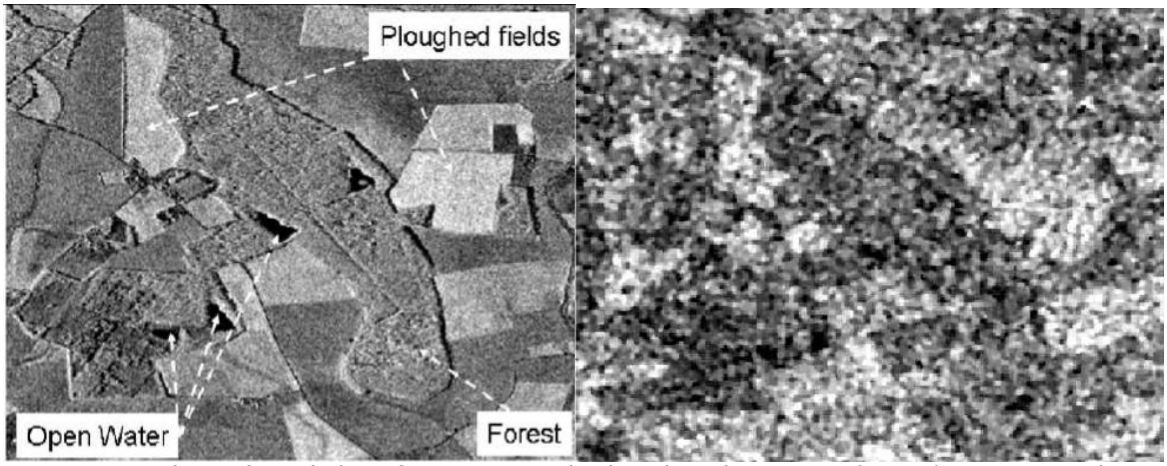

Figure 2: comparison of resolution of TerraSAR-X (1m) and Envisat ASAR (12.5m) over Orgeval, France (Adapted from Baghdadi et al., 2008)

In addition, the variation of incidence angle is also of importance because it plays a role in defining the roughness of the soil. At higher incidence angles (e.g. >45^{o}) it has been found that the effect of surface roughness is increased. In contrast, for soil moisture estimation it is suggested that lower incidence angles (25^{o}-35^{o} off nadir) are preferred because at these angles the sensitivity to surface roughness is reduced thereby improving the capability to extract soil moisture parameters (Ulaby, 1974). This is because soil moisture goes some way to smooth the surface. At low incidence angles the radar signal is higher for smoother surfaces because specular reflection dominates the signal, whereas as you move towards higher incidence angles the signal decreases as diffuse reflection dominates, highlighting the use of higher incidence angles for surface roughness estimations instead of soil moisture (Baghdadi *et al.,* 2002 and 2007). Baghdadi *et al.,* (2006) noted that with a combination of SAR data acquired at both low and high incidence angles, surface roughness can be eliminated and the accuracy of the soil moisture estimations improves (Figure 3). These correlations are possible when surface roughness remains constant which in an operational sense is unlikely to be the case.

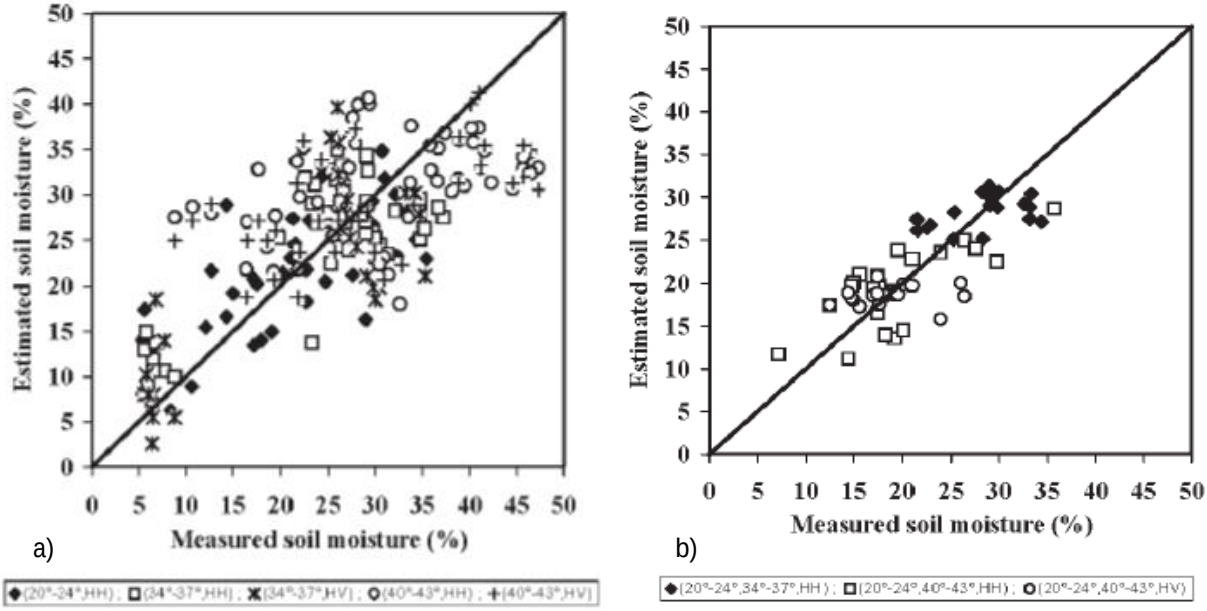

Figure 3: Comparison between the estimated moisture volumetric (mv) values and those measured in situ. a) one polarization one incidence angle, b) one polarization 2 incidence angles (Adapted from Baghdadi et al., 2006).

Baghdadi *et al.,* (2008) develops this analysis further when assessing the capabilities of TerraSAR-X in comparison with ALOS and Envisat. As part of their analysis they combined incidence angles into a color composite. In doing so, they concluded the composite reveals features distinct at different angles (both low and high). Figure 4 shows the varying soil moisture content over the bare fields, where a difference in volumetric water content between areas can be seen clearly by the noticeably darker zones. These darker zones correspond not only with the drainage but also with soil heterogeneities within field parcels. In part the differences might be accounted for by small differences in soil composite, slope or drainage network and it is suggested that more investigation will be needed to improve the understanding of these heterogeneities.

The use of amplitude data for soil moisture is not clearly proven and there are several ambiguities, not least because of the variability of response, for example Martin *et al.,* (1989) found that in prairie environments there was a strong correlation with soil moisture at both low and high incidence angles. In addition, whilst there is a small correlation between soil moisture and incidence angles the change is detected empirically and a number of factors are not considered comprehensively, such as variability of soil roughness, surface vegetation, etc.

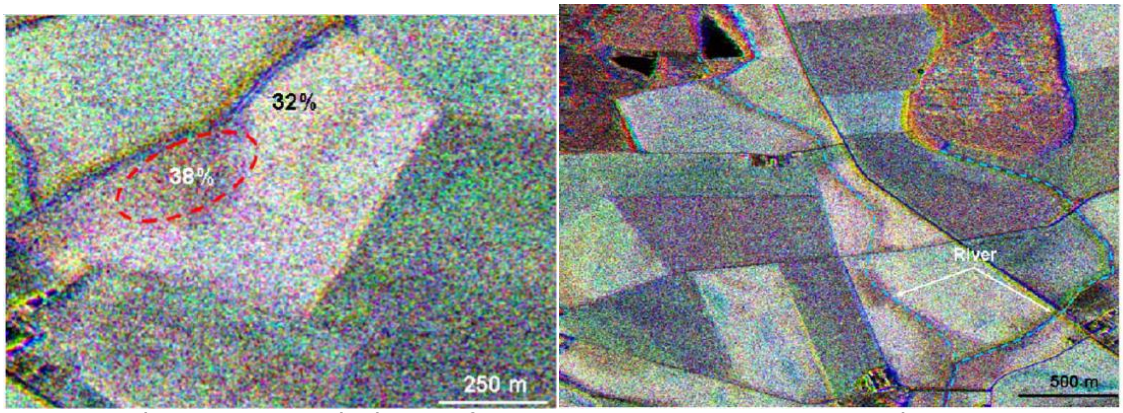

Figure 4: Composite images from TerrSAR-X sensor over Orgeval, France
RGB HH 50^{o} incidence (12th Feb), HH 26^{o} (12th Feb), HH 26^{o} (15th Feb) (Baghdadi et al., 2008).

7.2 MULTIPOLARIZATION

It has become clear, that the separation of the surface roughness and soil moisture parameters is key to soil moisture estimation, however, this is not possible with a single frequency and single polarisation as there no option to separate these values. In contrast, fully polarimetric data provides an option to separate surface roughness and soil moisture induced effects from the different polarizations of the sent and received signals (Hajnsek *et al.,* 2003). Since the launch of Radarsat-2, major improvements to polarisation capabilities of SAR sensors has led to extensive research into the use of polarimetry for SMC studies. Conclusions of such studies have been variable but for the most part have suggested the accuracy of SMC retrieval is not significantly improved when using simple comparisons of multiple polarisation amplitudes. This is particularly the case when dual polarization data is used which is available from several satellites in their standard modes. For example, Baghdadi *et al.,* (2006) found that the use of two ASAR polarizations (HH and HV) did not significantly improve the soil moisture estimation and concluded that the use of a single polarization and varying incidence angles provided more accurate results. Skriver, (2008) identified that multi temporal data was much more efficient for improving the accuracy of soil moisture estimates than using dual polarimetric amplitude data alone.

In contrast, techniques and algorithms have been developed to better explain and understand the scattering processes occurring above, below and at the ground surface using fully polarimetric or 'quad-pol' (HH, HV, VH, VV) SAR data. With a more comprehensive model of scattering processes the ability to determine soil moisture from the effect on dielectric properties is significantly improved.

A number of methods have been proposed, such as semi empirical algorithms; Oh *et al.,* (1992) and Dubois *et al.,* (1995) which are based largely on the evaluation of amplitude ratios and also the more advanced models based on the Bragg and Physical Optics (PO) scattering models; X-Bragg (Hajnsek *et al.,* 2003) or X-PO (Martone *et al.,* 2009), which have been extended (accounting for the 'X' prefix) to account for wider ranges of roughness conditions, non zero cross polarization backscattering and depolarization and are based on eigenbased decomposition (Martone *et al.,* 2009, Hajnsek *et al.,* 2003).

Semi empirical methods (Oh *et al.,* 1992 and Dubois *et al.,* 1995) serve to provide a reasonable estimate of soil moisture however, they do not consider the full range of roughness scales or the multiple scattering effects so their validity is limited (Keydel, 2005). In contrast, eigen based methods improve the inversion models by ensuring their applicability to a much larger class of land cover than the semi empirical models will allow (Keydel, 2005), therefore providing a more quantitative approach to SMC.

Whilst eigen-based decomposition for soil moisture estimation is still in its infancy the understanding of scattering entropy *(H);* an indicator of randomness, alpha angle *(α)*; the type of scattering, and also anisotropy *(A)*; a measure of the difference of the secondary scattering mechanism, is thought to be key to soil moisture estimation (Hajnsek *et al.,* 2003, Rao *et al.,* Ticconi *et al.,* 2010, Lee *et al.,* 2004).

Ticconi *et al.,* (2010) used *H* and *α* of X-band TerraSAR-X 'quad-pol' data to assess its capabilities for soil moisture estimation using the X-PO model. The X-PO model defined by Martone *et al.,* (2009) was designed to bridge the gap between studies using lower frequency and higher frequency polarimetric data to assess the accuracy and conditions for extracting SMC from this higher frequency data. The study by Ticconi *et al.,* (2010) confirmed prior knowledge that for shorter wavelengths the surface roughness overall is nominally high due to volume scattering from simultaneous scattering mechanisms. In addition, they also found that even over bare agricultural fields the entropy was still reasonably high (Figure 5a). Figure 5b shows the dominant *α*, this is especially prominent in bare or sparsely vegetated fields (shown in red) those areas in green show a lower *α* suggestive of dipole like scattering over fields which have a compact and distinct vegetation layer, because of this, the field parcels exhibiting these characteristics were masked from further analysis (Ticconi *et al.,* 2010).

Once the *H* and *α* values have been calculated the dielectric constant (permittivity of the soil) can be extracted and subsequently converted to volumetric water content by inverting the X-PO model (Figure 5c). However, Ticconi *et al.,* (2010) concluded that despite the collection of field measurements, without surface roughness data, there appeared to be a distinct underestimation of soil moisture levels from the SAR data. They concluded that further investigations were required and their conclusions confirmed the earlier findings by Martone *et al.,* (2009).

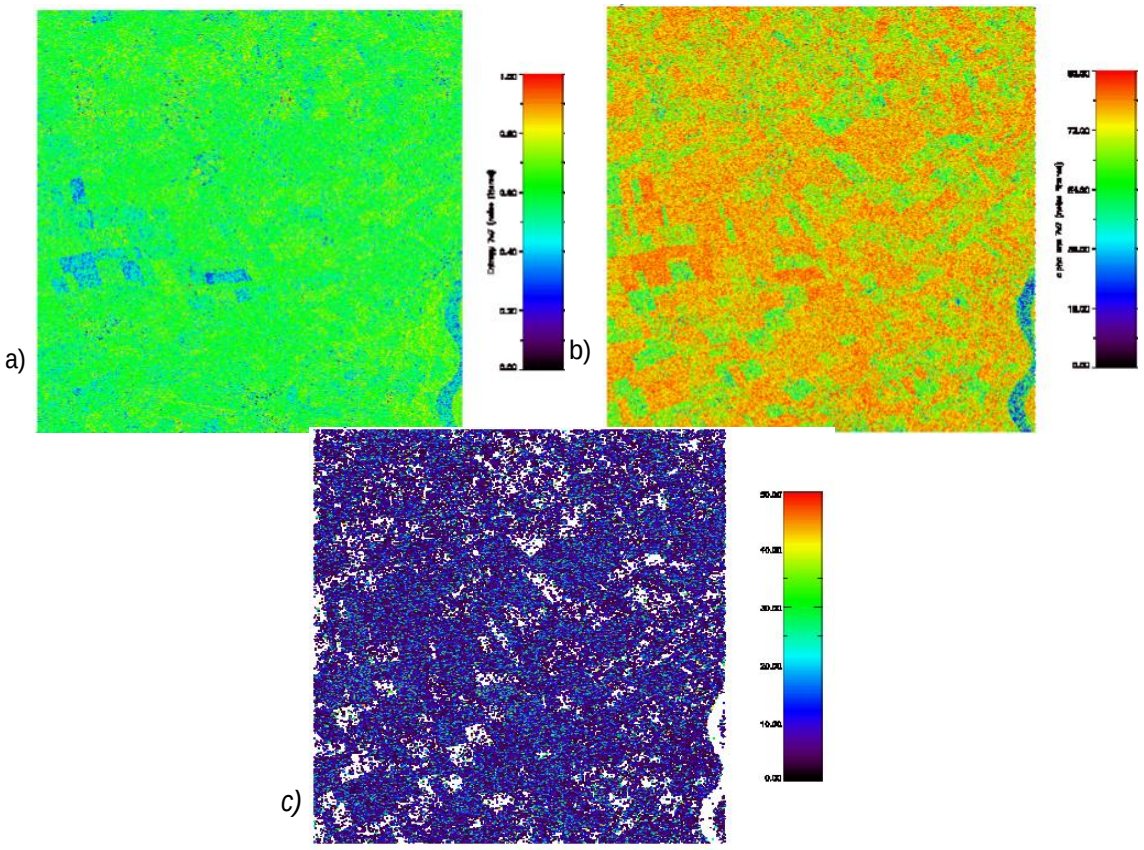

Figure 5: a) Entropy H Blue-Green-Red (low to high) b) dominant alpha angle Blue-Green-Red (low to high) c) soil moisture in volumetric percentage of the region derived from fully polarimetric SAR. (Adapted from Ticconi et al., 2010)

Hajnsek *et al.,* (2003) developed the X-Bragg model using *H, α* and *A*. The inclusion of *A* provides complementary information to the entropy and facilitates interpretation of the surface scatterer, in particular because *A* remains constant with changing permittivity and local incidence angle and therefore provides a basis for decoupling roughness and moisture effects. By modelling both the permittivity and the local incidence angles in the coherency matrix the variation of both the topography and the local incidence angle can be accounted for. As such, this technique is proposed to be a suitable methodology for both flat and topographically variable terrain.

In their study Hajnsek *et al.,* (2003) used L band fully polarimetric airborne data over test sites in Germany. Prior to analysis, as in the Ticconi *et al.,* (2010) study, those pixels above a certain threshold were removed from analysis. In this case those with $H > 0.5$ and $\alpha > 45^{o}$ were masked out leaving only the dominant surface scatterers and avoiding dipole and double bounce scatterings. The results, shown in Figure 6, compared with laboratory data have shown that the inversion is of high enough accuracy to show seasonal variations.

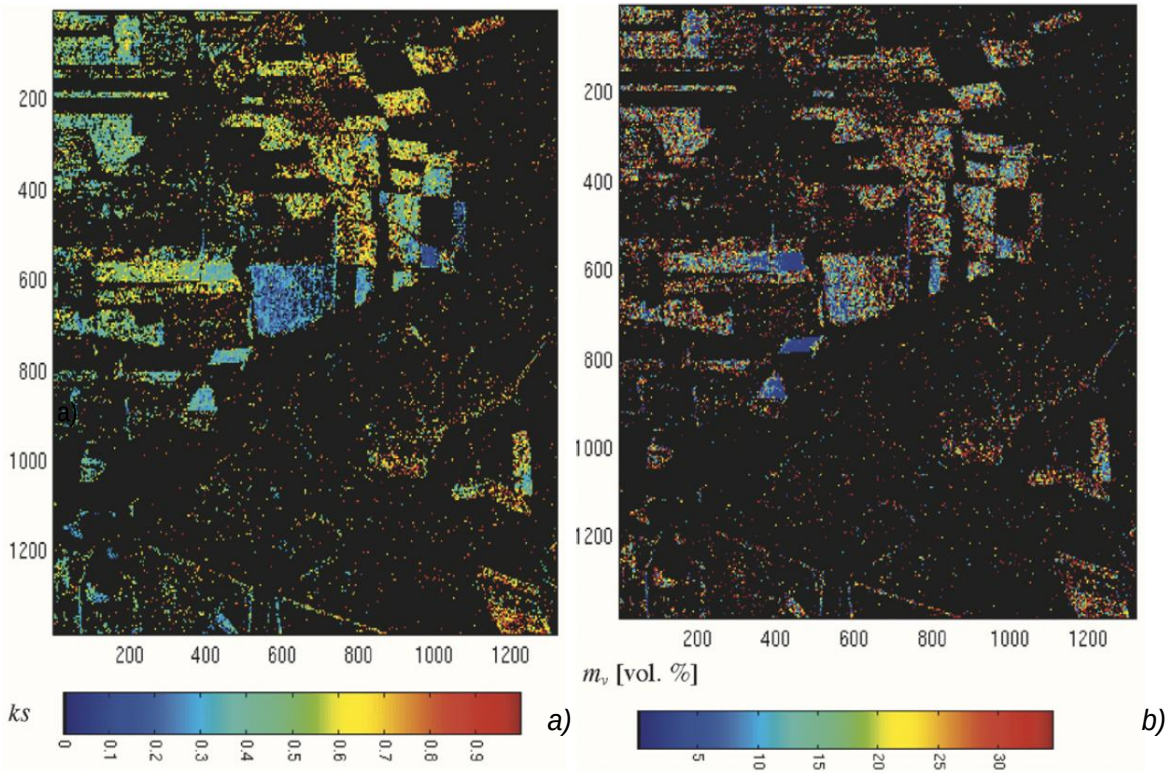

Figure 6 Elbe-Auen test site: a) estimated surface roughness (ks), ranging form 0 – 1 non valid areas are indicated as black b) estimated volumetric soil moisture (mv), ranging from 0-40%. Adapted from Hajnsek et al. 2003.

Both the X-PO and Bragg models do appear to exhibit some form of either under or over estimation affecting soil moisture (in the case of Ticconi *et al.,* 2010) or surface roughness (Hajnsek *et al.,* 2003). Hajnsek *et al.,* (2003) noted an overestimation in surface roughness and in part this is due to noise, whilst noise filters can, and were in this case, applied to the data, the filters used must retain the polarimetric content because even small changes in correlation can lead to biasing owing to changes to the scattering mechanisms, therefore impacting the co-polarization ratio.

There are now a number of different techniques that have been and are being developed using polarimetric methods and there is clearly promise for future application with respect to SMC. The main limitation is still the presence of vegetation (Hajnsek *et al.,* 2003). Therefore, even with polarimetric methods the presence of vegetation would still be a key issue for most natural environments. However, as was noted by Hajnsek *et al.,* (2003), with increasing advancements in SAR technology there is great promise for further work in this domain, not just using single frequency multi polarization data but dual frequency multipolarization data which would make it possible to apply the technique to a wider range of surface conditions. However, this in turn raises more issues with regards to how the different frequencies interact with the surface, which would need to be considered further.

7.3 DIFFERENTIAL INTERFEROMETRY

The potential for utilizing Differential Interferometry (DifSAR) to determine soil moisture arises from a phenomenon frequently overlooked where the effect has either been dismissed as noise or incorrectly attributed to causes which often may only sometimes correlate with soil moisture.

Gabriel et al (1989) observed SAR signal path length changes of several centimeters in interferograms from L-band Seasat data corresponding to irrigated agricultural fields. The effect was attributed, without thorough testing, solely to swelling of clay rich soils (Figure 7).

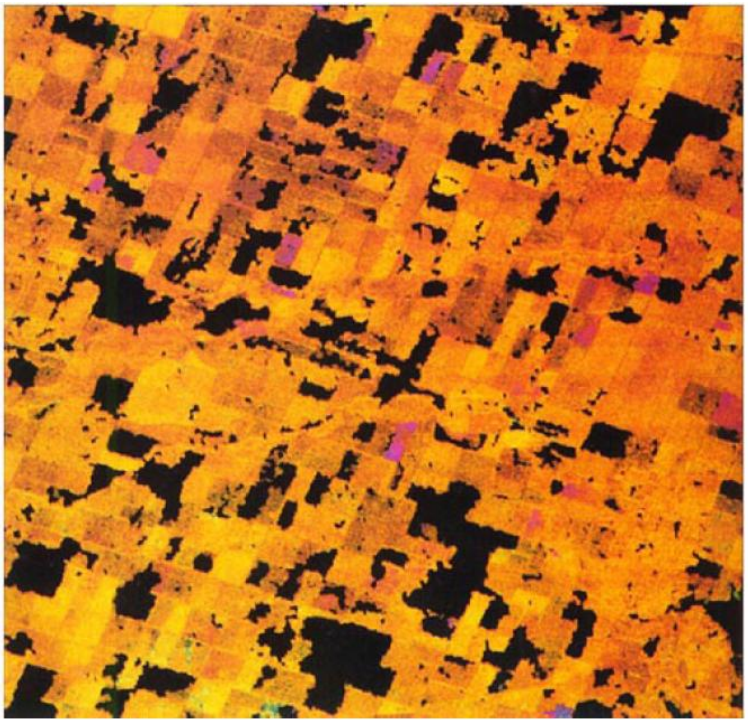

Figure 7: Dominant yellow color represents zero phase change black areas are loss of phase coherence (due to ploughing between acquisitions). Blue to red to green indicate small motions (2-3cm) of the fields from swelling or shrinkage associated with watering (Gabriel et al 1989).

However, Nolan *et al.,* (2003) hypothesize that such changes in path length in fact result from change in penetration depth which can serve as a viable proxy for soil moisture in a range of soil types. They provide evidence that soil moisture can be derived from the related phase signal of C-band DifSAR and discounted clay swelling as a mechanism in most of their study area.

In their test site above ground biomass levels are low, in the region of 0.25 kg/m^2. However, previous studies, such as Ulaby *et al.,* (1996), indicate that biomass under 0.5 kg/m^2 would have a negligible effect on C-band backscatter.

Nolan *et al.,* (2003) utilised a DEM from Intermap's Star3i airborne X-band InSAR system having typically 2m vertical accuracy. However, similar temporal results were also obtained when using alternative SRTM and NED DEM data, helping to confirm that the phase change features detected that correlated with hydrological features, as would be anticipated from the drainage process, and were not due to errors in the topographic models. Whilst the relationship between phase change and soil moisture is non linear, meaning absolute measurement requires a priori knowledge of moisture, the availability of accurate DEMs enables sub-millimeter phase changes to be resolved which relate to sub-percentage soil moisture resolution at most initial moisture levels.

In addition to topographic residuals, Nolan *et al.,* (2003) proceed to discount phenomena including atmospheric/ionospheric anomalies, vegetative growth, interaction with wind, surface roughness, frost and dew as accounting for the phase change features they observed. The study failed to achieve full verification largely because the soil moisture sensors used were placed at a minimum of 50mm depth, whereas C-band probably penetrates up to 20mm and in their test site there was a presence of windblown dust on the surface which was normally very dry, but tended to retain water at the surface after short rain events.

The phase change has a non-linear relationship to penetration depth and penetration depth is non-linearly related to soil moisture. Hence a measurement of the change in phase from a single interferogram cannot be converted directly to a change in soil moisture unless one of the soil moisture values is known *a priori* or if some linearizing assumptions can be made.

APPENDIX 8 : DESCRIPTION OF MONITORING TECHNIQUES

Synthetic Aperture Radar (SAR)

What is it?
Synthetic Aperture Radar (SAR) is a technique that is widely used in satellite imagery. It is capable of measuring a variety of geophysical properties. For the objective of dike monitoring, soil moisture or saturation is the property that is focused upon.

How does it work?
SAR satellites send and receive radar waves in a certain frequency (e.g. 5 GHz, also named C-band). A side looking antenna looks at the 'scatterers' or 'backscatters' of the radar signal as shown in the figure below. Flat surfaces like water will reflect and will not return to the antenna, while rough surfaces will cause a backscatter to the antenna, depending on the properties and geometrical characteristic of the terrain. The frequency of coverage, i.e. the time between two exactly the same images, depends on the orbit of the satellite. When looking at cropland, the amount of backscatter depends on the type and growth stage of vegetation and on the amount of saturation of the subsurface. Different types of SAR sensors exist on different satellites, each having its own characteristics (frequency, polarization, coverage, repeating cycle, spatial resolution).

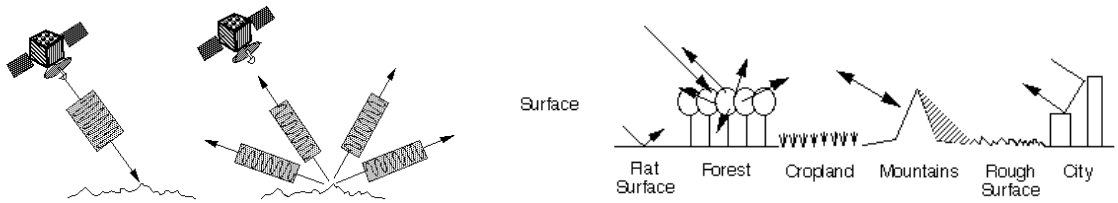

Figure 1 **Left: Backscattering of a radar signal on a rough surface. Right: different surfaces cause different backscattering characteristics. Courtesy of ESA.**

Long term and short term
SAR data can be used for long term and short term. For long term, differences in electromagnetical properties can be linked to differences in saturation. If at high waters a certain area will show more saturation than others, this could be an area where piping could occur more likely, or an area that is more likely to be flooded, etc. The area should thus be pointed out for further research for the responsible dike maintainer (e.g. water board or national maintainer). For short term, an anomalous increase in saturation could point out a current area in the dike where piping is occurring, or were groundwater is rising due to another mechanism.

Advantages
Because of working with satellite data, no physical data acquisition has to be executed. The data is in most cases delivered in a standardized way, and archived by the satellite agency (e.g. European Space Agency).

Disadvantages
The SAR data used in most studies is only penetrating the subsoil for a few centimeters (C-band). Vegetation and vegetation growth creates much noise, causing a very low signal-to-noise ratio. It is highly recommended to work with HH polarization data, which is less sensitive to vegetation. More information on polarizations can be found on http://envisat.esa.int/handbooks/asar/CNTR1-1-5.htm.

The costs for high resolution data (meaning having a spatial resolution smaller than 20x20) are in many cases high (e.g. < EUR 1000 per image). However, the new Sentinel-1 expected in 2012 (HH polarized and 20 x 20 m spatial resolution and app 6 day repeating cycle or better) will be for free.

Conclusions
SAR is a technique already widely used for scientific purposes. It is possible to derive saturation patterns from SAR data. Until now, there is no freely available data with a resolution of 20 m or smaller having a good repeating cycle to be used for operational purposed and thus we can only experiment with data until the Sentinel-1 satellite will be launched in 2012.

Reference
European Space Agency, 2007, Envisat ASAR product handbook, issue 2.2. courtesy of ESA. Also to be downloaded at http://envisat.esa.int/handbooks/asar/toc.htm

Persistent Scatter Interferometric Synthetic Aperture Radar (PS-InSAR)

What is it?
Persistent Scatterer Interferometry (PSI) is an advanced differential interferometric technique which involves the processing large volumes of multi-temporal Synthetic Aperture Radar (SAR) data to identify networks of persistently reflecting surface features (e.g. buildings, bridges, infrastructure and rocky outcrops), against which precise (millimetric) measurements of motion can be made.

How does it work?
As said in the description of SAR (above), smooth surfaces like water will reflect and will not return to the antenna, while rough surfaces will scatter back to the antenna, depending on the properties and geometrical characteristics of the terrain. We speak of ‘persistent scaterrers’ as objects that will give a high backscatter and not change in scattering characteristics. This is in most cases a human made reflector as a roof, a soundscreen at the highway or a bridge. Also, for typical circumstances dikes can be considered as persistent scatterers. PS-InSAR looks at the phase difference of the radar signal per persistent scatterer. In this way, millimetric vertical movement can be measured per repeating measurement.

Long term and short term
PS-InSAR measurements can be used for assessment of historical long term deformation studies. In dike assessment, this will for instance be a part of the dike showing more subsidence, thus making it a part for extra inspection by the levee patroller. The historical data can also be used for a priori input in dike models.

Advantages
The method can be used with existing equipment, making the data acquisition cheap. The data is provided, checked and archived by the European Space Agency and can be used for free by everyone.

Disadvantages
The data processing is complex and not always consistent. Most problems will occur due to atmospherically differences between measurements and when the difference in deformation is too large (larger than half a radar wavelength) between to measurements.

Conclusions
PS-InSAR is a very promising technique. It has however yet to be established as a standard technique and validation of the techniques will probably take another few years.

References
Hanssen, R.F., Radar Interferometry: Data Interpretation and Error Analysis. Kluwer Academic Publishers, Dordrecht, 2001. 328 pp
Kampes, Bert M., Radar Interferometry: Persistent Scatterer Technique, Springer, Berlin, 2005, 211 pp
Ketelaar, V.B.H., Satellite Radar Interferometry: Subsidence Monitoring Techniques, Springer, Berlin, 2008, 280 pp
ESA website: http://envisat.esa.int/handbooks/asar/CNTR1.htm#eph.asar.ug
Hansje Brinker website: http://www.hansjebrinker.com
Fugro-NPA website: http://www.fugro-npa.com/services/insar-surveying/insar-techniques/persistant-scatterer-insar

Passive Microwave Radiometry (PMR)

What is it?
Passive Microwave Radiometry is a passive method that measures the emission of microwaves by the (sub)surface. Materials emit microwaves, so does soil. The land surface radiation of microwaves is primarily dependent on the free water content of the soil (Haarbrink and Shutko, unknown date).
This method was also developed for quick emergency response in the case of terrorist attack or a natural disaster (Haarbrink and Shutko, 2005).

How does it work?
PMR can be applied as an airborne technique to measure soil moisture. Also space applications are possible.

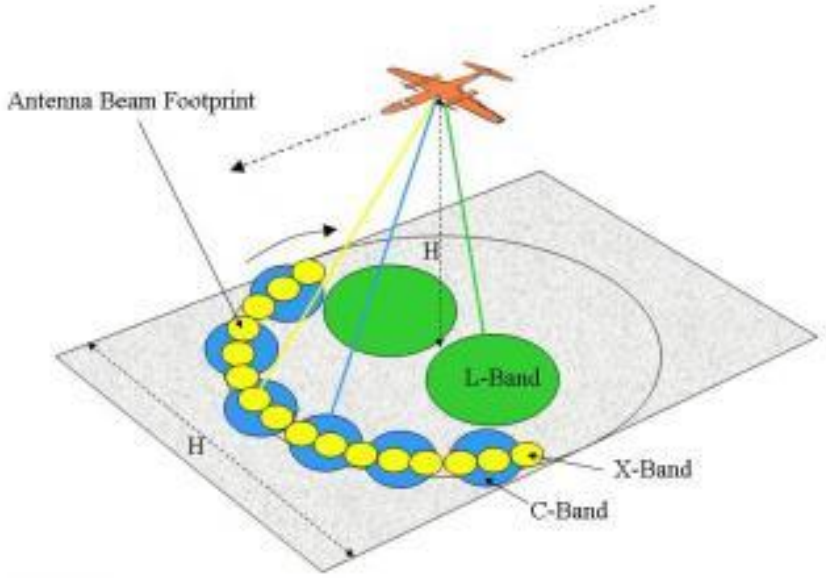

Figure 2 Airplane measuring three microwave bands for soil water content approximation. (www.miramap.com)

Long term and short term
Airborne PMR from planes, helicopters or Unmanned Airborne Vehicles (UAV's) could monitor soil moisture in short periods (UAV's, helicopters and planes) as well as long periods (satellites).

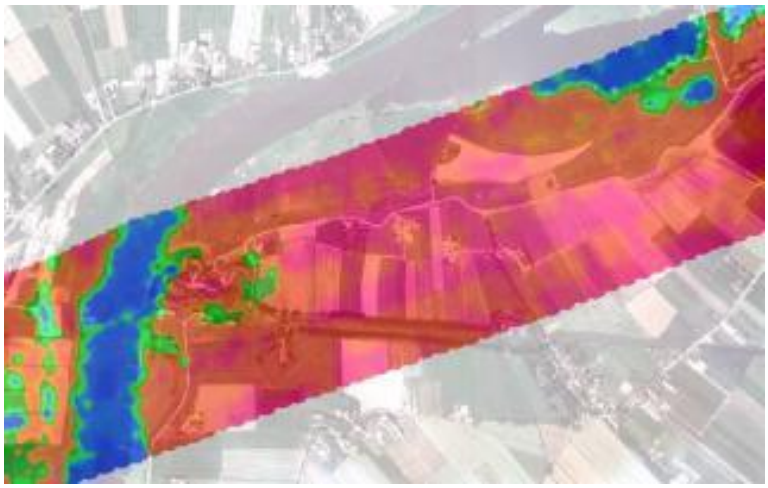

Figure 3 Resulting image from PMR measurements. Blue is wet and red is dry. (www.miramap.com)

Advantages
Soil moisture gives a good indication where internal water pressures are high. A method that can image large areas, such as automated UAV's or satellites, is relatively cheap but especially very quick to gather data about

the internal water contents. Miramap shows a draught monitoring application of this method, which measures the subsurface soil water contents.

Disadvantages
This method is not widely used yet as a monitoring system and produces large amounts of data, although there was a PMR sensor installed on the International Space Station (ISS).

Conclusions
PMR seems a promising method to monitor soil water contents on a large scale in short and long term, due to its applicability to (unmanned) airborne and space vehicles.

References
Haarbrink, R.B. and Shutko, A.M. (unknown date) New airborne sensor for soil moisture mapping, *(publication by ESA, Miramap and Inter-Commission WG I/V, Autonomous Navigation)*.
Haarbrink, R.B. and Shutko, A.M. (2005) Airborne passive microwave radiometry for emergency response, in *Proc. 1st Int. Symp. Geo-Inform. Disas. Manag.*, Delft, The Netherlands.
www.miramap.com (Miramap is a Dutch firm specialized in remote earth observation, initialized by the European Space Agency (ESA))

High resolution remote (infrared) image monitoring

What is it?
Recognize areas where surface seepage occurs, using pattern recognition in visible or infrared images, which are taken from an airborne vehicle.

How does it work?
A small plane, helicopter or unmanned airborne vehicle (UAV), equipped with high resolution (infrared) cameras and GPS flies over the levees that need to be monitored or are suspected of weaknesses. The cameras image the surface using either visible light or infrared cameras. Using pattern recognition, regions of surface seepage and sand mounds can be recognized. In infrared images the temperature difference between the surrounding waters and the seepage water can be imaged, also showing the weaker areas of the levee, where increased seepage and possibly piping occurs.
When images from different surveys are compared, one can recognize changes in the area close to the levee and possibly identify piping.

How is this applicable to embankment monitoring?
Monitor internal seepage and possibly piping using a combination of high resolution cameras and pattern recognition.

Long term and short term
This method is ideal for short term monitoring of suspected weaker areas. Long term monitoring would be too expensive. In the future, if more satellites with higher resolution cameras are available, long term monitoring from those satellites would be possible.

Advantages
If the pattern recognition software would work properly and the locations of seepage are not overgrown with vegetation this method should give a good overview of weaker areas of monitored levees, very quickly. Infrared monitoring images the infrared spectrum and possibly has less interference by vegetation, due to the fact that it measures the local heat radiation, not the visible color.

Disadvantages
One of the challenges for subsequent monitoring is to have a stable enough platform (plane or helicopter) to image at the right locations. Other problems might be: animal and human activity and changes in vegetation (due to wind or vegetation growth for instance), but the pattern recognition algorithms might be able to filter those.

Conclusions
Presently, as a short term monitoring technique, this seems to be a promising method. Increased satellite density and increased satellite camera resolution might make long term monitoring using this method possible in the future.

GPS deformation monitoring

What is it?
High sensitivity GPS receivers placed on top of the levee can monitor external deformation by measuring the absolute location and compare this value to previous values.

How does it work?
Lovse et al. (1995) used a differential Global Positioning System (GPS) receiver to monitor movement of the Calgary Tower in Calgary, Canada. They were able to measure movements with a 5 mm accuracy. In a similar way this method could be applied to embankment monitoring: monitor the slightest deformation in an embankment and try to recognize decreased strength. An application somewhat similar to levees is the application to earthquake fault observation in California. The accuracy of GPS measurements and spectral sensistivity has been steadily improved (see e.g. Bock et al. (2004) for an overview of some of these improvements). Application of GPS to levee monitoring requires millimeter level accuracy. Currently, using GPS to determine horizontal and vertical positions to within 1-2 mm for continuous, long-term application approaches the limits of this technique. Such accuracy requires meticulous handling of error sources and the use of high grade GPS equipment. Typically, the dual frequency, geodetic grade GPS receivers that are used exceed US$ 12,000 per unit. This cost is prohibitive of large-scale monitoring applications. In a joint US-Dutch research initiative, the aim is to arrive at a validated method with a unit price in the order of a more affordable US$ 1000. This research is to be carried out within the next two to three years.

How is this applicable to embankment monitoring?
Wilkins et al. (2003) wrote a paper about a fully automated remote monitoring system for earth filled dams. Differential GPS receivers placed on strategic localities on the levee record information about their absolute positions. Comparing these positions over time with previous measurements, one could monitor movement of the levee with 1-2 mm precision.

Long term and short term
The technique is applicable both for long and short term application.

Advantages
Deformation can be monitored with a 1-2 mm precision with existing technology. Installation needs no, or very little, penetration of the levee's body, sustaining its integral strength.

Disadvantages
This is a discrete measuring technique. To monitor an embankment, many GPS receivers have to be installed on the embankment's surface. Furthermore, in the case of piping for instance, deformation is not a clear indicator for occurrence of piping until failure occurs. GPS monitoring will therefore not give any predictability of failure due to piping.

Conclusions
GPS monitoring as described above might be useful to monitor stretches of embankments where failure due to e.g. slope instability is suspected. Piping can hardly be monitored with the external deformation parameter.

References
Bock, Y.; Prawirodirdjo, L., Timothy, I. and Melbourne, T.I. (2004) Detection of arbitrarily large dynamic ground motions with a dense high-rate GPS network. *Geophysical Research Letters,* **31**, L06604.
Lovse, J. W.; Teskey, W. F.; Lachapelle, G. and Cannon, M. E. (1995) Dynamic Deformation Monitoring of Tall Structure Using GPS Technology. *Journal of Surveying Engineering*, **121**, 1, 35-40.
Meng, X., G.W. Roberts, A.H. Dodson, E. Cosser, and C. Noakes (2002) Simulation of the Effects of Introducing Pseudolite Data into Bridge Deflection Monitoring Data. *Proceedings of 2nd Symposium on Geodesy for Geotechnical and Structural Engineering*, 21-24 May 2002, Berlin, 372-381.
Wilkins, R.; Bastin, G. and Chrzanowski, A. (2003) ALERT: A fully automated displacement monitoring system. *CAMI 2003 Conference*, September 8-10 2003, Calgary, Canada.

Ground Penetrating Radar (GPR)

What is it?
Ground Penetrating Radar (or GPR) is an electromagnetic technique often used to search for buried foundations, storage facilities and other buried either manmade or natural features. This method is also used for layer thickness surveys, such as asphalt, thickness and water table investigations.

How does it work?
GPR uses a high frequency (80 to 1500 MHz) electromagnetic pulse transmitted from a radar antenna to probe the earth (USDOT website). Subsequently, a radar receiver detects this signal that was reflected by interfaces that posses a contrast in dielectric properties. Many mechanical and geological properties correlate with the dielectric properties of the medium.
GPR does not directly measure the dielectric properties of the subsurface, but detects dielectric anomalies, caused by changes in geometry of subsurface interfaces. It is commonly used to determine the groundwater surface, locating metallic pipes or storage tanks or measure asphalt thickness, but can also measure localities with an increased hydraulic conductivity.

How is this applicable to embankment monitoring?
In Sweden for instance, several examples of water retaining dams have been surveyed using cross-hole tomography and reflection measurements (both applications of the GPR technique). Carlsten et al. (1995) performed a survey on the Suorva embankment (a water retaining dam with an internal core). They applied GPR in two different flavors: surface reflection measurements and cross-borehole tomography. The latter has more potential as a permanent embankment dam monitoring system, since the GPR antennas do not have to be moved over the surface.
GPR can also be inserted into the levee to monitor piping from below. This is costly, but it is possible to image the individual pipes very nicely.

Long term and short term
GPR antennas can be dragged over the levee's surface, making this a very mobile technique. Because there is much experience with the data processing, it can be done quickly. GPR can also be applied as a permanent monitoring system.

Advantages
A GPR antenna can act both as a receiver and as a transmitter, making the system more versatile: for instance, if there are ten antennas in a dam and subsequently each antenna acts as a transmitter and the other nine as receivers, a dataset of tomograms of ten section s of the dam can be made within minutes. It is not clear what the minimum spacing should be in order to monitor an embankment for piping. Since GPR is an active method, signal-to-noise ratios are expected to be relatively good.
A more important advantage is the way imaging can be done: with a moving survey, one can nearly real-time image what lies beneath. With fixed antenna layouts, small variation are visible.

Disadvantages
For permanent monitoring, insertion of the GPR antennas into the dike, the internal structure is disrupted by the penetration or drilling. Penetration of radar waves into clay is poor, making imaging beneath and in the clay-layer not possible.

Conclusions
Since GPR is an active system its data has good signal-to-noise ratios. GPR has not been used as a long term transient monitoring system, but is usually applied in separate surveys, it seems that a cross-borehole application of GPR might have potential for long term dam monitoring.

References
Carlsten, S., Johansson, S. and Wörman, A. (1995). Radar techniques for indicating internal erosion in embankment dams, *Journal of Applied Geosciences* **33**, 143-156.
United States Department of Transportation website, Federal Lands Highway Program (http://www.cflhd.gov/agm/geoapplications/SurfaceMethods/943GroundPenetratingRadar.htm)

Time Domain Reflectometry (TDR)

What is it?

There are different styles of TDR that have different capabilities and thus have different applicability to embankment monitoring:

(1) In the 1930s TDR was originally developed as a cable tester for transmission and power cables (Kane et al, unknown year). It was also used to test the performance of other electrical cables or circuit boards. Since the 1990s this technique started to be a tool for monitoring slope movement. Kane et al. (unknown year) show several examples of successful slope movement monitoring using TDR, some use on-site data acquisitions, others use remote monitoring systems.

(2) In recent years, TDR has also been used as a method to monitor water content inside water retaining structures. Wörsching et al (2006) performed a lab experiment, where TDR was used to transiently monitor water content and percolation into a laboratory-scale levee (see Figure 4 for their results). They applied long flat-ribbon cable (from top to bottom of their levee, that was built in their laboratory).

(3) Noborio (2001) has a very thorough review on TDR and shows that TDR can be applied at a large scale. He also showed that smaller probes, that do not penetrate the dike's body as much as in the case of Wörsching et al (2006), also work well as sensors for TDR, although, with very short probes, accuracy might become an issue.

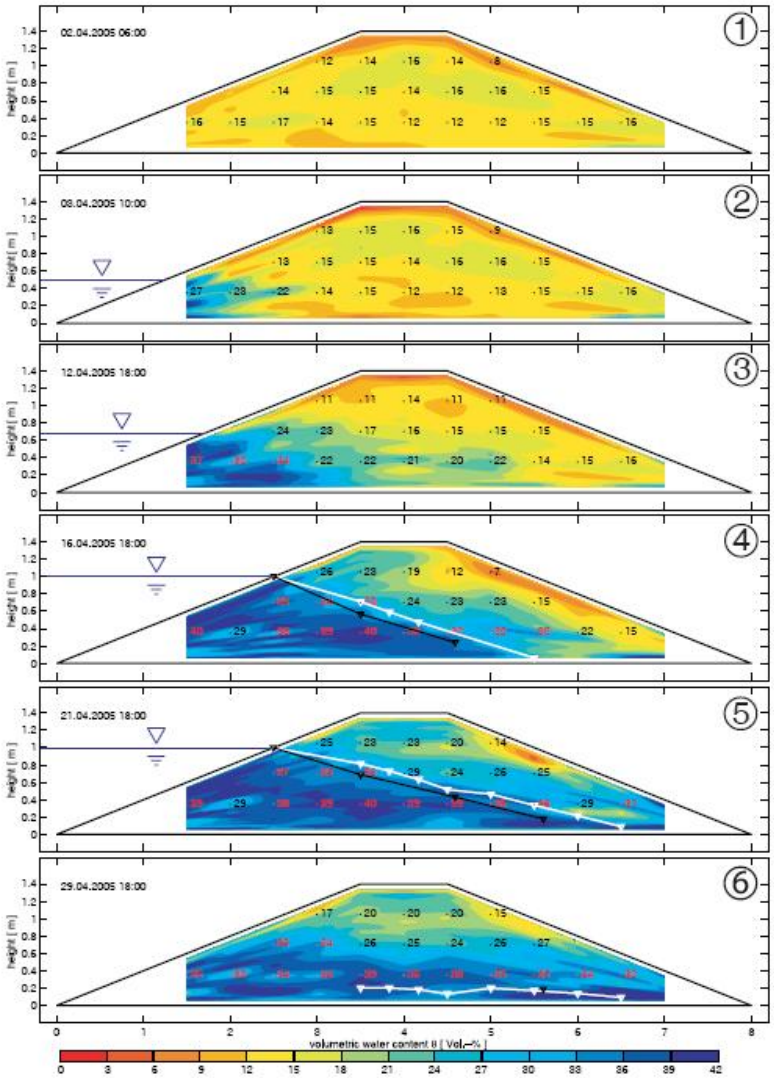

Figure 4 Saturation of a downscaled levee during saturation experiments (TDR) conducted by Wörsching et al. (2006) at Purdue University

How does it work?

(1) TDR in the form of a cable tester is comparable with deformation measurements using optical glass fiber wires. TDR measures the amplitude of reflections from a voltage pulse traveling along a coaxial cable. When

the pulse encounters a cable break, a deformed part of the cable or the end of the cable, the pulse is (partially) reflected. The receiver records the reflected pulse. A computer records the travel time and an automated analyzer makes a comparison between the transmitted pulse and the received pulse. From this information the relative deformation, the rate of displacement and the location of the deformation can be determined instantly (Kane et al., unknown year) (This is very much comparable with deformation measurements that Inventec / Ten Cate applied in the IJkdijk experiments). If the cable has a good physical connection with the dam, the deformation of the dam directly relates to the deformation in the cable, which in itself relates to the amplitude in the data. This way, changes in the data's amplitude correspond to the rate of ground movement. The travel time of the reflected pulse gives information about location of where deformation occurs.
(2) The Spatial-TDR, as described by Wörsching et al (2006), is based on the principle that the relative dielectric properties are much higher for water than for the other constituents of soils (such as lithology). Wörsching et al. (2006) also write that the dielectric properties (ε) are directly related to the squared velocity of the electromagnetic wave along their sensor. The water content can also be correlated using a regression curve based on measured values for a given soil (refer to e.g. Topp et al., 1980 for a comprehensive explanation). Extracting these types of information from the data requires estimation by some inverse modeling. The information about water content can be given with a spatial accuracy of 1 cm along the inserted cable. These measurements have a discrete nature. For the results of the inverted data, refer to Figure 4.

(3) According to Noborio (2001), accurate measurements can also be taken with short (up to few dm) sensors, reducing the impact of installation on the embankments' integrity. The data, originating from the technique Noborio (2001) describes, is a more continues type of data, on which inversion can be applied.

How can this technology be applied to embankment monitoring?
(1) Deformation is not a clear sign for dam failure due to piping, but can be a good tool to monitor for slope instability for instance. Aside from this deformation monitoring, a vertically installed TDR cable could also monitor the internal water level: the electromagnetic pulse is reflected by the water level.
(2) The technique that Wörsching et al. (2006) propose proved to work well in their lab environment. It would be very interesting to try this in a full-scale levee experiment.
(3) Noborio (2001) proposes a method for remote, long-term monitoring using TDR methods, which sounds promising. He states that a combination of electrical conductivity and water content can be measured with instruments that are readily available.

Long term and short term
This technique can be used for short-term as well as long-term deployments.

Advantages
Jones and Or (2004) showed that water content measurements with TDR can be taken in highly saline soils if the data analysis is extended to the frequency domain and the right size electrode is used. This is an advantage since monitoring of seawater retaining dikes involves brackish or saline water intrusion. Dissolved salt ions are notoriously known to mess up electromagnetic measurements.
Furthermore, TDR is a quick and economical method of determining slope movement and water content. When applied in a monitoring system as described by Noborio (2001), TDR has potential to monitor large areas using small probes. Small probes do not interfere with the internal integrity of embankments so much. Stevens Water Monitoring System[1] is a ready-to-use and complete system for monitoring water content in agrarian applications. The development on the hardware was already performed. This can be modified to work as a long-term monitoring system for levees.

Disadvantages
The older TDR methods measures deformation, which is not a significant indicator of dam instability due to piping phenomena, but could be applied to slope instability measurements. The TDR method described by Wörsching et al. (2006), seems more promising for piping monitoring, although the sensors have to be inserted into the dam, somewhat damaging internal structure. However, Wörsching et al. (2006) claim that there is an important development in progress, which would enable them to install the TDR sensors in existing levees in a non-destructive way.

Conclusions
(1) Since failure due to piping usually does not show much external or internal deformation before failure, TDR applied as deformation measurement is more useful for monitoring dam or slope failure due to slope instability than for monitoring failure due to piping phenomena. Another application in dam monitoring is water level

[1] Hydra Probe II Soil Sensor DATA SHEET

measurements, using TDR. The data from a vertically installed TDR cable shows a reflection of the voltage pulse at the water level.
(2) In recent years they found TDR can be applied as a technique measuring water contents (see Wörsching et al., 2006), with very promising results. That paper was taken from the Purdue University's website[2], who did thorough research on the applicability of TDR in geotechnical problems.
(3) According to Noborio (2001), TDR can be applied as a long-term, remotely-operated (remotely, in the sense of operated from another location, with in situ sensors) monitoring system that can monitor continuous data. A more comprehensive explanation of the TDR method, written by Applied Research Associates, Inc., can be found in Schinn et al. (1998).

References

Cole, R. H. (1977). Time domain reflectometry, *Annual reviews of Physical Chemistry*, **28**, 283-300.
Jones, S. B. and Or, D. (2004). Frequency domain analysis for extending time domain refelctometry water content measurement in highly saline soils, *Soil Science Society of America Journal*, **68**, 1568-1577.
Kane, W.F. (1998). Embankment monitoring with time domain reflectometry, *Tailings and Mine Waste '98*.
Kane, W. F.; Beck, T. J.; Hughes, J. J. (unknown year). Applications of time domain reflectometry to landslide and slope monitoring, publication of Kane GeoTech.
Noborio, K. (2001). Measurement of soil water content and electrical conductivity by time domain reflectometry: a review. *Computers and Electronics in Agriculture*, **31**, 213-237.
Shinn, J. D., II, Timian, D. A., Morey, R. M., Hull, R. L. (1998): Development of a CPT probe to determine volumetric soil moisture content. *Geotechnical site characterization: volume 1. Proceedings of the First International Conference on Site Characterization - ISC'98, Atlanta, Georgia, USA*, **1**.
Topp, G. C.; Davis, J. L. and Annan, A. P. (1980): Electromagnetic determination of soil water content: Measurements in coaxial transmission lines. *Water Resources Research*, **16**, 574–582.
Wörsching, H.; Becker, R.; Schlaeger, S.; Bieberstein, A. and Kudella, P. (2006). Spatial-TDR Moisture Measurement in a Large Scale Levee Model Made of Loamy Soil Material", *Proc. TDR 2006*, Purdue University, West Lafayette, USA, Sept. 2006, Paper ID **33**, 15 p., https://engineering.purdue.edu/TDR/Papers

Electroseismic or seismo-electric methods

What is it?
The electro-seismic or seismo-electric method is a method that combines seismic (acoustic) properties of the subsurface with electric properties.

How does it work?
A seismic source initiates a seismic wave, traveling down into the subsurface. These seismic waves also carry electromagnetic waves. When a seismic wave hits an seismic impedance interface, a seismic wave is reflected as well as an electromagnetic wave. Electroseismic methods measure these induced electromagnetic waves at the surface, using a voltmeter antenna. This phenomenon also works the other way around: electromagnetic waves also generate acoustic waves at subsurface impedance contrasts.

[2] https://engineering.purdue.edu/TDR/Papers

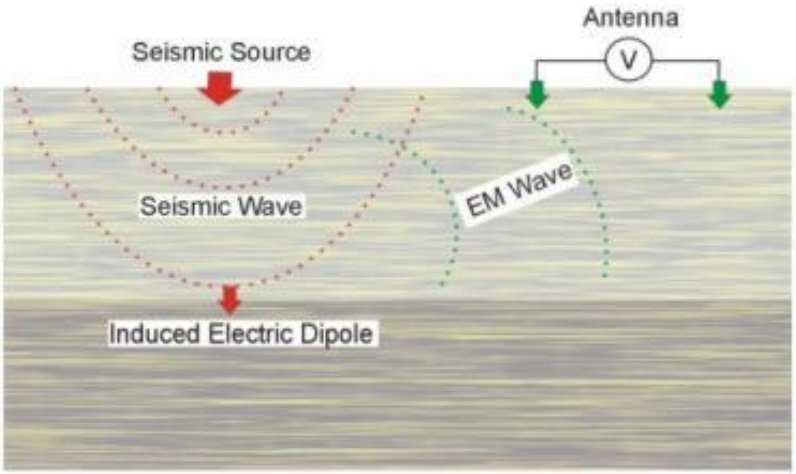

Figure 5 The seismoelectric effect of a seismic wave reflecting from an impedance interface (adapted from Federal Lands Highway Program website, see references)

According to Dupuis et al. (2007), which physical property has most influence in changing the observed parameter is not (yet) clear.

How is this applicable to embankment monitoring?
If these methods were used as a surface surveying method, it should be possible to measure the level of the water table in a non-invasive way. It should also be possible to measure hydraulic conductivity, which is related to permeability and the potential for groundwater flow. Groundwater flow itself can not be measured.

Long term and short term
Electroseismic methods can be applied as short term as well as long term levee monitoring.

Advantages
These methods are non-invasive: the internal structure of the water retaining dam is kept undisturbed. The seismoelectric method is sensitive to differences in hydraulic conductivity. Using this method one can monitor hydraulic conductivity non-invasively.

Disadvantages
Since electroseismic signals are very small (mV), the signal-to-noise ratio can pose a problem in data processing. It seems that it's capabilities are best exploited when used in combination with GPR (Dupuis et al., 2007). Furthermore, literature shows that this method is still under development. Not all observed phenomena can be explained yet. This might make this method hard to apply as a long-term monitoring system. Although, an advantage in the case of embankment monitoring is that we deal with subsurface geometries that are known.

Conclusions
Although the physical background of this non-invasive technique is presently not completely understood, it might be a good method to monitor hydraulic conductivity of the subsurface. Literature shows this technique is still under development, but seems to give good complementary data to GPR surveys.

References
Dupuis, J. C., Butler, K. E., & Kepic, A. W., 2007. Seismoelectric imaging of the vadose zone of a sand aquifer, *Geophysics*, **72**, A81–A85.
Federal Lands Highway Program website: http://www.cflhd.gov/agm/geoapplications/SurfaceMethods/945SeismoelectricalMethod.htm
Haines, S. S., S. R. Pride, S. L. Klemperer, and B. Biondi, 2007, Seismoelectric imaging of shallow targets. *Geophysics*, **72**, no. 2, G9–G20.

Electric Resisitivity Tomography (ERT)

What is it?
Electrical Resistivity Tomography (ERT) uses sensors with direct electrical soil coupling to measure the resistivity of the subsurface (in either 2D or 3D). This has been applied as a long term monitoring technique in a few Swedish embankment dams for water energy generation (applied in Swedish embankments, refer to Sjödahl et al., 2008).

How does it work?
Water is more conductive than the soil matrix, so if water content is increased, the electric resistivity is decreased. Locations with increased water content are imaged as regions of lower resistivity (or higher conductivity).
When applying ERT, an electrical signal is sent into the subsurface and received by a laterally placed sensor array. By varying the receiver – transmitter spacing, information about different depth levels can be obtained, with the help of inversion algorithms.

How is this applicable to embankment monitoring?
Locations with higher hydraulic conductivities show to be more vulnerable in civil engineered structures. If higher hydraulic regions within an embankment's body can be identified, one can identify the vulnerabilities.

Long term and short term
This technique is applicable for short term as well as long term monitoring.

Advantages
This is a non-intrusive technique, of which it's installation involves very little disturbance of the internal structure. According to Sjödahl et al. (2008), ERT works very well in discovering vulnerabilities in the Hällby embankment dam. Kuras et al. (2009) show that, with today's technologies and infrastructure, automated time-lapse electrical resisitivity tomography (including automated interpretation) is possible. They reached typical frame rates of at least 1.5 - 3 images per hour, without compromising the image quality.

Disadvantages
There are several different physical phenomena that influence ERT signals. Although the results from tests on Swedish embankment dams show promising, temperature, seasonal variations and electrode installation have to be taken into account.

Conclusions
ERT shows to be promising in predicting hydraulic vulnerabilities in embankment dams. See the Capacitive Resistivity (CRI) section for an improved method, based on ERT. A three page short introduction to this technology is given by Sjödahl et al. (2007).

References
Kuras, O., Pritchard, J.D., Meldrum, P.I., Chambers, J.E., Wilkinson, P.B., Ogilvy, R.D., Wealthall, G.P. (2009) Monitoring hydraulic processes with automated time-lapse electrical resistivity tomography (ALERT). *Comptes Rendus - Geoscience*, **341**, (10-11), pp. 868-885.
Sjödahl, P., Dahlin, T., Johansson, S. and Loke, M. H. (2008). Resistivity monitoring for leakage and internal erosion detection at Hällby embankment dam. *Journal of Applied Geophysics* **65**, 155-164.
Sjödahl, P., Dahlin, T. and Johansson, S. (2007). Detection of internal erosion and seepage evaluation using resistivity monitoring, *WasserWirtschaft*, 10 / 2007, p. 54-56.

Capacitive resistivity Imaging (CRI)

What is it?
The Capacitive Resistivity (CR) or Capacitive Resistivity Imaging (CRI) technique basically is an improved DC resistivity method. This method is less vulnerable to highly-resistive surfaces, like engineered surfaces (roads, pavements, embankments dams etc.), frozen or dry soils and more. Unlike Electric Resistivity Tomography (ERT), non-contacting capacitive electrodes permit continuous data acquisition on highly resistive surfaces (British Geological Survey website, see references).

How does it work?
CRI is very similar to normal DC resistivity measurements and data processing can be done with existing data processing and inversion algorithms for regular ERT. It is different in how it lays the electrical 'connection' with the ground surface. In ERT, the coupling between the transmitting sensors and the ground is a direct coupling. This means that a high resistant upper soil layer will attenuate a large portion of the transmitted signal. In electromagnetic methods, such as GPR, an inductive coupling is used; the transmitted electrical signal induces a magnetic signal which is recorded. CRI methods however, are based on another physical phenomenon, called capacitive coupling. Transmission signal attenuation is much larger, allowing for better data quality and signal-to-noise ratios.

Figure 6 Capacitive sensor towed by a truck. These sensors can be dragged over any surface – due to their capacitive electrical 'connection' with the subsurface they can measure an ERT through surfaces. (Source: Britsh Geological Survey information sheet, see references).

How is this applicable to embankment monitoring?
CRI equipment could be installed permanently on a levee and give us information about the resistivity in the subsurface (or internal resistivity structure of a levee's body). Internal resistivity is an indicator for water contents and can be related to hydraulic heads within civil engineered structures.
In locations where internal water pressures and seepage are increased, more water is relatively present. Water has a lower resistivity than dry soils, making the resistivity a good indicator of water content. Resistivity data can indicate preferred seepage paths through dams and show internal vulnerabilities.

Long term and short term
Since CRI works better than ERT on man-made surfaces and it can be dragged over those surfaces, CRI equipment is very mobile, making it ideal for short term measurements. CRI measures localities with higher electric conductivities and can so quickly detect weaknesses. For long term monitoring fixed sensors might need to be developed.

Advantages
CRI is an active method, decreasing the influence of external noise factors. Examples of 2D and 3D surveys over shallow targets show the superior quality and resolution of CR datasets compared with conventional DC resistivity (Kuras, 2006).
Furthermore, the British Geological Survey (BGS) has designed ready-to-use equipment for CR surveys (Capacitive Resistivity Imaging flyer, 2010). BGS also claims that CRI can perform resisitivity imaging with lateral resolution in the order of centimeters, with far superior results to ERT.

Disadvantages
The CRI method (and ERT method) gives information about the resistivity (or conductivity) of the subsurface. Changes in dissolved elements in the water (such as salt water intrusion) can change the accuracy of the results: this method does not indicate the flow of water.

Conclusions
Resistivity tomograms can give a good indication for vulnerabilities within human-made engineering structures (Sjödahl et al., 2008). The CRI method gives better results than regular ERT surveys. Opposed to regular DC resistivity tomography (ERT), CRI gives better data quality and signal-to-noise ratios, due to a different

concept of 'connecting' the sensors with the subsurface: direct versus capacitive coupling (for ERT and CRI respectively).
CRI seems to give good electric resistivity data, which is seen as a good indicator of water contents and an indicator of hydraulic vulnerabilities within embankment dams.

References

Capacitive Resistivity Imaging flyer (2010), The British Geological Society (downloadable from their website)
Britsh Geological Survey (BGS) website: http://www.bgs.ac.uk/research/tomography/CRI.html
Kuras, O.; Beamish, D.; Meldrum, P.I. and Ogilvy, R.D. (2006) Fundamentals of the capacitive resistivity technique, *Geophysics*, **71**, 3, p. 135-152.
Sjödahl, P.; Dahlin, T.; Johansson, S. and Loke, M.H. (2008) Resistivity monitoring for leakage and internal erosion detection at Hällby embankment dam, *Journal of Applied Geophysics*, **65**, p. 155-164.

Induced Polarization method (IP)

What is it?

The IP method is a non-invasive geophysical method, which, using an induced electrical potential applied to the surface, measures the chargeability of the subsurface (Kearey and Brooks, 1991). This method can be applied in two different domains; the time domain (generally called the IP method) and the frequency domain (which is also referred to as Spectral Induced Polarization or SIP method). According to Patella and Schiavone (1977), the best method depends on the polarizability (polarization potential or chargeability) structure of the subsurface, where the frequency domain method is most sufficient when the polarizability increases with depth and the time domain method works best for decreasing chargeability.

How does it work?

In time domain IP measurements a direct current (DC) is subjected to (an array of) electrodes on the surface. After a certain time, when the surface has had enough time to charge under the subjected potential, the induced charging is stopped and the measure of decay of charge (or relaxation time) is a function of the chargeability of the subsurface. This chargeability is a function of the separate chargeabilities of the lithology, the pore fluid (in combination with its dissolved matter) and the water contents (Binley and Kemna, 2005), such as dissolved elements. Together they produce the total chargeability of the porous medium. Since the aim is *monitoring* an area, the lithology will not change with time, and thus the chargeability of the lithology remains more or less unchanged. This implies that if there is interest in the saturation of the porous medium, the pore fluid's chargeability needs to be known. This might be problematic in regions where salt water intrusion occurs (such as sea water retaining dams or embankments), since the salt contents is not known and thus the chargeability is unknown.
Spectral Induced Polarization works generally the same as IP, but instead of DC and alternating current (AC) is used. A phase shift occurs between the subjected and measured current, which is comparable to the relaxation time in normal IP measurements. According to Binley et al. (2005), SIP can also be used to approximate the hydraulic conductivity of the subsurface. Since the hydraulic conductivity under an embankment is increased significantly by the piping phenomenon, this method might also have potential for monitoring piping occurrence.
The phase shift can be different for different input signal frequencies. In low frequency SIP surveys (Olhoeft, 1985), with frequencies in the range of <1000Hz, polarization of the ionic charge associated with the electrical double layer at the mineral-fluid interface is the dominant mechanism (Binley et al., 2005). The electrical double layer exists in close proximity of grains. Titov et al. (2002) propose a model that the mineral-fluid interface surface area, which is linearly related to the chargeability of the aforementioned electrical double layer, is related to the pore space in a predictable fashion and can thus be used as a proxy for hydraulic conductivity.

Long term and short term

There is IP acquisition hardware that is very mobile, which is ideal for a short-term application of this technique. For long-term or permanent deployment this technique is also very applicable.

Advantages

IP methods are non-invasive. This means that the embankment does not need to be penetrated for installation of this monitoring system. It uses electrodes on the surface, which apply an induced potential to the levee. An

induced potential has the advantage that the measured signal is less affected by anthropological noise sources. A three-dimensional image of the water contents of the embankment can be produced from IP measurements, from which water pressures can be derived. Furthermore, an IP monitoring system can easily be scaled up by adding more electrodes or enlarging the electrode offset, although the latter decreases the resolution.

Disadvantages
Induced polarization methods are able to indicate water content levels, which act as a proxy for hydraulic heads and water pressures, but can not give information about actual water flow (or seepage in the case of embankment monitoring), let alone flow direction. The methods relies on the assumption that embankments show higher hydraulic conductivities in their weaker areas.
Problems may occur when this method is applied as a monitoring system in areas where transiently changing pore fluid chargeability is present (such as salt-water intrusion in coastal areas), which may influence the results. To decrease this measurement error, the chargeability of the pore fluid should be monitored in sensitive areas or. Another possibility is that we would empirically learn from a longer monitoring time, although this seems difficult.

Conclusions
The time domain IP method seems promising in monitoring soil water content in areas where pore fluid chargeability is constant with time or monitored separately. Furthermore, frequency domain IP measurements could indicate localities of increased hydraulic conductivity (what piping essentially is). Currently there are no out-of-the-box solutions for long-term monitoring equipment.
Probably the best application of this method is recognizing variations in permeability of the subsurface. These measurements can be used to select vulnerable areas.

References
Binley, A. and Kemna, A. (2005), DC Resistivity and Induced Polarization Methods, Hydrogeophysics (Part 2), 129-156.
Binley, A., L. D. Slater, M. Fukes, and G. Cassiani (2005), Relationship between spectral induced polarization and hydraulic properties of saturated and unsaturated sandstone, *Water Resour. Res.*, **41**, W12417
Kearey, P.; Brooks, M. (1991). An Introduction to Geophysical Exploration (Second edition ed.). *Blackwell Science*
Patella, D. and Schiavone, D. (1977). Comparative Analysis of Time Domain and Frequency Domain in the Induced Polarization Prospecting Method, *Geophysical Prospecting*, **25**, 3, 496-511
Titov, K., Komarov, V., Tarasov, V., and Levitski, A. (2002). Theoretical and experimental study of time domain-induced polarization in water-saturated sands, *Journal of Applied Geophysics*, Volume **50**, 4, 417-433

Internal flow meter

What is it?
There are different types of flow meters. The simple, original flow meter is a mechanical device, with a propeller-like shape that turns as water flows through it. Also acoustic methods exist that measure flow velocity in a tube, using high-frequency acoustic signals (Voser et al., 1996).

How does it work?
In the original setup, the flow meter is in direct contact with the water. The water drives the flow meter; the more rotations per minute the device makes, the faster the water flows. The output flow velocity can be calibrated to the rotation velocity.
Voser et al. write about a flow meter that uses a tube through which the water flows. An acoustic signal is sent through this tube, which indirectly measure the flow rate.

How is this applicable to embankment monitoring?
Internal installation of a flow meter can monitor the seepage through a levee.

Long term and short term
For long term applications the flow meters without mechanical parts can be applied in long-term monitoring deployments, although the mechanical nature of these devices might give problems at longer deployments.

Short-term monitoring is hardly possible; it takes too long to install flow meters. Furthermore, in times with high water levels, one wants to avoid any disruption of the levee's internal structure.

Advantages
The flow meter is in direct contact with the water, possibly giving more accurate measurements. It is also a relatively simple device, making maintenance a simpler job.

Disadvantages
Since a flow meter is a mechanical device through which water flows, problems with corrosion and/or clogging by clay or sand grains. Installation of these devices need penetration in the levee body, disrupting the internal integrity. Also, measuring flow with a flow meter gives discrete data, we only know what happens exactly at the position of the flow meter. Besides, the situation created at the instrument is not representing the undisturbed situation very well; therefore the measurements can even be misleading.

Conclusions
A flow meter might be a good short-term monitoring device, but for long-term monitoring it is not recommended. Due to the fact that it is a mechanical device, over time clogging will occur.

References
Voser, A. Bruttin, Ch., Prénat, J.-E. Staubli, T. (1996) Improving acoustic flow measurement. *Water Power & Dam Construction*.

Dye tracer testing

What is it?
A dye coloring can be added to groundwater to trace the underground flow paths. This is also used to discover the flow path geometry of caves and underground rivers. In the IJkdijk project the idea of using dyed sand under the test levee in order to study pipe lengths did not persist for both practical reasons and operational costs.

How does it work?
Add a dye liquid to the upstream side of the water retaining levee and wait for it to occur on the downstream side. The time it takes to travel from up- to downstream side of the levee is a proxy for the flow velocity, which can be seen as a proxy for increased internal water seepage.

Long term and short term
Long term monitoring using dye tracers is very labor-intensive. In general, the implications to the environment should be considered. For short-term tests, other weaknesses can not be recognized using dye tracers.

Advantages
In principle it is easy to apply.

Disadvantages
It is not possible to automate this to perform as an automated long term monitoring system. Furthermore, water flows under the levee constantly (regular seepage), piping only increases water flows. Also, it is very labor-intensive, making it more expensive.

Conclusions
Dye testing does not seem to be a feasible method for long term embankment monitoring, since it can not be automated. Furthermore dye testing is not easily applied to large scale monitoring, due to the labor-intensive character of this method.

References
Turkmen S., Ozguler E., and Taga H. (2002) Seepage problems in the karstic limestone foundation of the Kalecik Dam (south Turkey). *Engineering Geology*, Vol. **63**, No. 3-4, pp 247-257.

APPENDIX 9 : INTERPOLATION AND TIMELINES

Interpolation is a technique where an X,Y point in the graph (time, value) is being calculated based on surrounding available points (measurements). The interpolation starts with the *measurements*, the result of the interpolation are called *points*. Because there are many ways to perform the interpolation and many different sensor data types, the interpolation mechanism should be pluggable.

For instance, a request to the TimelineStore is sent to get 8 points, evenly spaced in time. The top panel of Figure 1 below shows the measurements. It contains 12 measurements, the stars, and a connecting line between them. The bottom panel of Figure 1 shows the interpolated values using a linear interpolation technique. The circles represent the (interpolated) points on the requested timestamps.

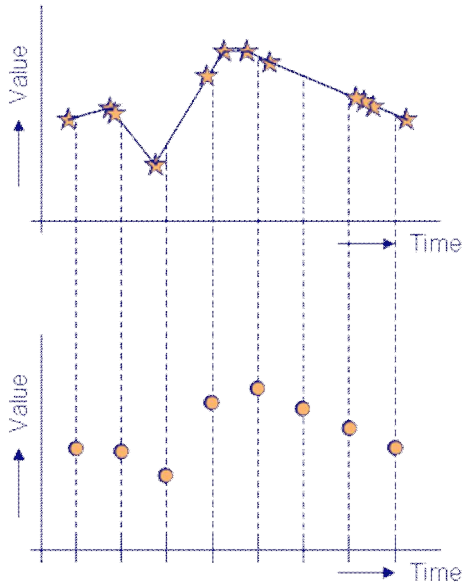

Figure 1 Interpolation example

There are many different interpolation techniques. In this report we investigate two of them: linear interpolation and sample-and-hold interpolation.

Linear interpolation
Figure 2 shows the linear interpolation as a timeline. The top line contains the actual measurements and their values. They are non linear spaced, because the sample moments happened to be non linear. The lower line shows the result of the linear interpolation. The first step is determining the timestamps of the requested points. Thereafter the corresponding values for these points are calculated using linear interpolation.

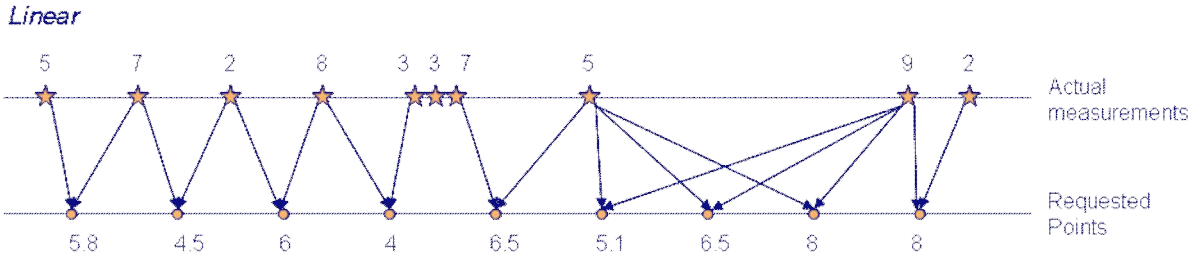

Figure 2 Linear interpolation example

Sample-and-hold interpolation
The sample-and-hold technique uses the last known (and measured) value. A value is being sampled and hold, until the next value is being sampled. The value being hold is used as the value for each point requested. The advantage of this interpolation technique is that no calculation is necessary to determine the intermediate values.

Figure 3 shows the sample-and-hold interpolation as a timeline. The top line contains again the actual measurements and their values. The lower line shows the result of the sample-and-hold interpolation.

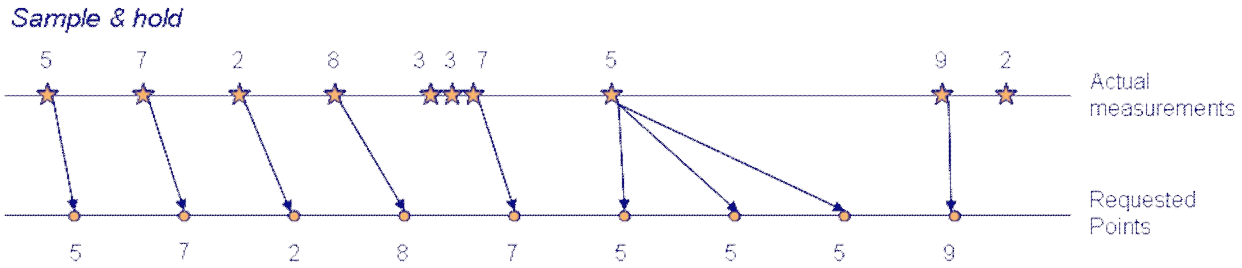

Figure 3 Sample-and-hold interpolation example

For each of the supported sensor value types in the database, the possible interpolation techniques must be configured. Not all interpolation techniques are suited for all sensor types. What would linear interpolation for example be on a text based sensor?

APPENDIX 10 : COLUMN BASED DATABASE

A new type of databases begins to become available, the column based databases as proposed by Google in a paper in 2006. Google BigTable is a column oriented distributed storage system that was designed for the storage and maintenance of huge amounts of data. It is known to be able to store petabytes of data, scattered over thousands (!) of instances. They combine the idea of column based databases with highly distributed implementation, using only low cost hardware. It is so robust, that hardware failures (mainly hard disks) has no influence on the database as a whole. It is scalable, extremely robust and failsafe.

This idea has been picked up by many developers but is very difficult to implement. At the moment there are several open source projects, but all of them still in beta, even after 4 years! One of the promising ones comes from the Apache group and is called Cassandra. The development of Cassandra has started at Facebook, they open sourced the project in 2008. It is a combination of the fully distributed design of the Amazons Dynamo system and the Google Bigtable's ColumnFamily-based data model.

In principle it is a key-value store, which makes it easy to store only data which is available. In Figure 1, sensor S1 has on three moments measurements, sensor S2 only on two. The system has a fall-through technique which makes it possible to get responses for something you did not explicitly asked.

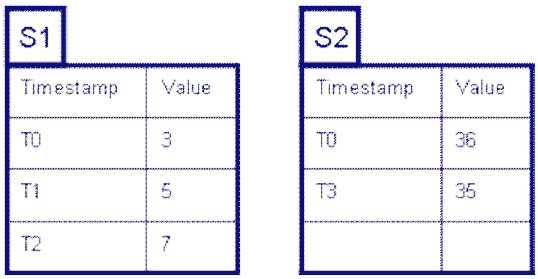

S1

Timestamp	Value
T0	3
T1	5
T2	7

S2

Timestamp	Value
T0	36
T3	35

Figure 1 Column based database for sensor measurements

Query for measurements on timestamp T0: {{S1, 3}, {S2, 36}}
Query for measurements on timestamp T1: {{S1, 5}, {S2, 36}}
Query for measurements on timestamp T3: {{S1, 7}, {S2, 35}}

Notice that or the value at that time is returned, or the value of the last known measurement. T1 is not present for S2, therefore the value of T0 is returned. The query had a fall through the data. Google uses this technique to store the many versions of a webpage index. Most pages are more or less static, only small changes are made. With this technique only those changes are stored, with their timestamp, all the parts of the webpage that did not change are not stored again. This results in many, many, many columns with width 2, but that is what the column based database is build for.

APPENDIX 11 : TIMELINES REST INTERFACE

The timeline store can be queried by the use of a REST-interface. Below you will find the specification of this interface which enables you to retrieve and store sensor data. Also the management of sensors and timelines can be done by this interface.

REST Interface
The REST interface has the following functionality:

- Retrieval
  - Get raw measurements
  - Get points
- Store
  - Store measurement
- Management
  - Available sensors
  - Available Timelines
  - Register sensor
  - Register timeline

The REST interface is HTTP based, some examples of the request and response. The request is part of the HTTP GET request, the responses are in JSON format.

Store measurement
The request consists of:

- The command (`storemeasurement`)
- The ID of the sensor (`livedijk:alertsolutions:1a_32ph`)
- The timeline name (`base`)
- The timestamp in ms since 1970 (`1278902215000`)
- The value (`value=1054.0`)

```
Request:
   http://localhost:8081/storemeasurement/
   livedijk:alertsolutions:1a_32ph/base/1278902215000/
   ?value=5564.785

Response:
   HTTP OK
```

Get raw measurements
The request consists of:

- The command (`rawmeasurements`)
- The ID of the sensor (`livedijk:alertsolutions:1a_32ph`)
- The timeline name (`base`)
- The from and to timestamp in ms since 1970 (`1278902215000/1278903717000`)

```
Request:
   http://localhost:8081/rawmeasurements/livedijk:alertsolutions:1a_32ph/base/
   1278902215000/1278903717000

Result:
   {"timeline":[
      [1278902215000,1054.0],
      [1278902516000,1049.0],
```

```
      [1278902816000,1057.0],
      [1278903118000,1052.0],
      [1278903417000,1051.0],
      [1278903717000,1047.0]
   ]}
```

Get points

The request consists of:

- The command (`timeline`)
- The ID of the sensor (`livedijk:alertsolutions:1a_32ph`)
- The timeline name (`base`)
- The from and to timestamp in ms since 1970 (`1278902215000/1278903717000`)
- The nr of points to be returned (4)
- The type of interpolation to be used (`interpolator=linear`).

Note that the request time period is the same as with the raw measurements, the result is different. Interpolated over the same dataset over 4 moments.

```
Request:
   http://localhost:8081/timeline/livedijk:alertsolutions:1a_32ph/base/
   1278902215000/1278903717000/4
   ?interpolator=linear

Response:
   {"timeline":[
      [1278902215000,1054.0],
      [1278902715666,1054.3244266666666],
      [1278903216333,1051.671127090301],
      [1278903717000,1047.0]
   ]}
```

APPENDIX 12 : BUILDING BLOCKS IN TREND ANALYSIS

Explanation

1. Sample and hold

For some other building blocks (e.g. moving average), it is necessary that there are no missing measurements. For other building blocks (e.g. subtraction and FFT) the measurements should have exactly the same time stamp. This building block is implemented by the interface on the timeline store (see section **Error! Reference source not found.**)

2. Moving average

Given a series of measurements and a fixed subset size (window), the moving average can be obtained by first taking the average of the first subset. The fixed subset size is then shifted forward, creating a new subset of numbers, which is averaged. This process is repeated in time. The plot line connecting all the (fixed) averages is the moving average. Thus, a moving average is not a single number, but it is a set of numbers, each of which is the average of the corresponding subset of a larger set of data points.
A configuration parameter for this building block is the size of the window (number of samples).

This building block can be used to reduce the noise. In Figure 1 the pore pressure measurements are depicted in the left panel. Usually, the time between each sample is 5 minutes. At some instances, e.g. around day 60, samples are missing. The signal of the left panel is resampled using the sample-and-hold building block in the timeline store. In the right panel, the average is calculated every 5 minutes over the last 12 samples (given the sample time this means an average over exactly 1 hour). As can be seen this signal is less noisy.

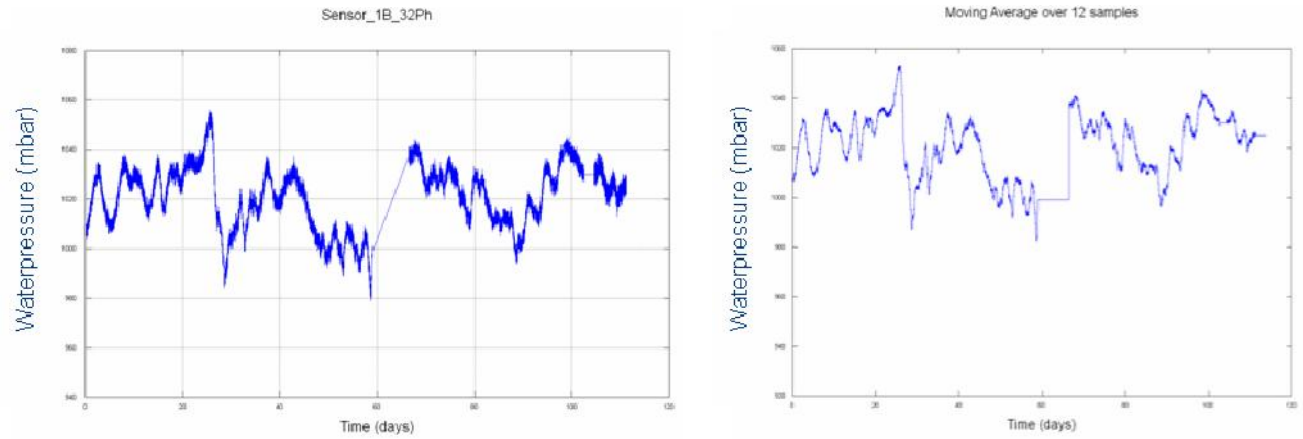

Figure 1 Pore pressure directly (left) and after moving average over 12 samples (right)

3. Average and standard deviation

This building block calculates the average of the stream of sensor measurements (Figure 2). Next to this, it calculates how much variation or 'dispersion' there is from this 'average'. The building block gives an update of the average and deviation each time a sample arrives. Because the stream is "endless" a smart algorithm is used (to prevent increasing memory use and calculation time). It uses a constant number of calculations and a few parameters that need to be stored:

`nrOfSensorValues`	= number of sensor values since start
`sumOfSensorValues`	= sum of all sensor values since start
`sumOfSquareOfSensorValues`	= sum of the square of all sensor values since start

```
protected void calculateAverageAndDeviation(float value) {
        nrOfSensorValues++;
        sumOfSensorValues         = sumOfSensorValues + value;
        sumOfSquareOfSensorValues = sumOfSquareOfSensorValues + value*value;
        average = sumOfSensorValues / nrOfSensorValues;
        if (nrOfSensorValues != 0) {
            standardDeviation = (float)Math.sqrt(
                (sumOfSquareOfSensorValues - (sumOfSensorValues*sumOfSensorValues /
        nrOfSensorValues))
                / (nrOfSensorValues-1)
            );
        } else {standardDeviation = 0;}
}
```

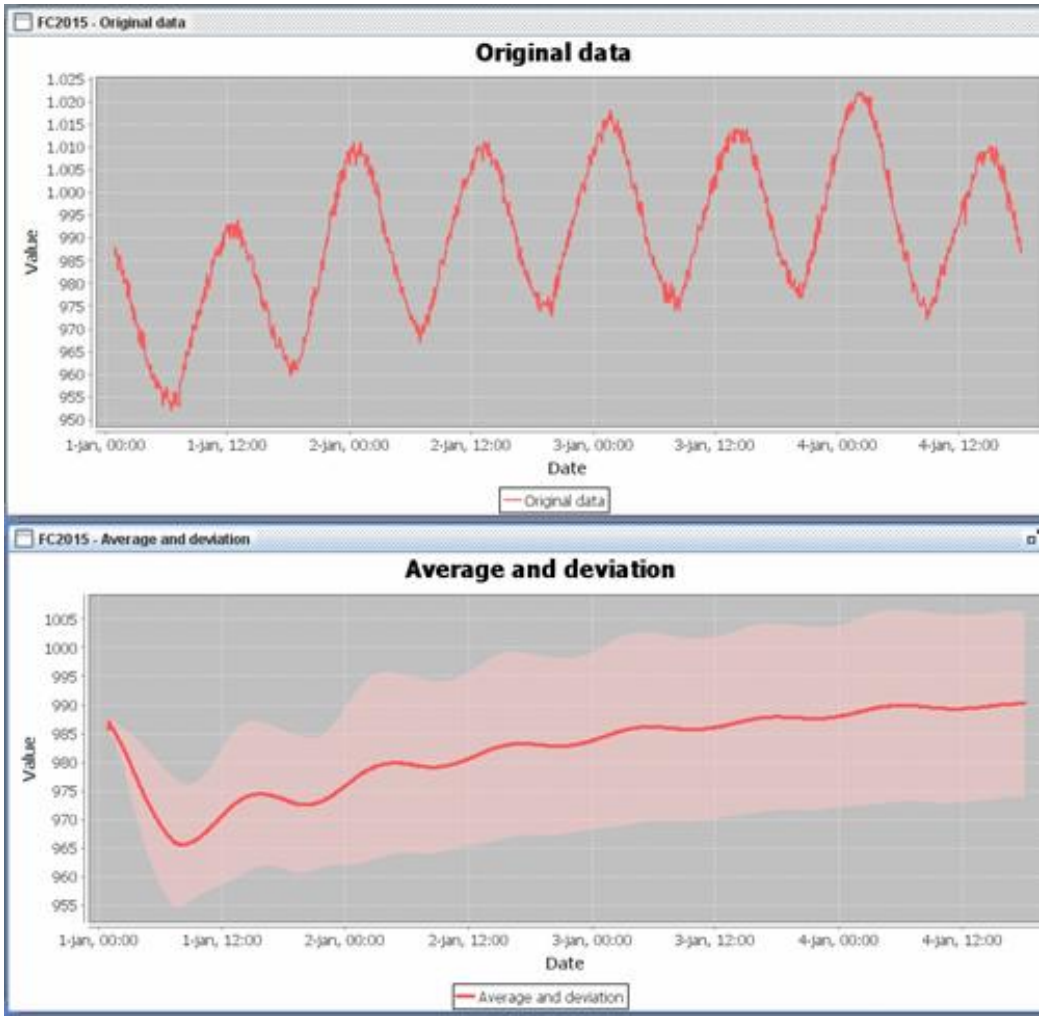

Figure 2 Original data (top) and Average since start and deviation (bottom)

4.Subtraction

This building block is to subtract 2 signals. It can be used e.g. to correct the pore pressure for the atmospheric pressure. To make it possible, both sensor signals should be resampled using the sample-and-hold mechanism (in the timeline interface) to have both signals available at the same timestamps.

In Figure 3, pore pressure signals are depicted and the atmospheric pressure (blue), using the sample and hold building block, followed by moving average (for noise reduction). In the right figure the atmospheric pressure signal is subtracted from all pore pressure signals.

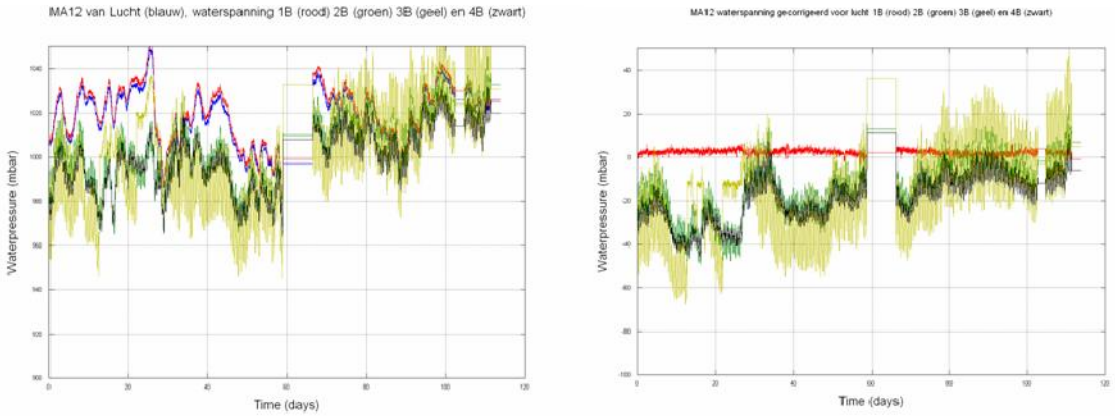

Figure 3 Atmospheric pressure (blue) and 4x pore pressure (left); corrected pore pressure (right)

5. Fast Fourier Transformation (FFT)

This building block is used to transform a sensor signal (discrete time domain) into frequencies and amplitudes (frequency domain). To make a FFT calculation possible, there are some constraints to the sensor signal:

1. the samples should be equidistant in time (so no missing samples)
2. the number of samples should be a power of 2 (e.g. 256 samples, 512 samples, 1024 samples).

Figure 4 gives an example of measured pore pressures from the LiveDijk and the result of the FFT. In the left panel, the original data is depicted for the last 512 samples (i.e. 1.78 days, due to 5 min sample interval). The right panel shows the frequencies (and amplitudes) after FFT analyses of the left signal. Note that the frequency is given in micro Hz. The peak is located at the tides.

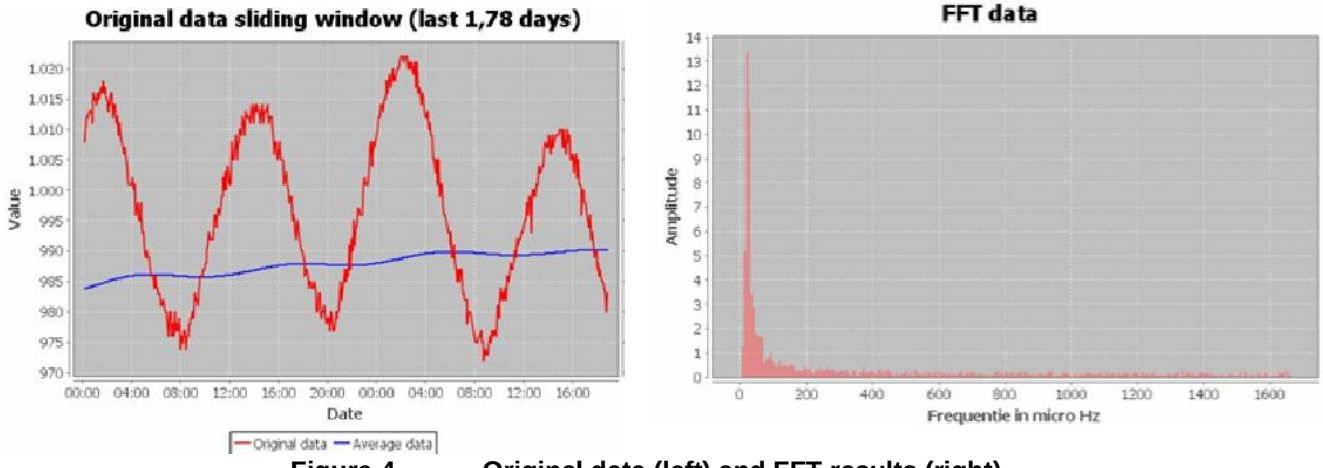

Figure 4 Original data (left) and FFT results (right)

For constraint 1 resampling using the sample and hold building block (via the interface on the timeline store) is essential. For constraint 2 the same timeline interface can be used to get *nicely* distributed samples over the period to be analyzed. Otherwise one can get the following. If there is a signal with a sample time of 5 minutes, the length of signal used for FFT analyses will be 0.9 days using 256 samples, and 1.8 day using 512 samples. For the analyses of exactly 24 hours in 256 samples, the sample time should be 337.5 seconds (is 5.625 minutes). This is where the timeline interfaces can be used perfectly: ask for 256 points in 24 hours!

6. N-strongest frequencies:
This building block returns the N strongest frequencies and amplitudes (based on the output of the FFT). This parameter N can be configured. In Figure 5, five sensor signals of the pore pressure during 113 days are shown in the upper panel (32768 samples). In the other two panels, the FFT results are depicted (frequency in times per day). In the middle panel, all frequencies are shown (more than 16000 frequencies). In the bottom panel, only the 100 strongest are shown. As can be seen this signal is similar as the signal in the picture showing all frequencies and therefore representative for the signal. Note that there is a peak at 2 times per day (being the tides).

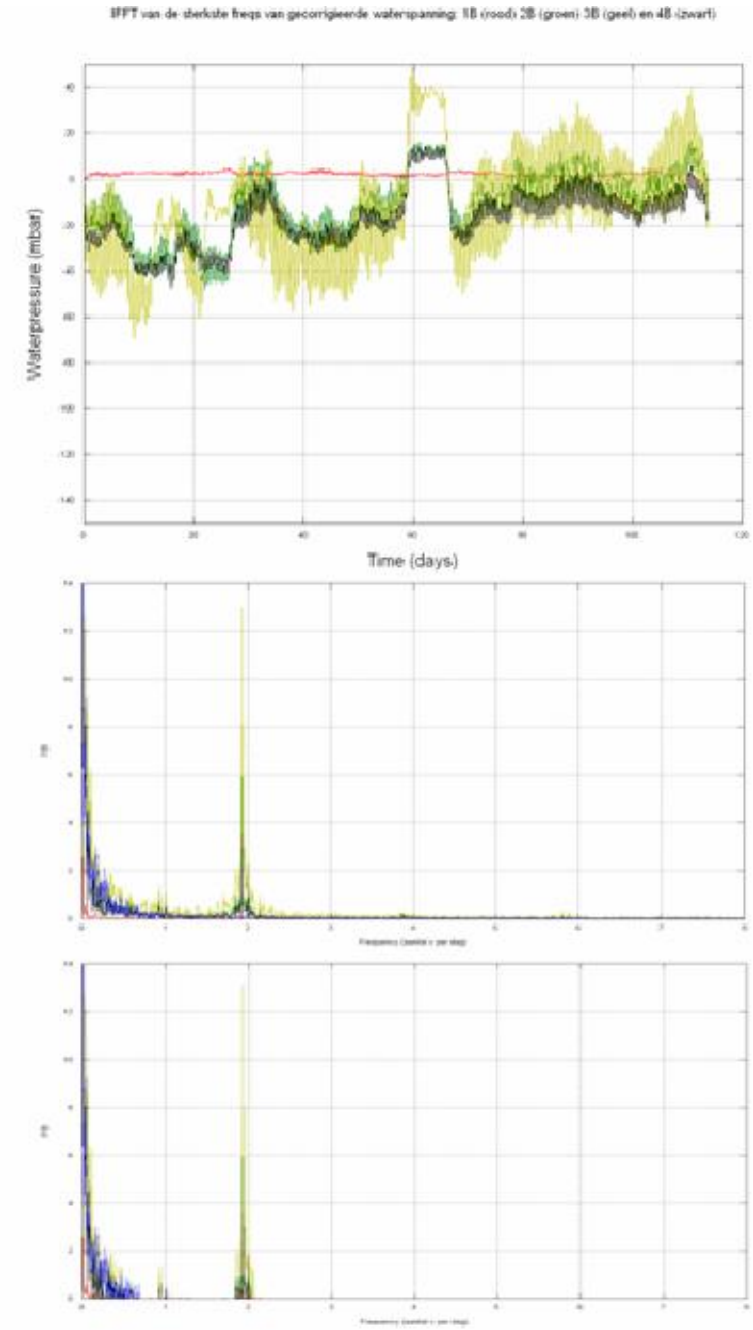

Figure 5 Original data (top), FFT results (middle) and N=100 strongest (bottom)

The results of this building block could be used for reconstructing the original signal using the IFFT (see next building block).

7. Inverse Fast Fourier Transformation (IFFT)

The Inverse Fast Fourier Transformation (IFFT) building block transforms a signal from the frequency domain into the discrete time domain. Input for this building block can be the output of building the N-strongest-frequencies building block to make a reconstruction of the original signal with only the strongest N-frequencies.

In Figure 6, an example is depicted using the 100 strongest frequencies of the previous figure (and building block). In the upper panel the original signals are depicted. The bottom panel shows a zoomed in part of the original signals. In the middle panel, the reconstructed signals are depicted.

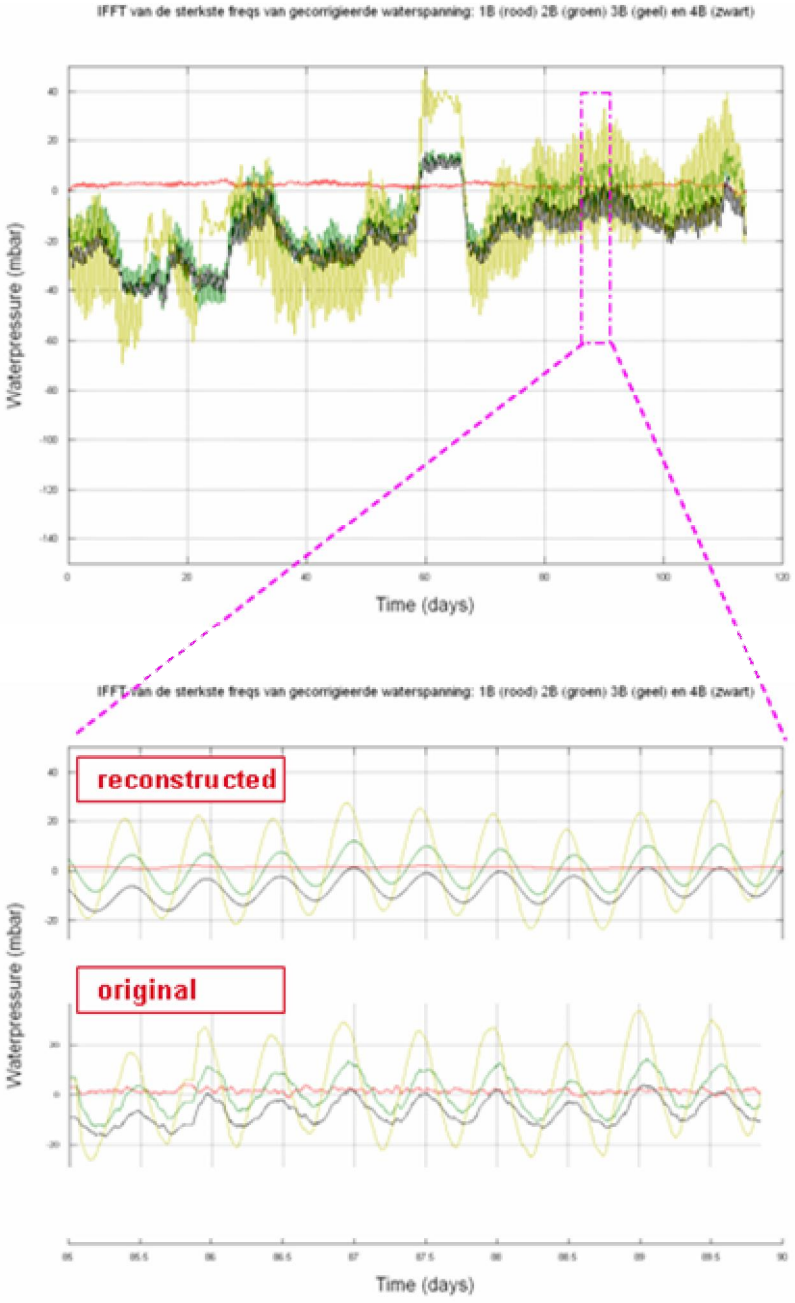

Figure 6 **Original signals (top); originals zoomed in (bottom) and reconstructed signals (middle)**

8. Number-of-Dominant frequencies

This building block returns the number of frequencies (integer value) which are determining the sensor signal (based on the output of the FFT building block). To determine the dominant frequencies an "energy-calculation-algorithm" is used. This algorithm calculates the sum of the squares of the amplitudes coming from the FFT (while omitting the bias signal: amplitude for frequency=0). Then it calculates the energy in the same

way using a subset of frequencies with the highest amplitude, until the energy of this subset is ETA-percent of the original energy calculation. This parameter ETA is a configuration parameter of the building block. The result of the building block is the number of frequencies which was necessary to reach ETA-percent of the energy function. In Java code it looks like this:

```
protected void determineContributingFrequencies() {
        Arrays.fill(contributingFFTSignal, 0);
        double[] copyFFT = fftSignal.clone();
        double originalEnergy=0;
        double contributingEnergy=0;
        int highestIndex=0;
        double highestValue=0;

        copyFFT[0] = 0;               // First element in FFT is the bias
        nrOfContributingFreqs=0;      // This where we are looking for

        // Determine energyvalue of the original without bias
        for (int t=0; t<NR_OF_FFT_VALUES; t++) {
                originalEnergy=originalEnergy+(copyFFT[t]*copyFFT[t]);
        }

        // Find those frequencies which determine the energy value
        // while not enough energy AND not reached all values
        while ((contributingEnergy < ETA * originalEnergy)
                && (nrOfContributingFreqs <= NR_OF_FFT_VALUES)){

                // find the strongest amplitude
                highestValue = 0;
                for (int t=0; t<NR_OF_FFT_VALUES; t++) {
                        if (copyFFT[t] > highestValue) {
                                highestIndex = t;
                                highestValue = copyFFT[highestIndex];
                        }
                }
                // you have found a strongest value, now use it to calculate the new energy value
                nrOfContributingFreqs = nrOfContributingFreqs+1;     // increase counter
                contributingFFTSignal[highestIndex] = highestValue;  // places value at right spot
                copyFFT[highestIndex] = 0;                           // reset the value in the copy
                // increase the energy value
                contributingEnergy = contributingEnergy + (highestValue*highestValue);
                }
        }
}
```

In Figure 7 a pore pressure signal is shown (using sample and hold, but without correction for atmospheric pressure) in the upper picture. In the lower picture the number-of frequencies is depicted, using ETA=0.7. As one can see, most of the time 2 frequencies are contributing to the pore pressure signal, sometimes 1 and sometime 3. At the right side of the graphics a distortion in the pore pressure signal can be seen. This can be detected by watching the number of contributing frequencies, which is increased to 5 frequencies.

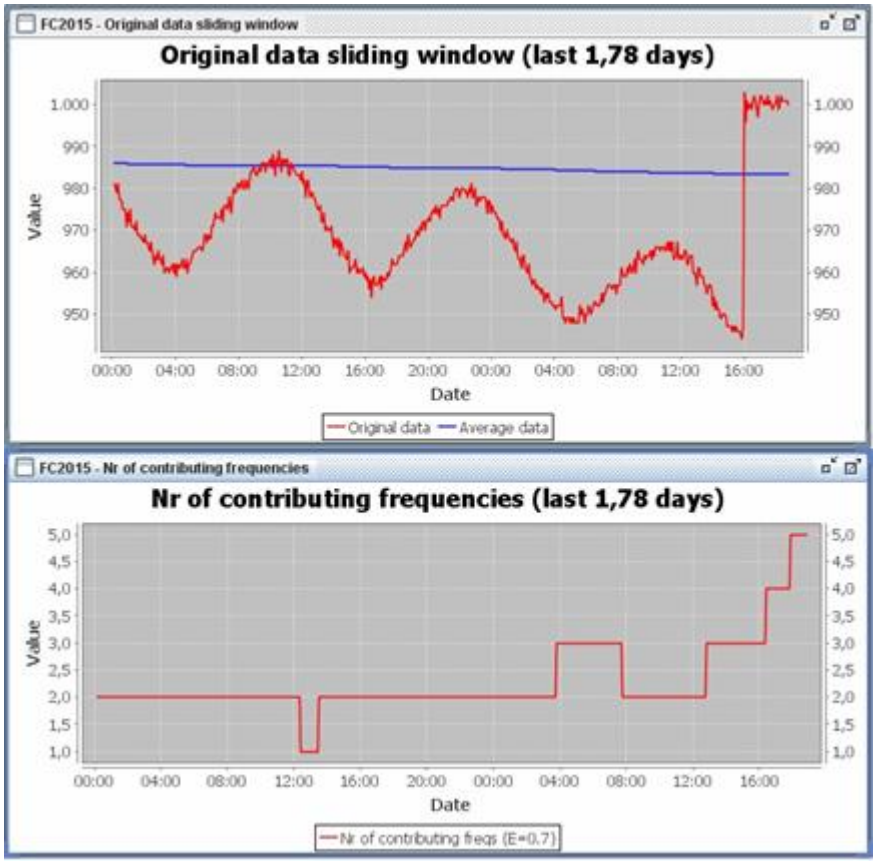

Figure 7 **Pore pressure (top); Number-of-contributing frequencies for ETA=0.7 (bottom)**